

Deformation in small dimensions studied by thin wires in torsion

Dong Dong

September 2015

School of Engineering and Materials Science

Queen Mary University of London

Supervisors: Dr. Andy Bushby and Prof. David Dunstan

**This thesis is submitted in partial fulfilment of the requirements for the degree of
Doctor of Philosophy from Queen Mary, University of London**

Declaration

I declare that the thesis entitled “Deformation in small dimensions studied by thin wires in torsion” is my own and has been generated by me as the result of my own original research.

This thesis contains no material which has been accepted for the award of any other degree or diploma in any University. To the best of my knowledge and belief, this thesis contains no material previously published or written by another person, except where due reference has been made.

Dong Dong

Abstract

This thesis comprises studies of deformation of thin wires in torsion. Generally, experiments in small-scale plasticity usually focus on small-sized samples. However, studying thin wires with lengths up to a meter in torsion has the advantage of giving extremely high strain resolution and reversal of the loading direction. These experiments allow the transition from elastic to plastic deformation to be studied in forward and reversed loading and subsequently to high strains.

In this way the work explored the very early stages of plastic deformation. This is important since structural failure is usually a consequence of exceeding the elastic limit. Micro-strain plastic deformation, dislocation creep, Bauschinger effects and the thermal activated recovery were easily observed. The onset of irreversible deformation was also observed and associated with a few dislocations in the largest grains throughout the wire. Easy plastic deformation on reversal of the loading direction was observed following this initial plastic deformation but not before.

Strain hardening behaviour was also studied. Comparing to the traditional torque-torsion method, much higher sensitivity was achieved. Data was fitted with the Ramsberg-Osgood equation to reveal the facts underlying strain hardening and flow stress. Size dependence of the plastic deformation was studied in wires with different diameters and grain sizes. The onset of plastic deformation and subsequent hardening could be related to the combined length-scale of the wire diameter and grain size.

The results in this thesis are important to understanding plasticity in confined volumes and at very low strains. The control of strength by the length-scale of the materials provides a new technique for controlling strength and fatigue resistance in metallic materials.

Acknowledgements

First and foremost, I would like to express my deepest gratitude to my supervisors, Dr. Andy Bushby and Prof. David Dunstan. They taught me everything they knew on both experimental work and theoretical analysis from the first day we met without any reservation. And they also gave me the freedom to explore various results without any objection. I hope that I could be as humorous, knowledgeable, and energetic as them. I really enjoyed the time with them in QM, especially every Tuesday evening!

Besides my supervisors, I would like to thank the rest of my thesis committee: Prof. Xiaoqing Guo and Prof. Angus Wilkinson for their comments on my thesis and broaden my horizon from various perspectives.

I would also like to thank Geoff Gannaway and Geoff Simpson for helping build the experimental devices, Dr. Ken Scott and George Nevill for technical support, Prof. William Gillin for letting us use the Rapid thermal annealing (RTA). Many thanks to Jonathan Hills, Rajesh Chadha and Wei Zhang for their help.

I would extend my thanks to my colleagues Dr. Yiwei Sun, Dominic Carter, Yuan Li, Temur Ahmad and Jonathan Wheatland. Thank you for the help and valuable discussions in the past four years.

I would also like to thank all my friends, Dr. Chen Chen, Dr. Yongfei Cui, Ke Yang, Dr. Zhao Wang, Junyao Yang, Jing Xu, Dr. Yiran An, Menglong Huang, Yi Zhang, Rui Mao, Dr. Hong Liu, Xiang Chen, Dr. Xingyu Han and Dr. Han Zhang, for bearing my mistakes and bad temper.

I would like to give my special thanks to my wife Dr. Fang Mai for being with me. I will never overcome the procrastination without her support.

I would like to thank Chinese government for giving me this precious opportunity to study

abroad and their funding for my living expenses.

Last but not the least, I would like to thank my parents, Shanhai Dong and Zunluo Liu. I will never become myself without their endless love. There is no way to express how much I love them.

| | |
|---|----|
| Declaration..... | 2 |
| Abstract..... | 3 |
| Acknowledgements..... | 4 |
| List of Figure Captions | 10 |
| Introduction..... | 21 |
| 1. Literature review..... | 22 |
| 1.1 Various geometrical size dependence..... | 22 |
| 1.2 Size effects on micro torsion experiments..... | 29 |
| 1.3 Theoretical principles | 40 |
| 1.3.1 Theory on inhomogeneous deformation | 41 |
| 1.3.2 Theory of homogeneous deformation..... | 45 |
| 1.4 Summary | 47 |
| 2. Experiment and Method..... | 49 |
| 2.0 Introduction | 49 |
| 2.1 Sample preparation..... | 50 |
| 2.2 Experiment apparatus | 51 |
| 2.3 Method and principle..... | 52 |
| 2.4 Characterization..... | 57 |
| 2.5 Twist per dislocation..... | 59 |
| 2.6 Problem | 60 |
| 3. High resolution low strain torsion results | 62 |

| | |
|--|----|
| 3.1 Raw data presentation | 63 |
| 3.2 Monotonic loading | 64 |
| 3.2.1 Results of 50 μm diameter copper wire | 64 |
| 3.2.2 Results of 25 μm diameter copper wire | 67 |
| 3.2.3 Result of 20 μm diameter copper wire..... | 70 |
| 3.2.4 Result of 18 μm diameter copper wire..... | 71 |
| 3.3 Reverse loading | 72 |
| 3.3.1 Results of 50 μm diameter copper wire | 72 |
| 3.3.2 Results of 25 μm diameter copper wire | 78 |
| 3.4 Thermal recovery..... | 82 |
| 3.5 Summary | 86 |
| 3.5.1 Sensitivity | 86 |
| 3.5.2 Elastic limit | 86 |
| 3.5.3 Creep | 88 |
| 3.5.4 Recovery | 89 |
| 3.5.5 Cyclic loading (Bauschinger effect) | 89 |
| 4. High strain torsion results | 90 |
| 4.1 Strengthening background of metal materials..... | 90 |
| 4.2 Work hardening background | 91 |
| 4.2.1 Work hardening in singlecrystal | 91 |
| 4.2.2 Work hardening in polycrystals | 92 |

| | |
|--|-----|
| 4.2.3 Work hardening theory..... | 92 |
| 4.3 High strain results..... | 93 |
| 4.3.1 Deformation distribution..... | 93 |
| 4.3.2 Strain hardening | 94 |
| 4.3.3. Creep deformation | 96 |
| 4.4Summary | 102 |
| 4.4.1 Deformation pattern in high strain..... | 102 |
| 4.4.2 Creep | 103 |
| 4.4.3 Theory fitting on high strain | 103 |
| 4.4.4 Length scale | 104 |
| 5. Discussion..... | 105 |
| 5.0 Data comparison with literature | 105 |
| 5.1 Yield points..... | 106 |
| 5.1.1 Elastic limit | 106 |
| 5.1.2 Permanent creep deformation | 107 |
| 5.1.3Appearance of Bauschinger effect..... | 108 |
| 5.1.4Abnormalthermal recovery | 108 |
| 5.1.5 Theory fitting to high strain area | 109 |
| 5.1.6 Engineering yield point..... | 109 |
| 5.2 Size effects..... | 110 |
| 5.2.1 Grain size | 110 |

| | |
|-------------------------------------|-----|
| 5.2.2 Sample size | 110 |
| 5.2.3 Effective length scales | 111 |
| 6. Conclusion | 116 |
| Publications..... | 117 |
| References..... | 118 |

List of Figure Captions

| | |
|---|----|
| Figure 1.1 Tension and torsion response of copper wire of diameter from 12-170 μm , where a is the wire radius, σ is the true stress in tension, ϵ is the logarithmic strain of tension, Q is the torque in torsion and κ is the twist per unit length (Reproduced from Fleck, 1994). | 23 |
| Figure 1.2 The normalized bending moment against the surface strain for three foil thicknesses of pure nickel, where h is the film thickness (Reproduced from Stölken and Evans, 1998). | 24 |
| Figure 1.3 The variation in the mean normal indentation pressure P_m , with a/R where a and R are the radii of indentation and the indenter respectively, for annealed OFC, determined using spherical indenters of radii 7, 30, 200 and 500 μm (Reproduced from Lim and Chaudhri, 1999). | 25 |
| Figure 1.4 Mechanical behaviour for pure Ni microsamples having a $\langle 134 \rangle$ orientation (A) Stress-strain curves for microsamples ranging in size from 5 to 40 μm in diameter, as well as the stress-strain curve for a bulk single crystal having approximate dimensions 2.6 \times 2.6 \times 7.4 mm. (B) A scanning electron micrograph (SEM) image of a 20 μm diameter sample tested to about 4% strain. (C) A SEM image of 5 μm diameter sample after testing, where the sample achieved about 19% strain during a rapid burst of deformation that occurred in less than 0.2s (Reproduced from Uchic et al., 2004). | 26 |
| Figure 1.5 Stress-strain plots comparing membrane width (2.5, 5.0, 10.0, and 20.0 μm) for an Au films 0.3 (a) 0.5 (b) and 1.0 μm (c) thickness (Reproduced from H.D. Espinosa et al., 2004). | 27 |
| Figure 1.6 Stress-strain plots comparing film thickness (0.3, 0.5, and 1.0 μm thick) for Au membrane widths of 2.5 (a), 5.0 (b), 10.0 (c), and 20.0 μm (d). The vertical bars on each signature represent the data scatter over five identically sized membranes (Reproduced from | |

| | |
|---|----|
| H.D. Espinosa et al., 2004). | 28 |
| Figure 1.7 Schematic of the Fleck torsion device (Reproduced from Fleck et al., 1994) | 29 |
| Figure 1.8 Photograph of a wire torsion experiment (Reproduced from Lu and Song, 2011) | 30 |
| Figure 1.9 Resultant torsional curves of the copper wires with different diameters, where normalized torque and rotation are used for comparing the deformation behaviour of specimens with various sizes (Reproduced from Lu and Song, 2011) | 31 |
| Figure 1.10 Normalized torque rotation curves of copper wires with different diameters, where normalized torque and rotation are used for comparing the deformation behaviour of specimens with various sizes (Reproduced from Lu and Song, 2015) | 32 |
| Figure 1.11 Schematic of Walter and Kraft torsion measuring principle (Reproduced from Walter and Kraft, 2011). | 33 |
| Figure 1.12 Cyclic torsion response of 40 μm diameter gold wire, where M_t is the torsion moment and γ is the surface strain (Reproduced from Walter and Kraft, 2011). | 33 |
| Figure 1.13 Monotonic torsion response of 10 μm diameter gold wire with one or two sensors, where M_t is the torsion moment (Reproduced from Walter and Kraft, 2011). | 34 |
| Figure 1.14 Torsional response of the wires against gradient, where D is the wire diameter, κ is the strain gradient and τ is the shear stress (Reproduced from Chen et al., 2015). | 35 |
| Figure 1.15 Hall-Petch behaviour of the wires with respect to the 0.2% proof stress in both tension and torsion, where D is the wire diameter (Reproduced from Chen et al., 2015). | 35 |
| Figure 1.16 Schematic illustration of Liu torsion test apparatus (Reproduced from Liu et al., 2013). | 36 |
| Figure 1.17 Torsional responses of copper wires with diameters from 20 to 50 μm (Reproduced from Liu et al., 2013). | 36 |
| Figure 1.18 Comparisons of experimental data at yield point for copper wires in torsion and the various theoretical curves (Reproduced from Liu et al., 2013) | 37 |

| | |
|---|----|
| Figure 1.19 Cyclic torsion data of the Cu wires with $2a = 18, 35, \text{ and } 42 \mu\text{m}$ for the initial loading cycles, where a is the wire radius. The yield points in the forward and reverse directions are marked by circles. The wires show significant Bauschinger and size effects (Reproduced from Liu et al., 2013). | 38 |
| Figure 1.20 Torsional responses of gold wires at different annealing temperatures. (a) and (b) are respectively the torsional results of gold wires of diameter $2a = 20$ and $50 \mu\text{m}$ annealed in the temperature range $330 - 750^\circ\text{C}$. (c) Torsional response of quasi-single crystal wires of diameter $2a = 20$ and $50 \mu\text{m}$, where Q is the torque (Reproduced from Gan et al., 2014)..... | 39 |
| Figure 1.21 Load-unload data in torsion for three wires, (a) a $10 \mu\text{m}$ diameter wire with an average grain size of $d = 11 \mu\text{m}$ and length 0.26 m , (b) a $50 \mu\text{m}$ diameter wire with an average grain size of $d = 8.4 \mu\text{m}$ and length 1 m (open triangles), and (c) a $50 \mu\text{m}$ diameter wire with an average grain size of $d = 21 \mu\text{m}$ and length 1 m . The solid curves are critical thickness theory fitting (Reproduced from Dunstan et al. 2009)..... | 40 |
| Figure 1.22 Geometrically-necessary dislocations created by a rigid conical indenter. The dislocation structure is idealized as circular dislocation loops, where θ is the angle between the surface of the indenter and the plane of the surface, a is the contact radius and h is the depth of indentation (Reproduced from Nix & Gao, 1998)..... | 42 |
| Figure 1.23 The elastic strain energy E_s increases in proportion to the strained layer thickness, but the energy of a misfit dislocation E_{disloc} rises more slowly. Critical thickness h_c is defined by the crossing of these two lines (Reproduced from Dunstan, 1996)..... | 44 |
| Figure 1.24 Flow stress at 10% strain vs. pillar diameter plotted on log-log scale (Reproduced from Greer et al. 2005)..... | 46 |
| Figure 2.1 Schematic representation of the apparatus for torsion testing..... | 51 |
| Figure 2.2 Loading-unload principle in wire torsion | 53 |

| | |
|--|----|
| Figure 2.3 Schematic of the load-unload method for measuring the surface shear strain and its elastic and plastic strain components..... | 55 |
| Figure 2.4 Grain size for all annealing conditions..... | 58 |
| Figure 2.5 Grain distribution of the wire in Figure 3.1 over 1 mm length. Inset, FIB microscopy of the wire surface showing the grains strongly contrasted by their crystal orientation. | 59 |
| Figure 3.1 An example of the raw data from the first forward (1F) loading of a wire. The unload angle is plotted against the load angle. The dots (•) are the successive load-unload data points. Creep test data are indicated by the red, green, blue and black crosses, which represent successive loading for 2, 4, 8 and 15 minutes. Thermal-induced plastic recovery data are indicated by the yellow, orange and purple squares, which represent for successive heating to 100, 200 and 300 °C. The inset shows the data during creep and thermal recovery at a load angle of 420°..... | 64 |
| Figure 3.2 Plastic strain vs total torsional strain for a copper wire of 50 μm diameter, 1 m length, annealed at 850 °C 60s, grain size 12 μm. The black dots • are the successive load-unload data points for 1F loading. Creep test data are indicated by the red, green, blue and black crosses, which represent successive loading for 2, 4, 8 and 15 minutes..... | 65 |
| Figure 3.3 Plastic strain vs total torsional strain for a copper wire of 50 μm diameter, 1 m length, annealed at 650 °C 30s, grain size 3.3 μm. The black dots • are the successive load-unload data points for 1F loading. Creep test data are indicated by the red, green, blue and black crosses, which represent successive loading for 2, 4, 8 and 15 minutes..... | 66 |
| Figure 3.4 Plastic strain vs total torsional strain for a copper wire of 50 μm diameter, 1 m length, annealed at 500 °C 30s, grain size 2.6 μm. The black dots • are the successive load-unload data points for 1F loading. Creep test data are indicated by the red, green, blue and | |

| | |
|---|----|
| black crosses, which represent successive loading for 2, 4, 8 and 15 minutes..... | 67 |
| Figure 3.5 Plastic strain vs total torsional strain for a copper wire of 25 μm diameter, 0.5 m length, annealed at 800 $^{\circ}\text{C}$ 90s, grain size 10 μm . The black dots • are the successive load-unload data points for 1F loading. Creep test data are indicated by the red, green, blue and black crosses, which represent successive loading for 2, 4, 8 and 15 minutes..... | 68 |
| Figure 3.6 Plastic strain vs total torsional strain for a copper wire of 25 μm diameter, 0.5 m length, annealed at 750 $^{\circ}\text{C}$ 30s, grain size 3.6 μm . The black dots • are the successive load-unload data points for 1F loading. Creep test data are indicated by the red, green, blue and black crosses, which represent successive loading for 2, 4, 8 and 15 minutes..... | 69 |
| Figure 3.7 Plastic strain vs total torsional strain for a copper wire of 25 μm diameter, 0.5 m length, annealed at 650 $^{\circ}\text{C}$ 15s, grain size 3.2 μm . The black dots • are the successive load-unload data points for 1F loading. Creep test data are indicated by the red, green, blue and black crosses, which represent successive loading for 2, 4, 8 and 15 minutes..... | 70 |
| Figure 3.8 Plastic strain vs total torsional strain for a copper wire of 20 μm diameter, 0.5 m length, annealed at 750 $^{\circ}\text{C}$ 120s, grain size 7.7 μm . The black dots • are the successive load-unload data points for 1F loading. Creep test data are indicated by the red, green, blue and black crosses, which represent successive loading for 2, 4, 8 and 15 minutes..... | 71 |
| Figure 3.9 Plastic strain vs total torsional strain for a copper wire of 18 μm diameter, 0.25 m length, annealed at 650 $^{\circ}\text{C}$ 90s, grain size 6.5 μm . The black dots • are the successive load-unload data points for 1F loading. | 72 |
| Figure 3.10 Plastic strain vs total torsional strain for a copper wire of 50 μm diameter, 1 m length, annealed at 850 $^{\circ}\text{C}$ 60s. The black dots • are the successive load-unload data points for 1F loading and blue triangle ▲ are the load-unload data for first reversal (2B) loading. Creep test data are indicated by the red, green, blue and black crosses, which represent successive loading for 2, 4, 8 and 15 minutes..... | 73 |

Figure 3.11 Plastic strain vs total torsional strain for a copper wire of 50 μm diameter, 1 m length, annealed at 850 $^{\circ}\text{C}$ 60s. The brown dots • are the successive load-unload data points for 3F loading and cyan rhombus ♦ are the load-unload data for second reversal (4B) loading. Creep test data are indicated by the red, green, blue and black crosses, which represent successive loading for 2, 4, 8 and 15 minutes.....74

Figure 3.12 Plastic strain vs total torsional strain for a copper wire of 50 μm diameter, 1 m length, annealed at 650 $^{\circ}\text{C}$ 30s. The black dots • are the successive load-unload data points for 1F loading and blue triangle ▲ are the load-unload data for first reversal (2B) loading. Creep test data are indicated by the red, green, blue and black crosses, which represent successive loading for 2, 4, 8 and 15 minutes.....75

Figure 3.13 Plastic strain vs total torsional strain for a copper wire of 50 μm diameter, 1 m length, annealed at 650 $^{\circ}\text{C}$ 30s. The brown dots • are the successive load-unload data points for 3F loading and cyan rhombus ♦ are the load-unload data for second reversal (4B) loading. Creep test data are indicated by the red, green, blue and black crosses, which represent successive loading for 2, 4, 8 and 15 minutes.....76

Figure 3.14 Plastic strain vs total torsional strain for a copper wire of 50 μm diameter, 1 m length, annealed at 500 $^{\circ}\text{C}$ 30s. The black dots • are the successive load-unload data points for 1F loading and blue triangle▲ are the load-unload data for first reversal (2B) loading. Creep test data are indicated by the red, green, blue and black crosses, which represent successive loading for 2, 4, 8 and 15 minutes.....77

Figure 3.15 Plastic strain vs total torsional strain for a copper wire of 50 μm diameter, 1 m length, annealed at 500 $^{\circ}\text{C}$ 30s. The brown dots • are the successive load-unload data points for 3F loading and cyan rhombus ♦ are the load-unload data for second reversal (4B) loading. Creep test data are indicated by the red, green, blue and black crosses, which represent successive loading for 2, 4, 8 and 15 minutes.....78

Figure 3.16 Plastic strain vs total torsional strain for a copper wire of 25 μm diameter, 0.5 m length, annealed at 750 °C 30s. The black dots • are the successive load-unload data points for 1F loading and blue triangle▲ are the load-unload data for first reversal (2B) loading. Creep test data are indicated by the red, green, blue and black crosses, which represent successive loading for 2, 4, 8 and 15 minutes.....79

Figure 3.17 Plastic strain vs total torsional strain for a copper wire of 25 μm diameter, 0.5 m length, annealed at 750 °C 30s. The brown dots • are the successive load-unload data points for 3F loading and cyan rhombus ◆ are the load-unload data for second reversal (4B) loading. Creep test data are indicated by the red, green, blue and black crosses, which represent successive loading for 2, 4, 8 and 15 minutes.....80

Figure 3.18 Plastic strain vs total torsional strain for a copper wire of 25 μm diameter, 0.5 m length, annealed at 650 °C 15s. The black dots • are the successive load-unload data points for 1F loading and blue triangle▲ are the load-unload data for first reversal (2B) loading. Creep test data are indicated by the red, green, blue and black crosses, which represent successive loading for 2, 4, 8 and 15 minutes.....81

Figure 3.19 Plastic strain vs total torsional strain for a copper wire of 25 μm diameter 0.5 m length, annealed at 650 °C 15s. The brown dots • are the successive load-unload data points for 3F loading and cyan rhombus ◆ are the load-unload data for second reversal (4B) loading. Creep test data are indicated by the red, green, blue and black crosses, which represent successive loading for 2, 4, 8 and 15 minutes.....82

Figure 3.20 Plastic strain vs total torsional strain for a copper wire of 50 μm diameter, 1 m length, average grain size 8 μm . The black dots • are the successive load-unload data points for 1F loading. Creep test data are indicated by the red, green, blue and black crosses, which represent successive loading for 2, 4, 8 and 15 minutes. Thermally-induced plastic recovery data are indicated by the yellow, orange and purple squares, which represent successive

heating to 100, 200 and 300°C.....83

Figure 3.21 Plastic strain vs total torsional strain for a copper wire of 50 μm diameter 1 m length, average grain size is 8 μm . The black, brown and pink dots • are the successive load-unload data points for forwards loading and blue ▲, cyan ◆ and grey ▼ are the successive load-unload data points for reverse loading. Creep test data are indicated by the red, green, blue and black crosses, which represent successive loading for 2, 4, 8 and 15 minutes. Thermally-induced plastic recovery data are indicated by the yellow, orange and purple squares, which represent successive heating to 100, 200 and 300°C. a) first forward 1F and reverse 2B cycles, b) second forwards 3F and reverse 4B cycles, c) third forwards 5F and reverse 6B cycles.85

Figure 3.22 Yield strain (elastic sensitivity limit) versus grain size and wire radius (sample size) in low strain.....88

Figure 4.1 Three stages of stress–strain curve in single crystal (Reproduced from Modern physical metallurgy and materials engineering, 1999)92

Figure 4.2 A wire taken to unity strain (50 μm diameter copper wire, 1m length, annealed at 850 °C for 60s , average grain size is about 20 μm). The dot symbols and squares are data for 2 different 20cm sections of the wire, 5F and 6F, taken to high strain. The red, green, blue and black crosses indicate creep under 2 minutes, 4 minutes, 8 minutes and 15 minutes load.....94

Figure 4.3 Five wires were taken to 1000 $\mu\epsilon$ total strain. The black dot • symbols are 50 μm diameter copper wire, 1m length, annealed at 850 °C for 60s, grain size 12 μm ; the blue triangle ▲ symbols are 50 μm diameter copper wire, 1m length, annealed at 650 °C for 30s, grain size 3.3 μm ; the red square◻ symbols are 25 μm diameter copper wire, 0.5m length, annealed at 750 °C for 30s, grain size 3.6 μm ; the green rhombus◊ symbols are 25 μm diameter copper wire, 0.5m length, annealed at 800 °C for 90s, grain size 10 μm ; the purple

inverted triangle ▼ symbols are 18 μm diameter copper wire, 0.25m length, annealed at 600 °C for 90s, grain size 6.5 μm95

Figure 4.4 The wires of Figure 4. 3 taken to unity strain. The black dot • symbols are 50 μm diameter copper wire, 1m length, annealed at 850 °C for 60s, grain size 12 μm ; the blue triangle ▲ symbols are 50 μm diameter copper wire, 1m length, annealed at 650 °C for 30s, grain size 3.3 μm ; the red square □ symbols are 25 μm diameter copper wire, 0.5m length, annealed at 750 °C for 30s, grain size 3.6 μm ; the green rhombus ◊ symbols are 25 μm diameter copper wire, 0.5m length, annealed at 800 °C for 90s, grain size 10 μm ; the purple inverted triangle ▼ symbols are 18 μm diameter copper wire, 0.25m length, annealed at 600 °C for 90s, grain size 6.5 μm96

Figure 4.5 Creep deformation of the wires in Figure 4.4 are shown in the same log-log coordinate system. Red, green, blue and black symbols indicate creep under 2 minutes, 4 minutes, 8 minutes and 15 minutes load. The × symbol is 50 μm diameter copper wire, 1m length, annealed at 850 °C for 60s, grain size 12 μm ; the • symbol is 50 μm diameter copper wire, 1m length, annealed at 650 °C for 30s, grain size 3.3 μm ; the ▲ symbols is 25 μm diameter copper wire, 0.5m length, annealed at 750 °C for 30s, grain size 3.6 μm ; the ▼ symbols is 25 μm diameter copper wire, 0.5m length, annealed at 800 °C for 90s, grain size 10 μm ; the ■ symbols is 18 μm diameter copper wire, 0.25m length, annealed at 600 °C for 90s, grain size 6.5 μm97

Figure 4.6 Creep strain rate versus elastic strain98

Figure 4.7 Ramberg-Osgood fitting for 50 μm diameter copper wire (a), (b),(c) and 25 μm diameter copper wire (d), (e), (f). The solid blue line is WK model, fitted over the whole range of the data; the red dashing line is σ_0 model, fitted over the range excluding the data below the yield strength; the dashed blue line is WK Low model, fitted only over the low strain data. All three models are plotted in three different scales: (a), (d) are in the range of

| | |
|--|-----|
| strain from 0 to 0.7; (b), (e) are in the range of strain from 0 to 7000 $\mu\epsilon$; (c) is in the range of strain from 0 to 1200 $\mu\epsilon$ for 50 μm diameter copper wire and (f) is in the range of strain from 0 to 630 $\mu\epsilon$ for 25 μm diameter copper wire. | 100 |
| Figure 4.8 Elastic strain of various mechanical tests versus effective size, where open symbols for pillar compression, solid circles for InGaAs layers and for polycrystalline Cu wire in torsion, (+) for foils in flexure and (\times) for wire in tension and (open rectangle) for tungsten nanofoams, where a_0 is the lattice parameter. (Reproduced from Dunstan and Bushby, 2013) | 102 |
| Figure 5.1 Comparisons between our data and Walter & Kraft data, black dots are our data and blue triangles are schematic representation of the data of Walter & Kraft and its scatter. | 105 |
| Figure 5.2 Comparisons between our data and Fleck's data. Black dots are our data (50 μm diameter copper wire, grain size 12 μm). Red dashed line and blue solid line are schematic representation of the data of Fleck's data (30 μm diameter copper wire, grain size 30 μm and 15 μm diameter copper wire, grain size 15 μm). | 106 |
| Figure 5.3 Yield strain (elastic limit) versus combined length scale at low strain | 111 |
| Figure 5.4 Yield strain by elastic limit versus combined length scale at strain up to 1000 $\mu\epsilon$ | 112 |
| Figure 5.5 Yield strain by elastic limit versus combined length scale at high strain up to unit strain..... | 112 |
| Figure 5.6 Yield strain by elastic limit versus inverse square root grain size at high strain up to unit strain. | 113 |
| Figure 5.7 Yield strain by elastic limit versus inverse wire radius at high strain up to unit strain..... | 113 |

| | |
|---|-----|
| Figure 5.8 Yield strain by elastic limit versus inverse wire radius at high strain up to unit strain..... | 114 |
| Table 1 Ramberg-Osgood fitting parameters on various sample sizes and grain sizes | 101 |
| Table 2 Table of the definitions for all the yield points | 110 |

Introduction

Understanding the mechanical behaviour of materials is crucial in materials science. When the sizes of materials external dimension and microstructure are down to micrometer or nanometer scales, the classical plasticity models are no longer effective. The strength of a material increases when the structure is small or when only a small volume is deformed. The term ‘size effect’ is used generically to cover all the cases in which this may happen. A large quantity of size effects are reported over the past fifty years, such as wire twisting [1], foil bending [2], nanoindentation [3] and pillar compression[4]. However, the physics behind these size effects is still not fully understood.

This thesis comprises studies of thin wire torsion experiments using the load-unload method in micron scales, as the existing data does not have enough resolution to display the changes at micro-strain scale. The most cited explanation of size effects is strain gradient plasticity (SGP) but it could not account for the size effects with no strain gradient. Characterising and understanding deformation is important at the first departures from elastic behaviour, since structural failure is usually a consequence of exceeding the elastic limit. Another motivation is that the interaction between microstructural (grain size) and external (sample size) size effects are rarely reported both in experiments and in theories.

This thesis is divided into 6 Chapters; the first two chapters introduce the background and experimental method. Chapters 3 and 4 describe the experimental data in the low strain and high strain areas. Chapters 5 and 6 are discussion and summary.

1. Literature review

The classical strengthening theories do not work well on micro and nano-scales materials since there is no length scale to give a size effect. Research is needed to build multi-scale plasticity theories for the applications from the biomedical to the semiconductor industry. Different from the classic strengthening theory, the mechanism of the small size materials, which mainly focuses on the microstructural constraints and external dimension constraints, is not fully understood and needed to be explored. The microstructural constraints could be due to particle size, such as the Hall-Petch effect [5, 6] on grain size. The dimensional constraints are decided by external sample sizes, such as wire diameter in twisting, plastic deformation zone in indentation, thickness of bending foils, diameter of pillars under compression *etc.* Some major phenomena and theories are reviewed separately below.

1.1 Various geometrical size dependence

The size effects have now been observed in various geometries, such as shear in wire twisting [1], uniaxial foil bending [2], complicated strain gradients in nano indentation [3] and uniaxial micro-pillar compression [4]. The classic wire torsion experiment was carried out by Fleck *et al.* [1]. They observed strong size effects in microscale torsion experiment on annealed polycrystalline copper wires, with diameters ranged from 15 to 170 μm , grain sizes from 5 to 25 μm . Details will be discussed in Section 1.2.

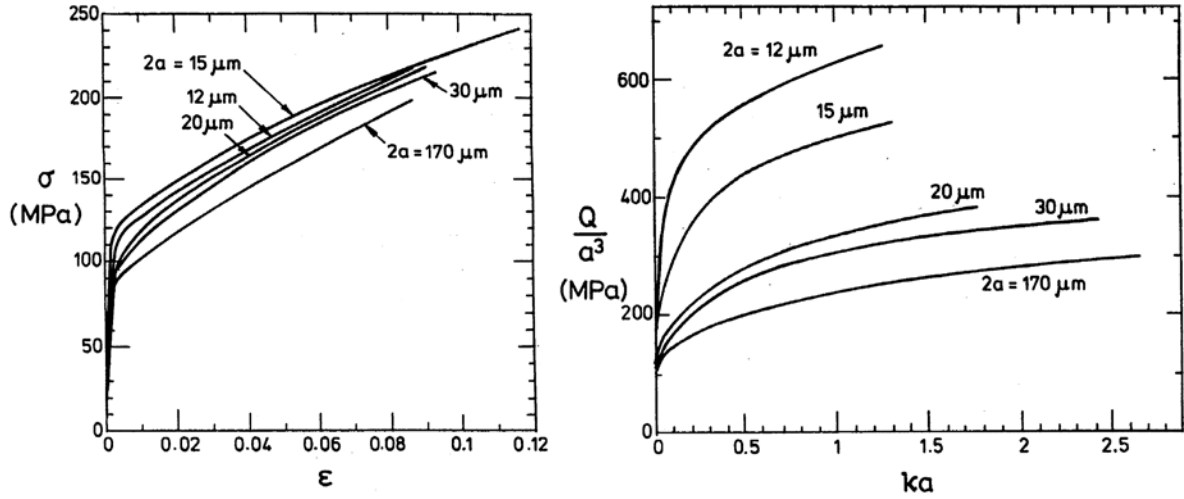


Figure 1.1 Tension and torsion response of copper wire of diameter from 12-170 μm , where a is the wire radius, σ is the true stress in tension, ϵ is the logarithmic strain of tension, Q is the torque in torsion and κ is the twist per unit length (Reproduced from Fleck, 1994).

Comparing to the tensile results, which are nearly independent on wire diameters, strong size effects were found on the torsion experiment, see Figure 1.1. Therefore Fleck *et al.* attributed these differences to the strain gradient plasticity associated with the geometrically necessary dislocations.

Stölken and Evans [2] created a load-unload method for a nickel micro-bend experiment for obtaining the plasticity length scale, see Figure 1.2. In the load-unload method, the foil is bent to some curvature and then unloaded to another curvature. The bending moment could be determined by the change of the curvature. Only the radii of foil curvature and the Young's modulus of the sample needed to be measured, avoiding the difficulties of direct measurement of the stress-strain data. Their results clearly showed that thinner foil had greater strength at large plastic strain. However, the grain size effect was not discussed in detail in their analysis and the error bars were large.

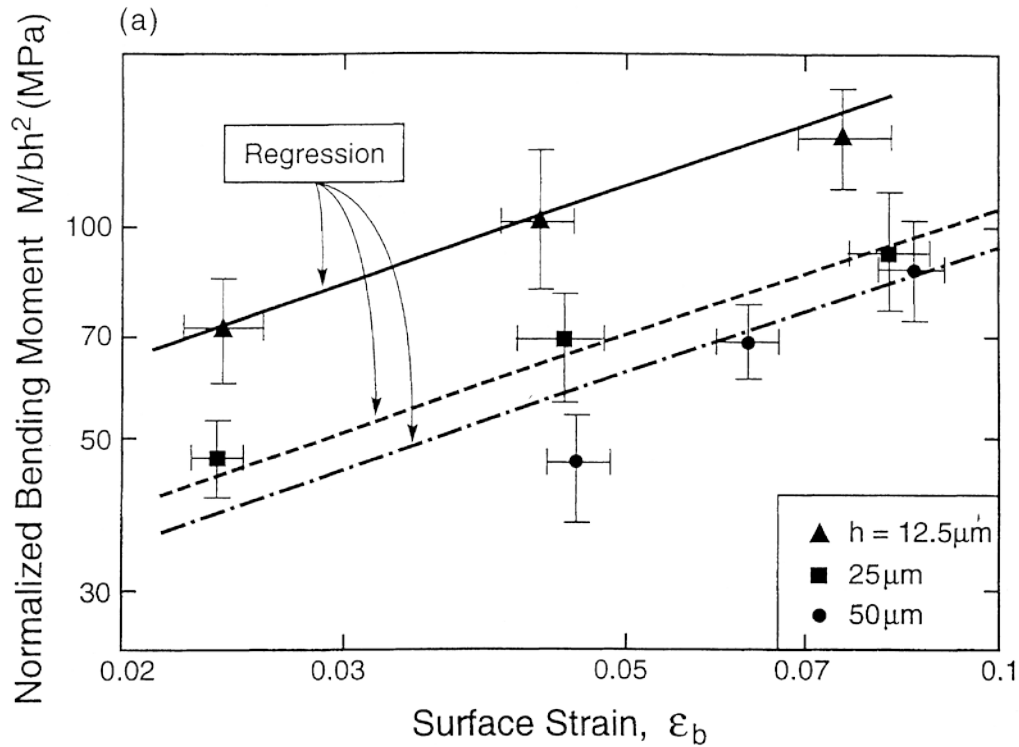


Figure 1.2 The normalized bending moment against the surface strain for three foil thicknesses of pure nickel, where h is the film thickness (Reproduced from Stölken and Evans, 1998).

Nano indentation is a good candidate to test the stress-strain behaviours of materials. It is a practically non-destructive test method since the investigations need only be carried out on small specimens only a few micrometers across and elastic deformation could be fully recovered on unloading by the spherical or pointed indenter. Therefore the complete elastic-plastic transition and yield behaviour could be measured. Lim and Chaudhri [7] observed clear entire flow curves on oxygen-free copper for spherical indenter, see Figure 1.3. For smaller indenters, the pressure increased as diameter of indenter decreased. However, there are still difficulties in measuring the actual deformation zone and in defining the boundary of the contact area, especially when the indent is shallow.

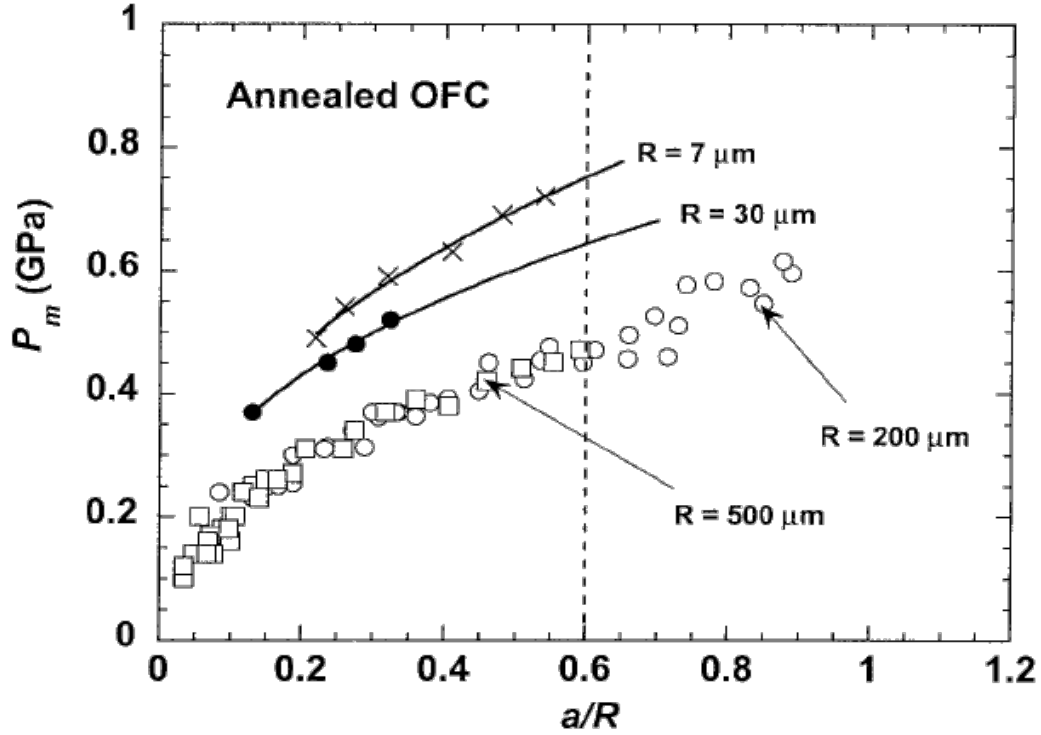


Figure 1.3 The variation in the mean normal indentation pressure P_m , with a/R where a and R are the radii of indentation and the indenter respectively, for annealed OFC, determined using spherical indenters of radii 7, 30, 200 and 500 μm (Reproduced from Lim and Chaudhri, 1999).

Since the development of focused ion beam (FIB) machining and *in-situ* testing in electron microscopes such as scanning electron microscopy (SEM), transmission electron microscopy (TEM) and atomic force microscopy (AFM), the emphasis in experimental work has largely been on micron-sized specimens, principally in compression, but also in tension and in bending of cantilevers. Such experiments need use high resolution systems for displacements and force measurements for precise mechanical characterization.

Uchic *et al.* [4] adopted the FIB microscope for specimen preparation, using a modified nano indentation flat-punch indenter, on micron-sized pure Ni and Ni alloy pillars under uniaxial compression. When the sample size was decreased below 10 μm , a distinct increase in yield stress occurred comparing to the 20 and 40 μm diameters, which are quite similar to the bulk material data, see Figure 1.4. Grain boundaries to hinder the dislocations' movement were

removed since they used single crystal Ni. They observed dramatic external dimension size effects.

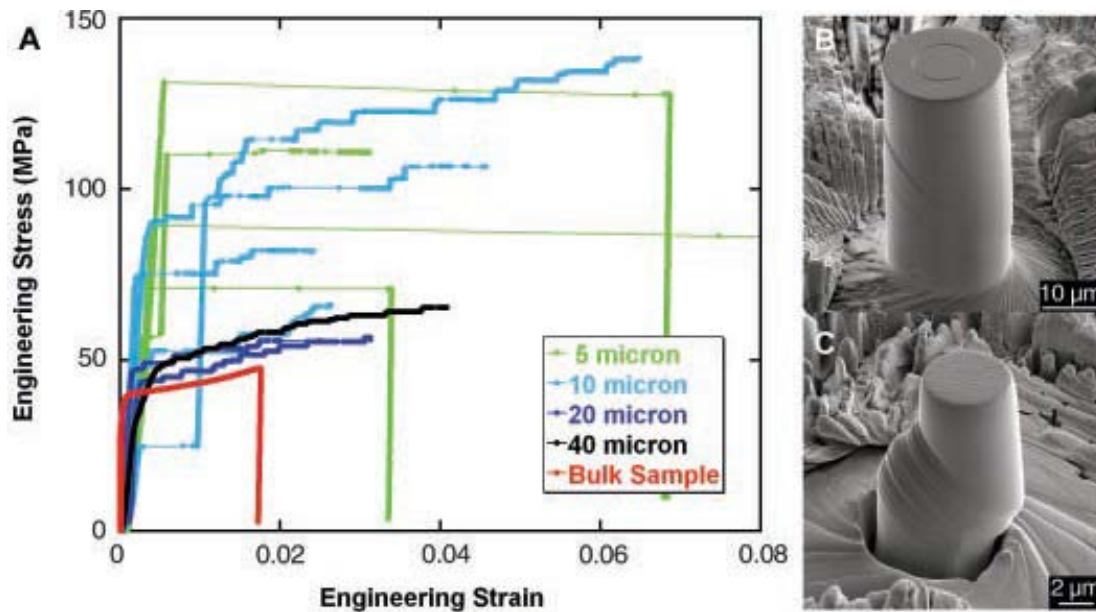


Figure 1.4 Mechanical behaviour for pure Ni microsamples having a $\langle 134 \rangle$ orientation (A) Stress-strain curves for microsamples ranging in size from 5 to 40 μm in diameter, as well as the stress-strain curve for a bulk single crystal having approximate dimensions $2.6 \times 2.6 \times 7.4$ mm. (B) A scanning electron micrograph (SEM) image of a 20 μm diameter sample tested to about 4% strain. (C) A SEM image of 5 μm diameter sample after testing, where the sample achieved about 19% strain during a rapid burst of deformation that occurred in less than 0.2s (Reproduced from Uchic et al., 2004).

Espinosa *et al.* [8] observed the increased yield stress with decreased film thickness and width, on micron-scale gold films in pure tension tests to avoid strain gradient, see Figure 1.5 and Figure 1.6. The specimens were prepared by FIB. Similar plasticity size effects were also observed in Cu and Al.

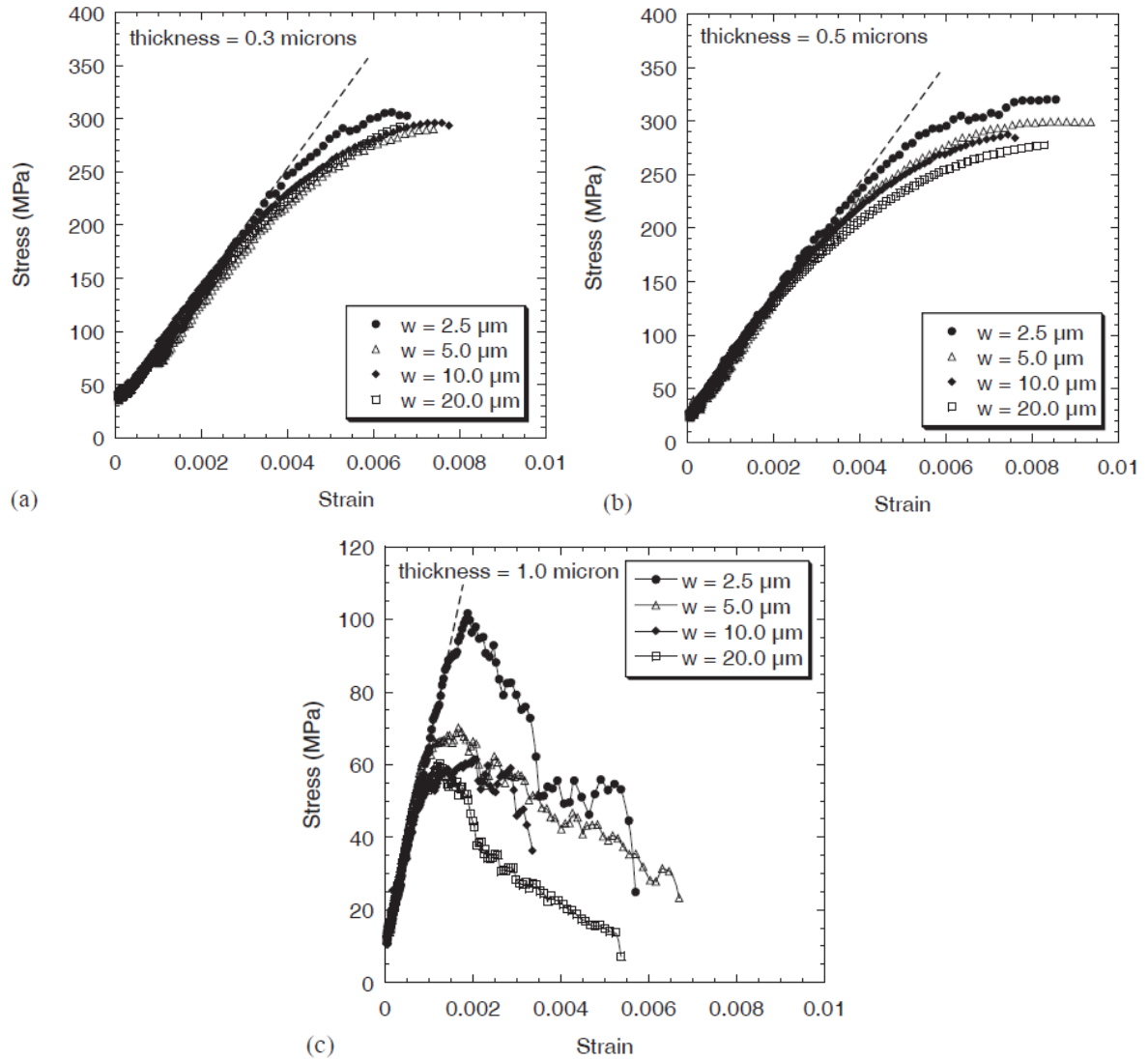


Figure 1.5 Stress-strain plots comparing membrane width (2.5, 5.0, 10.0, and 20.0 μm) for an Au films 0.3 (a) 0.5 (b) and 1.0 μm (c) thickness (Reproduced from H.D. Espinosa et al., 2004).

With fixed thickness, the width of the samples did have a moderate effect on film strength. Below 1 μm thickness, the 2.5 μm width specimen showed a relatively larger yield stress than the larger width data. The curves of width above 2.5 μm are quite similar. For 1 μm thickness, the flow stress at various widths showed a sharp drop with increase in deformation.

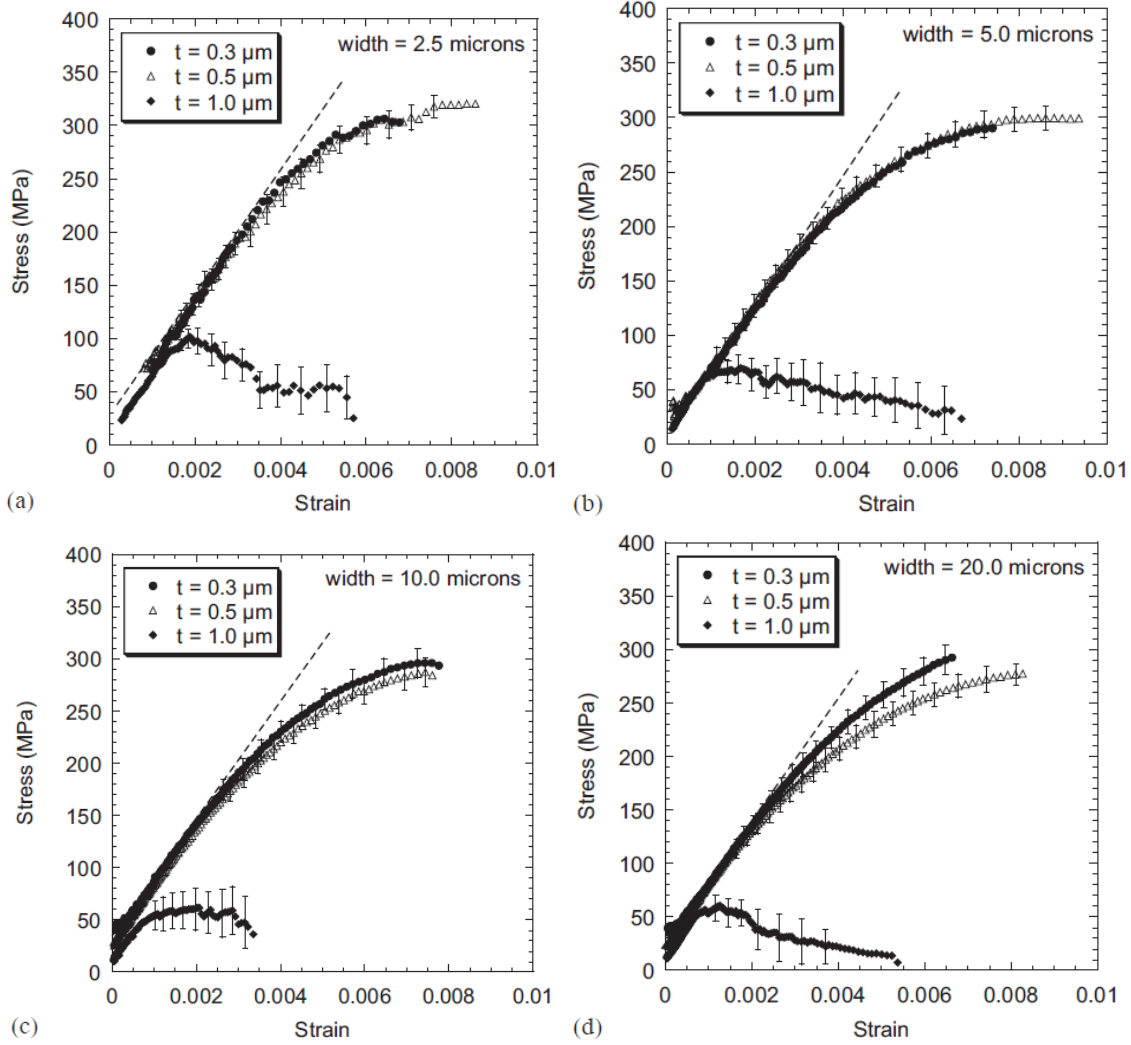


Figure 1.6 Stress-strain plots comparing film thickness (0.3, 0.5, and 1.0 μm thick) for Au membrane widths of 2.5 (a), 5.0 (b), 10.0 (c), and 20.0 μm (d). The vertical bars on each signature represent the data scatter over five identically sized membranes (Reproduced from H.D. Espinosa et al., 2004).

When they compared the data against fixed width, the thickness effect became much clearer. Smaller thickness (0.3 and 0.5 μm) samples showed significantly higher yield stress than the larger one (1 μm) at various widths. They combined the effects of increase in the number of grains across the width and through the thickness to relax statistical and geometrical constraints on the deformation mechanism to account for the differences of flow stress.

1.2 Size effects on micro torsion experiments

Among all the micromechanical tests, torsion is the most sensitive method since very low strain can be observed in long wires at measurable angles of twist. Since there is a strain gradient from zero strain on the centre of the wire to the maximum strain at the surface, torsion experiments, like foil-bending experiments, should be sensitive to any strain gradient effects [9].

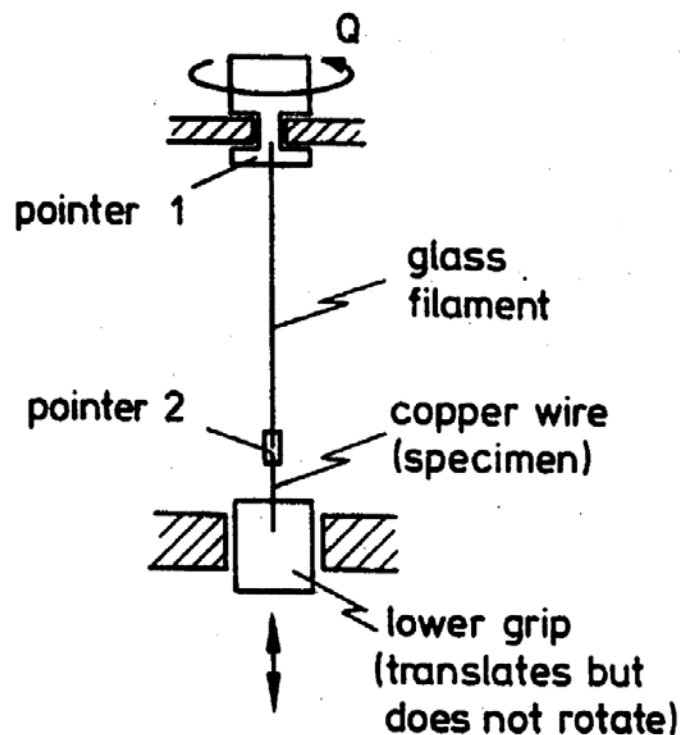


Figure 1.7 Schematic of the Fleck torsion device (Reproduced from Fleck *et al.*, 1994)

In the classic experiment of Fleck *et al.* [1], the torsion test was carried out by twisting the specimen in series with a glass filament that acted as torque load cell, see Figure 1.7. Pointers indicated the total twist and the amount undergone by the specimen. The diameter of the polycrystalline copper wire specimens ranged from 12 to 170 μm and the gauge length was 2 mm. All the wires were annealed, producing grain sizes between 5 to 25 μm . A strong size effect in torsion was observed: at a normalised torsion of $\kappa a = 1$ the normalised torque Q/a^3 for the 12 μm diameter wire was about three times greater than for the 170 μm diameter

wire, see Figure 1.1. If the constitutive law were independent of strain gradient, plots of Q/a^3 against κa for different diameter wires would all lie upon the same curve. No such significant difference in strength was observed in the same wires in uniaxial tension testing. It was therefore proposed that strain hardening was controlled by total dislocation densities, which in torsion include a geometrically-necessary dislocation (GND) density proportional to the strain gradient. In tension, hardening would be the result of statistically stored dislocations with no strain gradient. Therefore the flow stress under strain-hardening depends both on strain and on strain gradient.

It may be commented that the data presented does not have the resolution to display the elastic regime or the elastic-plastic transition. With a gauge length of only 2 mm, this was probably because of inadequate resolution in the measurement of the torsion of the specimen.

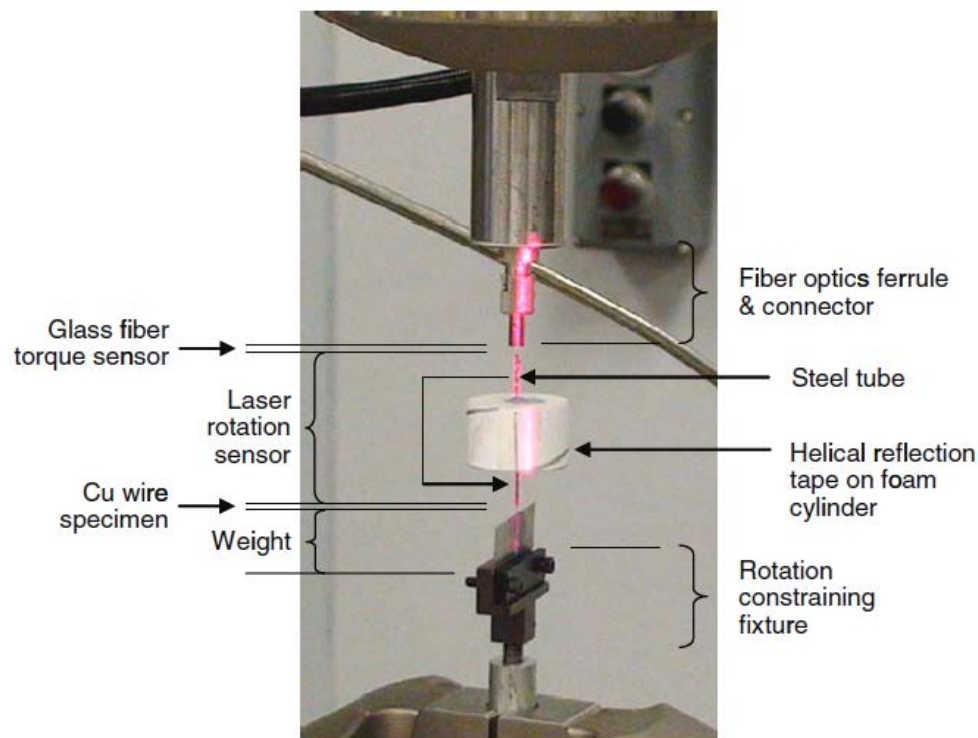


Figure 1.8 Photograph of a wire torsion experiment (Reproduced from Lu and Song, 2011)

Lu and Song [10] improved upon the experiment of Fleck *et al.* by using a laser rotation sensor to measure the rotation angle of the glass fibre torque cell (see Figure 1.8). In this way,

their angular resolution was sufficient, with gauge lengths 1 – 3.2 mm, to display the elastic part of the torque-torsion curve, for wires from 16 to 180 μm , in the strain range 0 – 10^{-3} . However, the transition from elastic to plastic was not affected significantly by the wire diameter, see Figure 1.9.

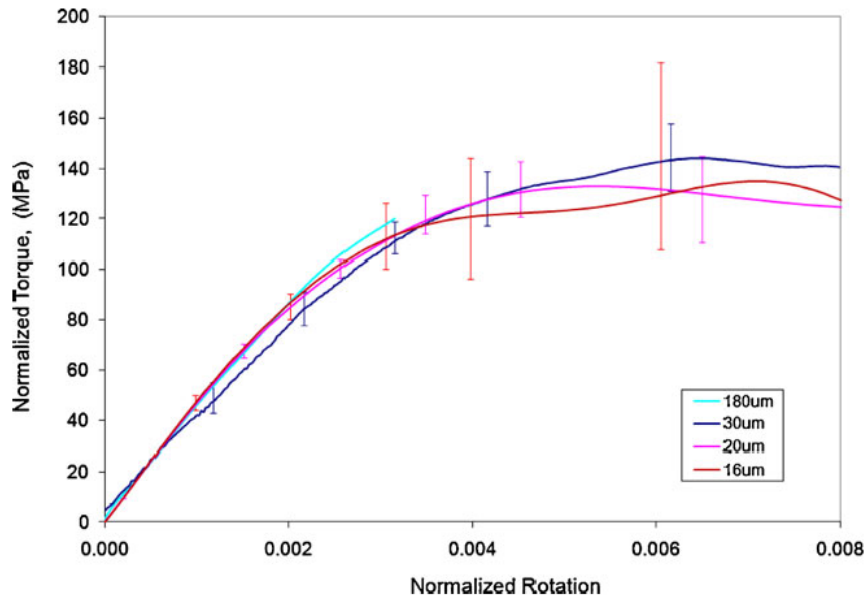


Figure 1.9 Resultant torsional curves of the copper wires with different diameters, where normalized torque and rotation are used for comparing the deformation behaviour of specimens with various sizes (Reproduced from Lu and Song, 2011)

Later Lu and Song [11] reported improvements to their experiment, in which a force sensor device is used to increase the resolution. This time they got direct measurement of small torques in the torsion test with constant shear strain rate and removing any misalignment issue. The results on wires of diameter from 12 to 30 μm fitted the theoretical elastic line in the elastic region. It is interesting that they observe no significant size effect with little work-hardening, see Figure 1.10. However, it may be that size effects were swamped by the high strength due to the small grain size of their wires, reported to be 3.2 - 6.4 μm .

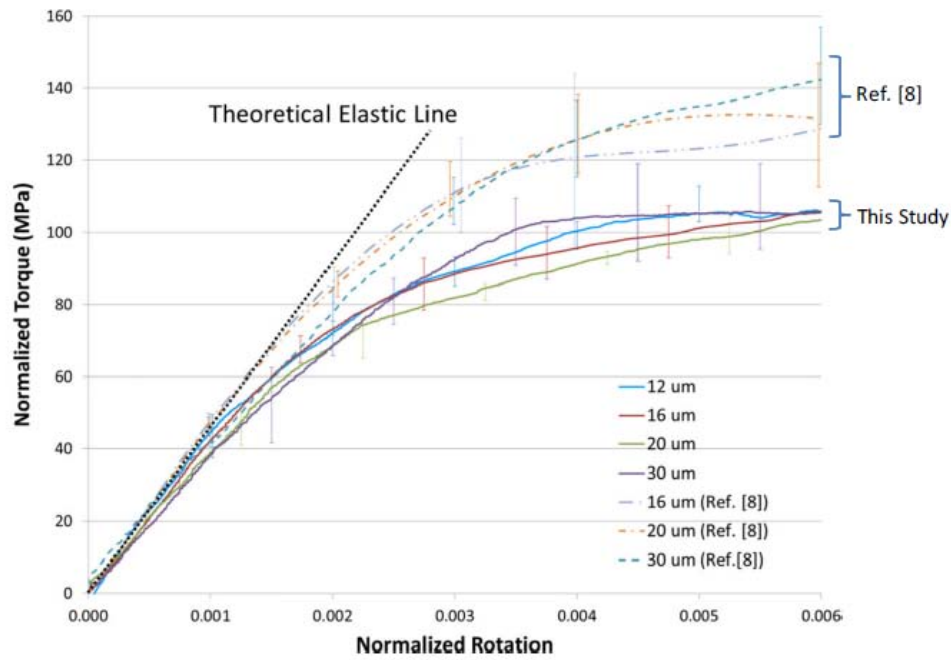


Figure 1.10 Normalized torque rotation curves of copper wires with different diameters, where normalized torque and rotation are used for comparing the deformation behaviour of specimens with various sizes (Reproduced from Lu and Song, 2015)

Walter and Kraft [12] designed an AFM-based torsion balance experiment using AFM cantilevers as load cells, contacting a cross beam attached to the wire under test, see Figure 1.11. Wire diameters ranged from 10 – 60 μm and the equipment allowed a gauge length of 58 mm. The strain was provided by a computer-controlled rotation table, so that they could investigate different strain rates. As well as monotonic torsion tests, the instrument was also suitable for cyclic tests going between forward and reverse strain. A typical cyclic result is shown in Figure 1.12, for a 40 μm gold wire. For this wire, the torque at yield is about 0.5 μNm , rising to about 1 μNm at strains $\sim \pm 0.15$. The cyclic tests showed strong Bauschinger effects, both the normal Bauschinger effect of a reduced yield strength in reverse loading, and the anomalous Bauschinger effect of plastic recovery during the unloading parts of both forward and reverse cycles. Cyclic hardening was very clearly observed.

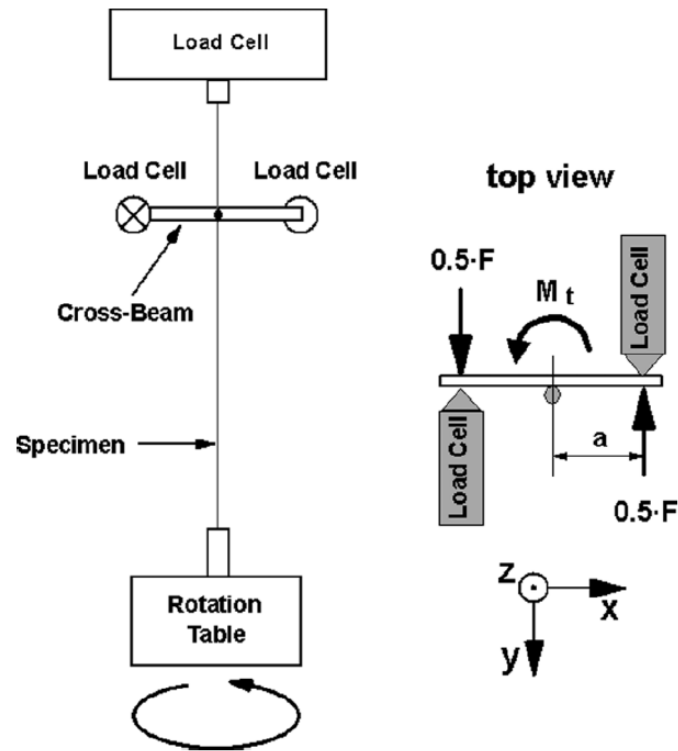


Figure 1.11 Schematic of Walter and Kraft torsion measuring principle (Reproduced from Walter and Kraft, 2011)

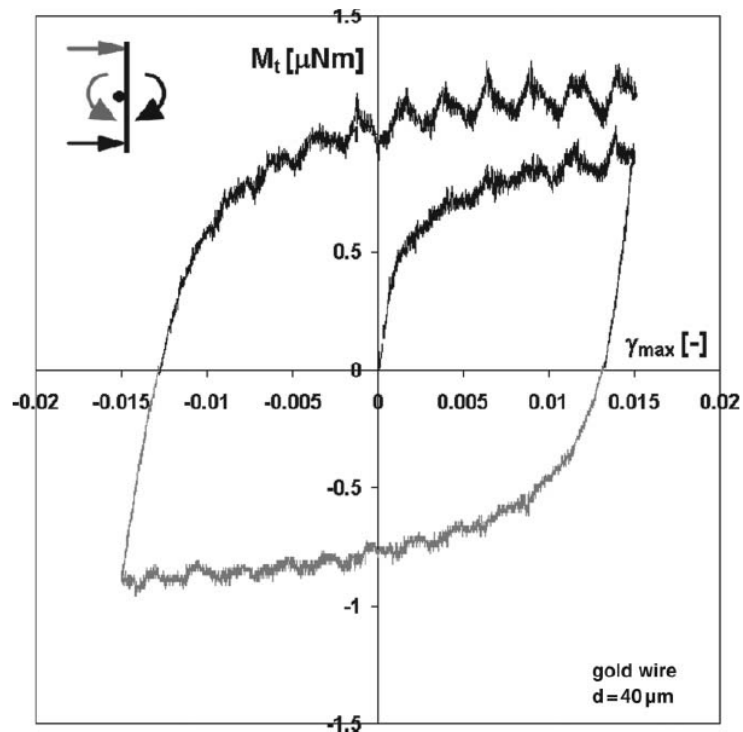


Figure 1.12 Cyclic torsion response of $40 \mu\text{m}$ diameter gold wire, where M_t is the torsion moment and γ is the surface strain (Reproduced from Walter and Kraft, 2011).

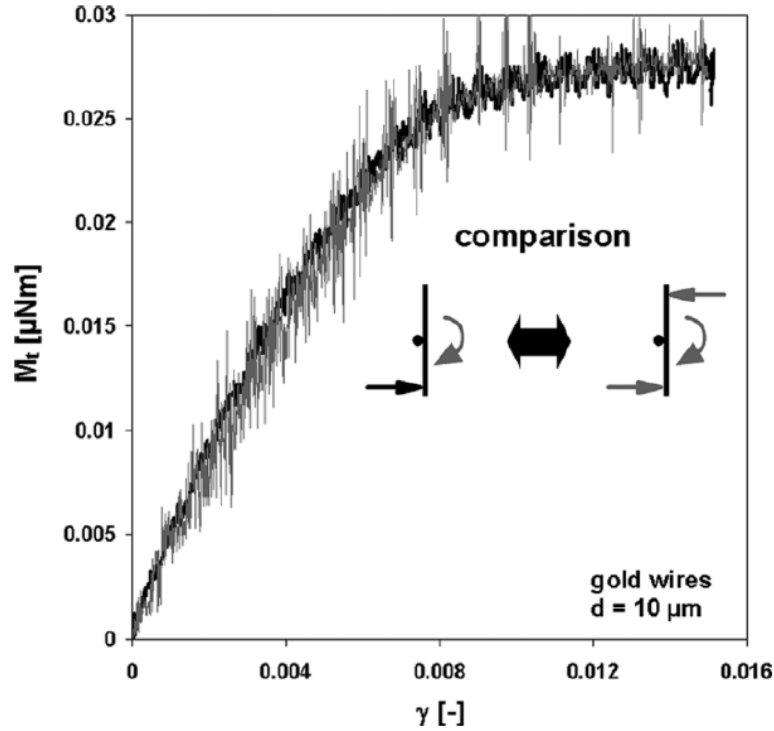


Figure 1.13 Monotonic torsion response of 10 μm diameter gold wire with one or two sensors, where M_t is the torsion moment (Reproduced from Walter and Kraft, 2011).

As may be seen in Figure 1.13, the noise in these experiments is predominantly in the torque measurement, with periodic fluctuations attributed to misalignment of the AFM tips on the crossbar, and random noise of about $\pm 0.01 \mu\text{Nm}$. On the 10 μm wire, the elastic regime extended to about 0.02 μNm , with noise of $\pm 0.0025 \mu\text{Nm}$. This corresponds to a sensitivity such that plastic strain deviations from the elastic line greater than about 10^{-4} could be detected.

Chen *et al.* [13] recently followed the Walter and Kraft experimental design. They did their work with both torsion and tension tests on gold wires, diameter ranged from 12.5 - 60 μm and averaged grain size ranged from 2.96 – 8.63 μm . An obvious sample size effect and strong work hardening were found in their study, see Figure 1.14. They were trying to demonstrate that the size effect was not only related to the grain size, sample size might also contribute, see Figure 1.15. But the problems of alignment and surface roughness might still

be a big issue in their design.

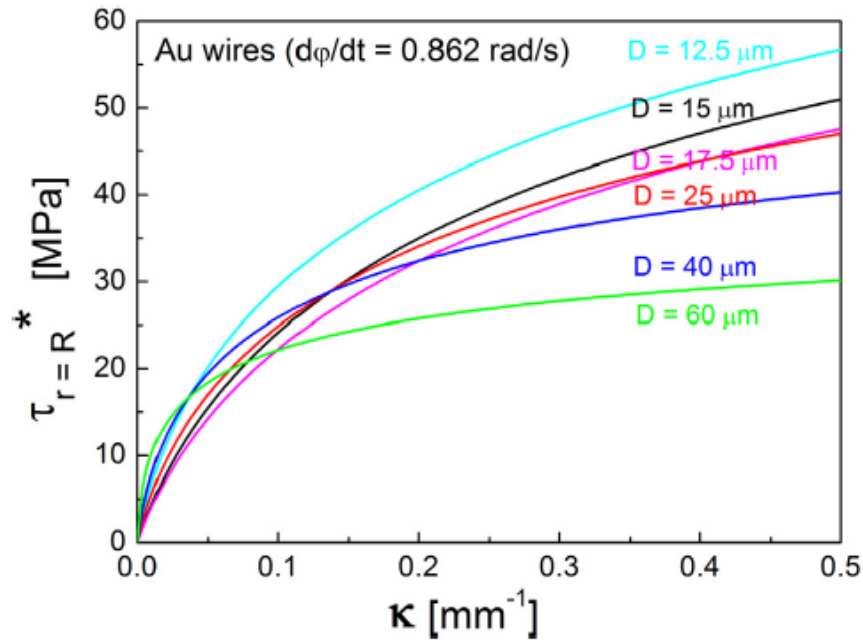


Figure 1.14 Torsional response of the wires against gradient, where D is the wire diameter, κ is the strain gradient and τ is the shear stress (Reproduced from Chen et al., 2015).

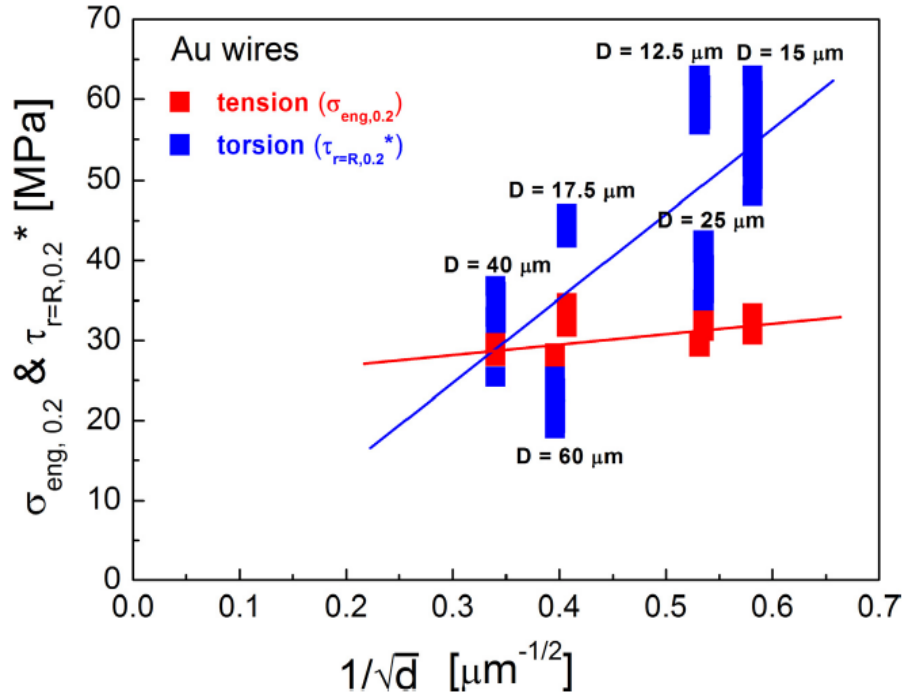


Figure 1.15 Hall-Petch behaviour of the wires with respect to the 0.2% proof stress in both tension and torsion, where D is the wire diameter (Reproduced from Chen et al., 2015).

Liu et al. [14] applied the torsion balance principle to build their automated torsion device,

see Figure 1.16. Twist angle of the torsion wire was measured by a laser sensor paired with a laser target. There are significant size effects at yielding and plastic flow in torsion in Figure 1.17, while only a minor size effect present in tension.

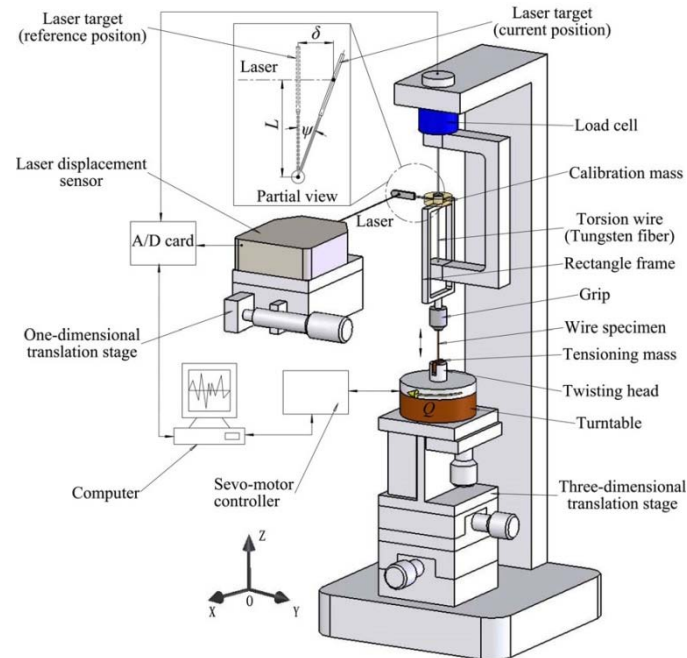


Figure 1.16 Schematic illustration of Liu torsion test apparatus (Reproduced from Liu et al., 2013).

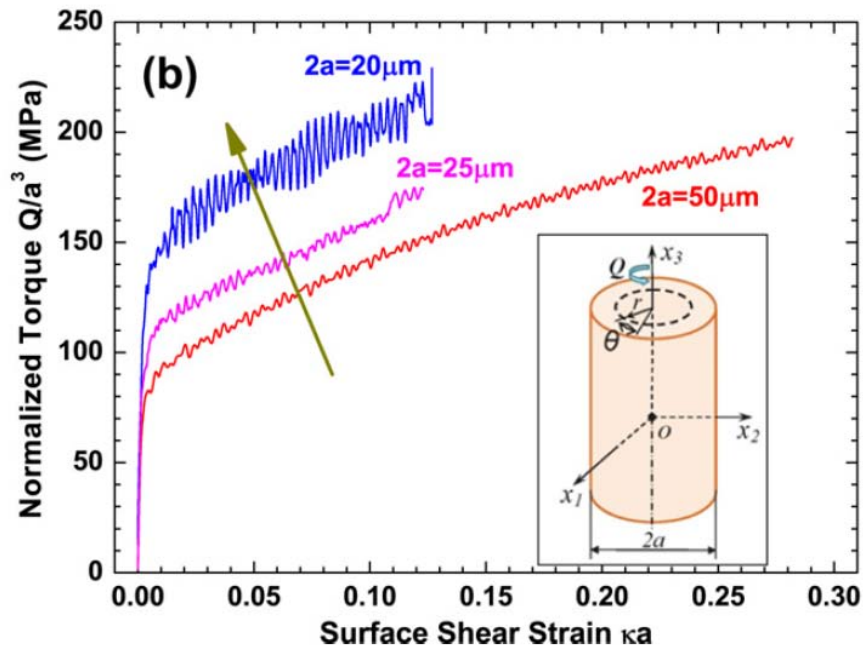


Figure 1.17 Torsional responses of copper wires with diameters from 20 to 50 μm (Reproduced from Liu et al., 2013).

Their analysis shows approximately agreement on initial yield size effect with various Strain Gradient Plasticity models and with the Critical Thickness Theory model, by choosing various parameters suitable, see Figure 1.18 and section 1.3.1. However, they did not take account of grain size effect (Hall-Petch effect) here.

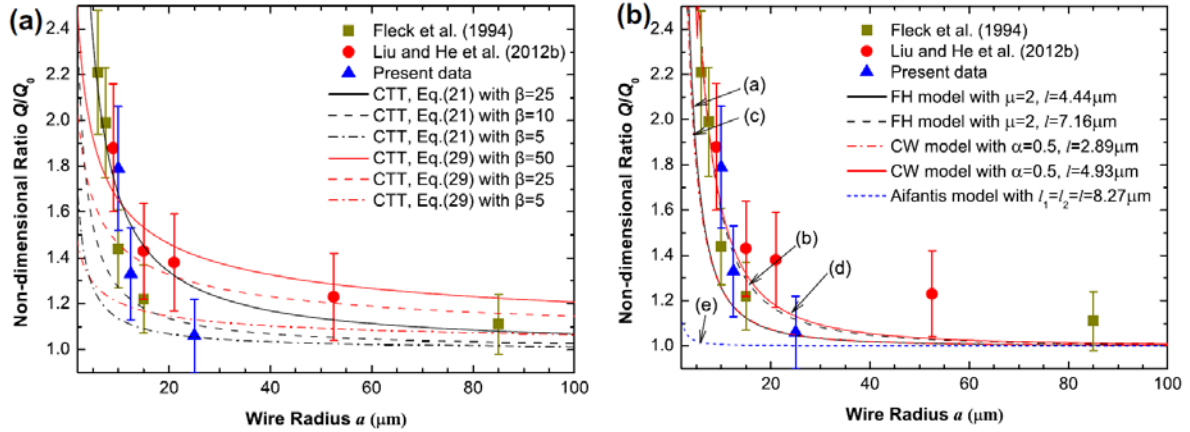


Figure 1.18 Comparisons of experimental data at yield point for copper wires in torsion and the various theoretical curves (Reproduced from Liu *et al.*, 2013)

Three successive load-unload torsion cycles were also shown in Liu *et al.*[15], see Figure 1.19. A significant Bauschinger effect was demonstrated by the yield strength in backward loading being lower than in forward loading. And on the transition from elastic to plastic, they suggested that there were neither cyclic hardening nor monotonic hardening happening since Bauschinger effect was present. In other words, they considered the Bauschinger effect is just that part of plastic recovery which requires some reverse stress.

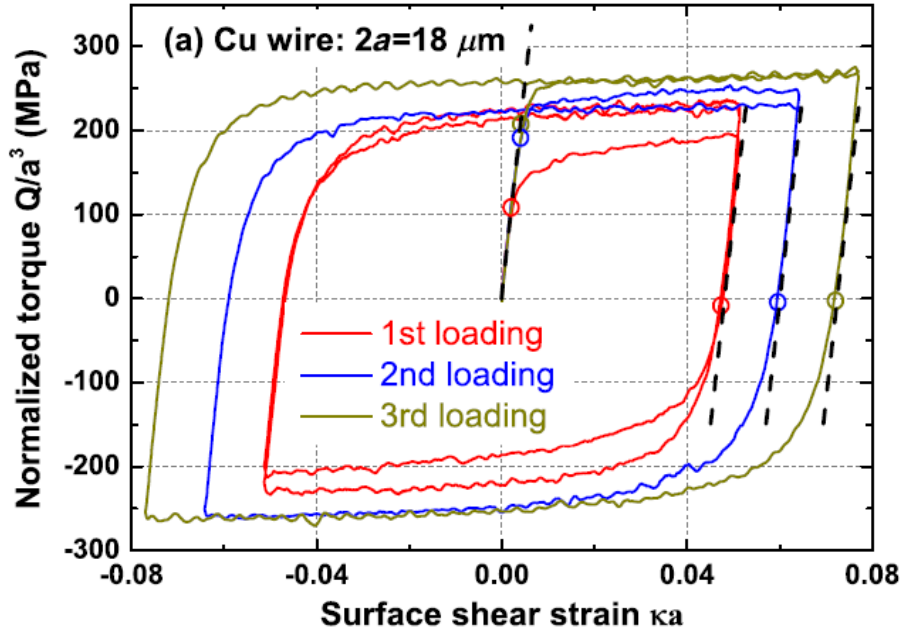


Figure 1.19 Cyclic torsion data of the Cu wires with $2a = 18, 35, \text{ and } 42 \mu\text{m}$ for the initial loading cycles, where a is the wire radius. The yield points in the forward and reverse directions are marked by circles. The wires show significant Bauschinger and size effects (Reproduced from Liu *et al.*, 2013).

Gan *et al.* [16] followed Liu to continue the torsion experiment on gold wires. They combined the Hall-Petch effect and the strain gradient effect to analyse their results, see Figure 1. 20.

In Figure 1.20, (a) (b) are for wires with the same diameter ($2a = 20$ and $50 \mu\text{m}$, respectively) but different grain sizes, displaying the increase in flow stress with the decrease in grain size. They believed the grain size played a crucial role on the strength of polycrystalline gold wires. (c) is for quasi-single crystal wires with two diameters ($2a = 20$ and $50 \mu\text{m}$). The increase in flow stress with decrease in wire diameter reveal that the strength of quasi-single crystal wires is due to the strain gradient since the Hall-Petch effect is inoperative here. Therefore they suggested that there exists an unknown relation between the Hall–Petch effect and strain gradient effect, which strongly depends on the range of grain size.

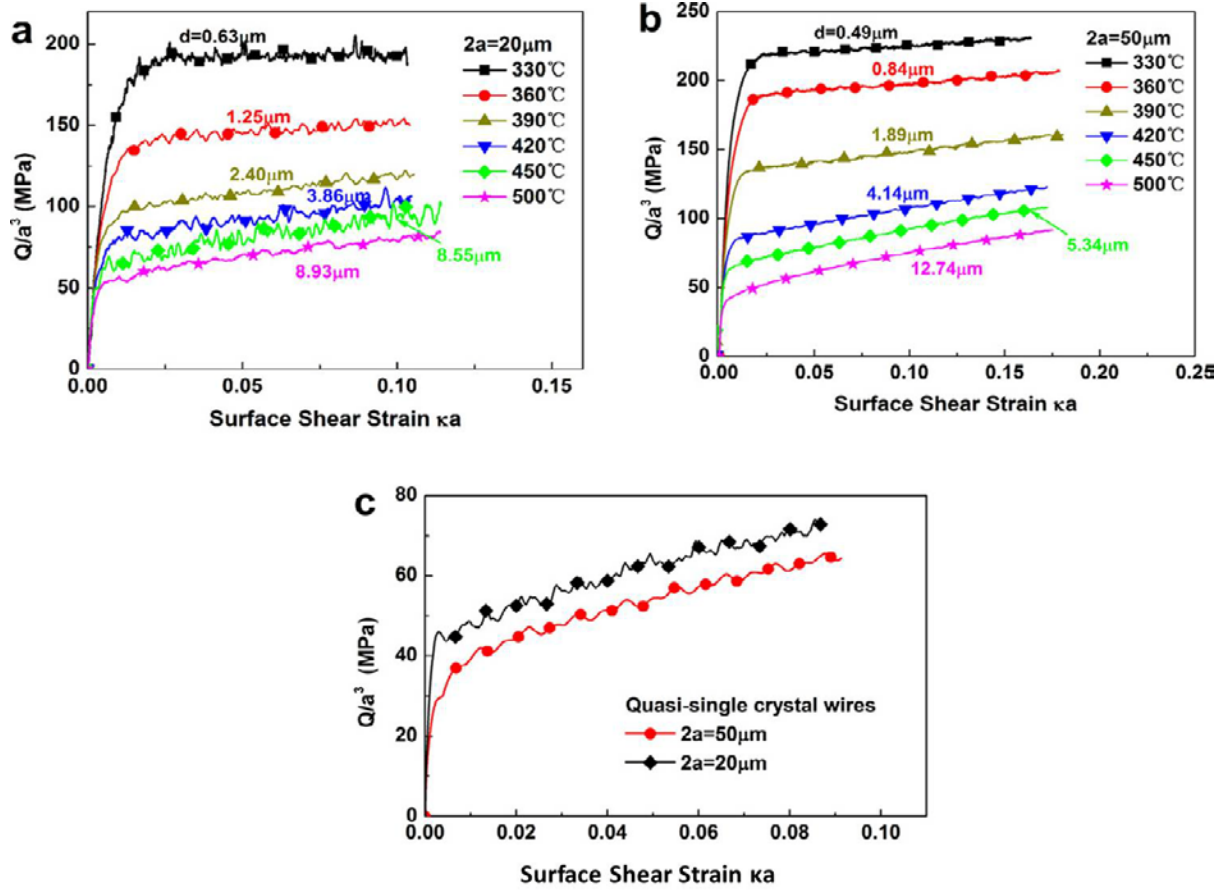


Figure 1.20 Torsional responses of gold wires at different annealing temperatures. (a) and (b) are respectively the torsional results of gold wires of diameter $2a = 20$ and $50 \mu\text{m}$ annealed in the temperature range $330 - 750^\circ\text{C}$. (c) Torsional response of quasi-single crystal wires of diameter $2a = 20$ and $50 \mu\text{m}$, where Q is the torque (Reproduced from Gan *et al.*, 2014)

The first load-unload torsion experiment was reported by Dunstan *et al.* [17]. A $10 \mu\text{m}$ diameter copper wire was compared with $50 \mu\text{m}$ wires with two different grain sizes. They fitted to the critical thickness theory describing the strain which allows dislocation sources to operate. It fitted well at large strain, see Figure 1.21.

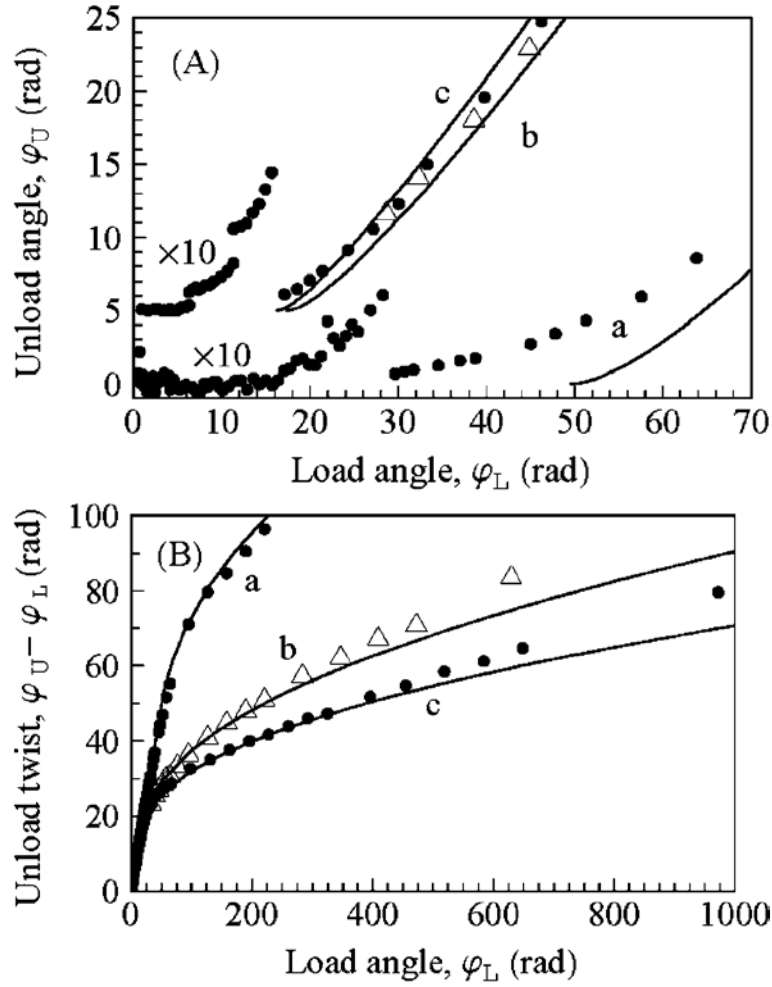


Figure 1.21 Load-unload data in torsion for three wires, (a) a 10 μm diameter wire with an average grain size of $d = 11 \mu\text{m}$ and length 0.26 m, (b) a 50 μm diameter wire with an average grain size of $d = 8.4 \mu\text{m}$ and length 1 m (open triangles), and (c) a 50 μm diameter wire with an average grain size of $d = 21 \mu\text{m}$ and length 1 m. The solid curves are critical thickness theory fitting (Reproduced from Dunstan et al. 2009).

In summary, the papers above show clear and accurate data for high strain behaviour, which reveal size effects in flow stress, initial yielding, strain hardening and Bauschinger effects. But all of them say nothing on low strain and could not determine a real yield point yet.

1.3 Theoretical principles

Micromechanical research on size dependence has been investigated over several decades since the tremendous development of small scale materials and structures. The classical

continuum plastic theory could not account for these phenomenal behaviours because there is no length scale. Many theories based on various mechanisms have been developed to overcome this deficiency.

Therefore more systematic size effects tests are still needed to reveal the physical facts.

Here we review some well-known theories.

1.3.1 Theory on inhomogeneous deformation

1.3.1.1 Strain gradient plasticity theory

In general, dislocations are generated, moved and stored when a crystal is deformed plastically. The material becomes stronger due to the dislocations' storage. There are two approaches for the dislocations' accumulation: they are collected by trapping each other in a random way or they are required for compatible deformation of various parts of the material. The first were called statistically stored dislocations (SSDs) and occur under homogeneous strain [18] while the latter ones were called geometrically necessary dislocations (GNDs), which are related to the curvature of the crystal lattice or to strain gradients [19]. The total hardening effect of a material should be a combined result of both the strain hardening (SSDs) and strain gradient hardening (GNDs).

Fleck *et al.* [1] first applied the strain gradient plasticity theory (SGP) to interpret the size effects in their torsion test. Comparing with their uniaxial tensile data, they attributed this observation to both strain and strain gradient.

Nix and Gao [20] followed this idea to create their mechanism based strain gradient plasticity theory. They assumed the indentation is accommodated by circular loops of GNDs. The GNDs are introduced by strain gradients, as shown in Figure 1.22. The SSDs were not shown in the figure.

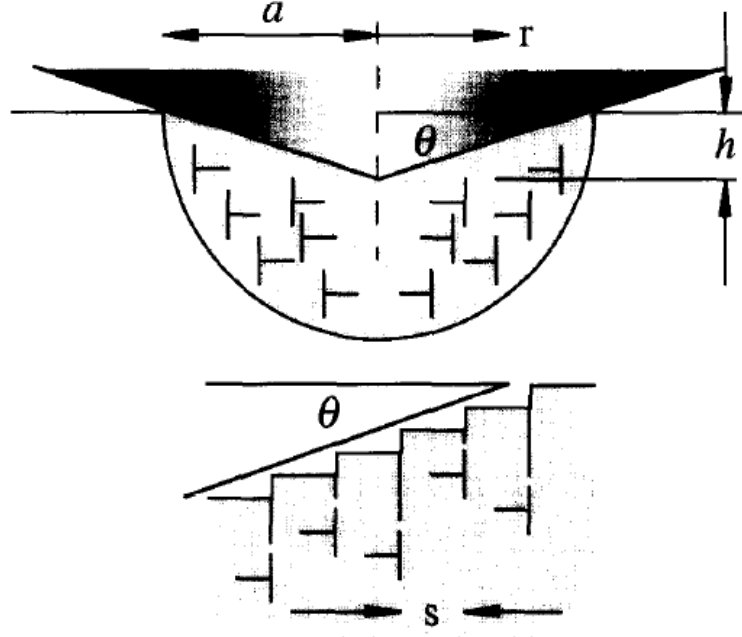


Figure 1.22 Geometrically-necessary dislocations created by a rigid conical indenter. The dislocation structure is idealized as circular dislocation loops, where θ is the angle between the surface of the indenter and the plane of the surface, a is the contact radius and h is the depth of indentation (Reproduced from Nix & Gao, 1998).

Therefore the density of GNDs is

$$\rho_G = \frac{3}{2bh} \tan^2 \theta \quad \text{Equation 1.1}$$

Here b is the Burgers vector, h the depth of indentation, and θ the angle between the plane of the surface and the surface of the conical indenter. To estimate the deformation resistance, with Taylor relation [21], shear strength follows:

$$\tau = \alpha \mu b \sqrt{\rho_T} = \alpha \mu b \sqrt{\rho_G + \rho_S} \quad \text{Equation 1.2}$$

Where ρ_T is the total dislocation density, α is a constant, μ is shear modulus, ρ_G is the density of GNDs and ρ_S is the density of SSDs. Applying the von Mises flow rules and Tabor's factor, they transformed the shear stress to hardness

$$\frac{H}{H_0} = \sqrt{1 + \frac{\rho_G}{\rho_S}} = \sqrt{1 + \frac{h^*}{h}} \quad \text{Equation 1.3}$$

Where H_0 is hardness from the SSDs alone and h^* is called the characteristic length.

$$h^* = \frac{81}{2} b \alpha^2 \tan^2 \theta \left(\frac{\mu}{H_0} \right)^2 \quad \text{Equation 1.4}$$

However, this theory could not account for the size effects in homogenous deformation. For example, Uchic *et al.* [4] observed strong size effects on micron sized pillar compression tests, see section 1.1. There is not any strain gradient therefore strain gradient plasticity did not apply. What's more, the size effects at the initiation of the plasticity cannot be interpreted by Nix-Gao strain gradient plasticity theory.

1.3.1.2 Critical thickness theory

The concept of critical thickness was first introduced by Frank and van der Merwe [22]. It is used for epitaxial layers of metals grown on nearly perfect substrates, and in the semiconductor field [23]. The elastic strain energy scales linearly to the film thickness, whereas the energy to cause relaxation has a non-zero lower limit and a weaker dependence on thickness, see Figure 1.23. The critical thickness is the thickness at which the fully strained layer become unstable or metastable. Below the critical thickness, the layer grows with an elastic strain determined by the misfit while above the critical thickness, misfit dislocations will form to reduce the strain by plastic relaxation.

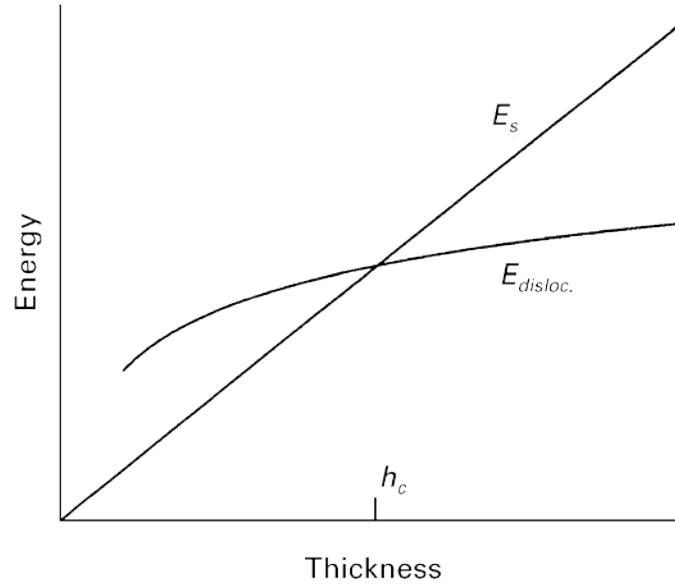


Figure 1.23 The elastic strain energy E_s increases in proportion to the strained layer thickness, but the energy of a misfit dislocation E_{disloc} rises more slowly. Critical thickness h_c is defined by the crossing of these two lines (Reproduced from Dunstan, 1996).

The underlying idea is that generation of the dislocation is a cooperative process involving numerous atoms in the crystal. This process necessarily involves a finite volume rather than beginning at a point. This geometrically required small deformation area restricts the dislocation sources and hence a higher yield stress is required. Matthews [24] applied the thermodynamic criterion to calculate the critical thickness. The assumption is that a misfit dislocation will exist if and only if the total energy of the system is reduced by its presence. Therefore the critical strain and critical thickness is

$$\varepsilon_c \approx \frac{b}{h_c} \quad \text{Equation 1.5}$$

But dislocation multiplication and significant relaxation only happens at five times Matthew's critical thickness [25, 26], where dislocation sources operate within the layer.

$$\varepsilon_c \approx \frac{5b}{h_c} \quad \text{Equation 1.6}$$

On micromechanical tests, the elastic strains are much smaller. Therefore the bulk yield strain ε_Y is also needed. The above equations were changed to

$$\varepsilon_c \approx \frac{b}{h_c} + \varepsilon_Y \quad \text{Equation 1.7}$$

$$\varepsilon_c \approx \frac{5b}{h_c} + \varepsilon_Y \quad \text{Equation 1.8}$$

This concept has been applied to the thin wire torsion [17].

When the energy of the wire with and without the dislocation is equal, the critical twist per unit length for this dislocation is:

$$K_c \approx \frac{b}{2\pi a^2} \ln \frac{a}{b} \approx \frac{5b}{2\pi} \quad \text{Equation 1.9}$$

where a is some micrometers and b some angstroms. The plastic strain generated by source operation in finite volume using $4b$ [27] for spiral source or $5b$ [17] for Frank-Read source to replace the b . According to the Figure 1.18 and Figure 1.21, critical thickness theory fitted the initial yield very well.

Spary *et al.* also used this model to explain the indentation size effect under spherical indenters by assuming that the yield stress is inversely proportional to a volume [28].

However, more work still needs to be done to fully explain the size effects by critical thickness theory.

1.3.2 Theory of homogeneous deformation

Pillar compression experiments have attracted extensive interest since the development of focused ion beam (FIB) machining. The pillars are not constrained by a substrate, so misfit dislocation mechanisms do not exist. Also the strain gradient plasticity theory could not account for these size effects since there is no strain gradient. Several alternative models were made to interpret the size effects here. Three commonly used mechanisms are dislocation starvation, dislocation nucleation and dislocation pile-up.

1.3.2.1 Dislocation starvation

Greer and Nix established the dislocation starvation mechanism to account for the size effect in their pillar compression [29]. When sizes were decreased below some critical diameter, flow stresses at 10% strain varied inversely with the diameter over a large range, see Figure 1.24.

In ordinary plasticity, dislocation movement leads to dislocation multiplication by cross-slip. However, dislocations can only travel a short distance before annihilating at the free surface especially in the small scales pillars. This will reduce the dislocation multiplication rate and eventually leads to dislocation starvation. Therefore, very high stress would be required for continual dislocation nucleation.

However, this model is far from complete due to the lack of a mathematical basis. And the initial dislocation densities are still in doubt.

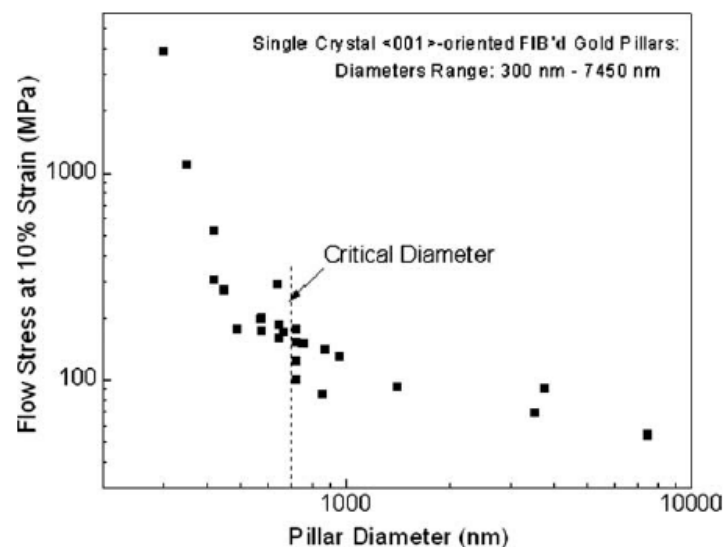


Figure 1.24 Flow stress at 10% strain vs. pillar diameter plotted on log-log scale (Reproduced from Greer et al.2005).

1.3.2.2 Dislocation multiplication

Dislocation sources are required to generate the dislocation for the plastic slip. If the number of dislocation sources is limited by sample volume, a higher flow stress is needed. Von

Blanckenhagen *et al.* [30] showed that the critical stress to bow out a dislocation segment for a given source size is given by

$$\tau_{source} = \frac{\mu b}{2\pi} \cdot \frac{1}{s} \cdot \ln\left(\frac{as}{b}\right) \quad \text{Equation 1.10}$$

where μ is the shear modulus, b is the Burgers vector, s is the source size and a is a constant. This model predicts an inverse scaling of the flow stress with the sample sizes. It is actually the same as the dislocation source operation model [31] and critical thickness theory [32].

1.3.2.3 Dislocation pile-up

Obstacles like interfaces could cause dislocation pile-ups. Kiener *et al.* [33] believed the damage during sample preparation by FIB should not be ignored. The damaged surface by Ga^+ ion bombardment could block the dislocation movement and cause pile-ups at the surface. If the deformed volume is large, there would be plenty of dislocation sources and the emitted dislocations would be uniformly distributed all over the sample. However, only a few dislocation sources are available when the sample sizes are reduced to small values. The back stress could make the activation of dislocation sources with even more difficulties. Therefore a higher stress is needed to activate other sources or to break the interface. This mechanism was first proposed by Eshelby *et al* [34] and is commonly used to explain the Hall-Petch effect.

1.4 Summary

It is clear that size effects are observed in various geometries of mechanical experiments. And torsion is the most sensitive method to detect the size effects. Different theories and models are also reviewed here as a support for their test results. However, all these models suffer from a lack of enough experiment proof.

The differences between theories and experimental data are:

1. There is not any experimental data that describes the low strain behaviour in micro torsion.
2. There is no account of the effects of grain size vs. wire size.

More work is needed to be done to reveal the underlying physical nature.

2. Experiment and Method

2.0 Introduction

Most of the torsional tests in the literature were focused on the torque-torsion method with small size samples. However their experimental resolution was not precise enough. Following the load-unload method introduced by Stölken and Evans [2], Dunstan first applied this principle to thin-wire torsion experiments [17]. The sensitivity was hugely improved by increasing the gauge length of the testing wire. However, handling and preparing the wires require involved procedures.

Smooth thin copper wires with various grain sizes are needed for our torsion experiments. Therefore we need to anneal the copper wire in a Rapid thermal annealing (RTA) furnace to grow the grain sizes. High-temperature short-time anneals (up to 1000 °C, 10 - 300s) are preferred in order to minimise surface roughening, on the grounds that the thermal activation energy for surface diffusion leading to roughening is lower than the thermal activation energy for bulk diffusion leading to grain growth and dislocation annealing [9]. The dislocation densities are reduced by this annealing, which is done in vacuum between graphite strips to avoid oxidation.

A crossbar is attached at the bottom of the wire (see Figure 2. 1). The crossbar is used to give a 2 ~ 3 MPa tension stress, which is well below the expected yield strength of the wire but high enough to avoid the symmetry-breaking “twisted hairpin” phenomenon at high strain [9]. This requires about 400 - 600 mg for a 50 μm wire, 100 - 150 mg for 25 μm wire, 64 - 96 mg for 20 μm wire and 52 - 78 mg for 18 μm wire. A thicker wire, e.g. 400 μm diameter copper wire, with appropriate mass is a suitable candidate for making the crossbar.

2.1 Sample preparation

Specimens are prepared from thin copper wires from Goodfellows purity 99.99%, Comax purity 99.99% and Youkwire purity 99.99%. The free end of wire is gently released from the manufacturer's reels. Wires are unreeled to some lengths according to their diameters with a little extra length, for example actual 1.1 m length for a 1 m length 50 μm diameter sample. The excess length is needed for both ends of the wire to be fixed on the apparatus. Then the wire is cut carefully with a scalpel and wound onto a stainless-steel bobbin for annealing.

Calibration of the RTA is needed before the annealing. A small ball of pure silver is flattened using pliers. Then it is put into a hole in the centre of a graphite strip, which is on top of another graphite strip. A third graphite strip covers the strip with the hole. Two blocks are placed on top at both ends with screws to fix these strips. Then the furnace is purged with nitrogen and vacuum of 10^{-3} Pa achieved with a vacuum pump.

Heating to 960.5 $^{\circ}\text{C}$ (just below silver's melting point of 961.8 $^{\circ}\text{C}$) for 15s takes place. If the silver melts, the RTA is not calibrated correctly. The sapphire rod of an optical pyrometer measures wavelengths of light emitted by the glowing graphite strip as they heat the sample using resistance (ohmic) heating. It needs to be cleaned using acetone on cotton buds when necessary.

The reel is then placed by tweezers in the centre hole of the graphite strip, which would be heated uniformly, between two graphite strips (no hole in the centre). Closing the lid, the furnace was purged twice with nitrogen and pumped out. Then the annealing took place in a vacuum ambient, pressure less than 0.1 mbar. The required annealing time and temperature are controlled.

Unwinding the wires from the reels on which they are annealed while hanging them in the top of the apparatus (see Figure 2.1) introduces some plastic deformation. A further *in situ* anneal is needed to anneal any strain-hardening occurring in unspooling the wire and enable the

small tensile stress to straighten the wire. This is done *in situ* by direct electrical heating in a nitrogen ambient. The temperature is monitored by the thermal expansion and the increase in resistivity. For a 1 m gauge length of copper wire, 7mm expansion corresponds to 300 °C. For 10 μm diameter copper wire, a 1 m length has a resistance of about 220 Ω at room temperature and this rises to 550 Ω at 400 °C. For larger diameters, the resistance is lower, but the increase in resistance at high temperature is proportionate. Typical currents are 180 mA for 10 μm diameter copper wire and 800 mA for 50 μm diameter copper wire [9]. These procedures are designed to minimise residual stress and ensure reproducibility in testing conditions. In particular, the surface roughness and oxide film are not significantly worsened.

2.2 Experiment apparatus

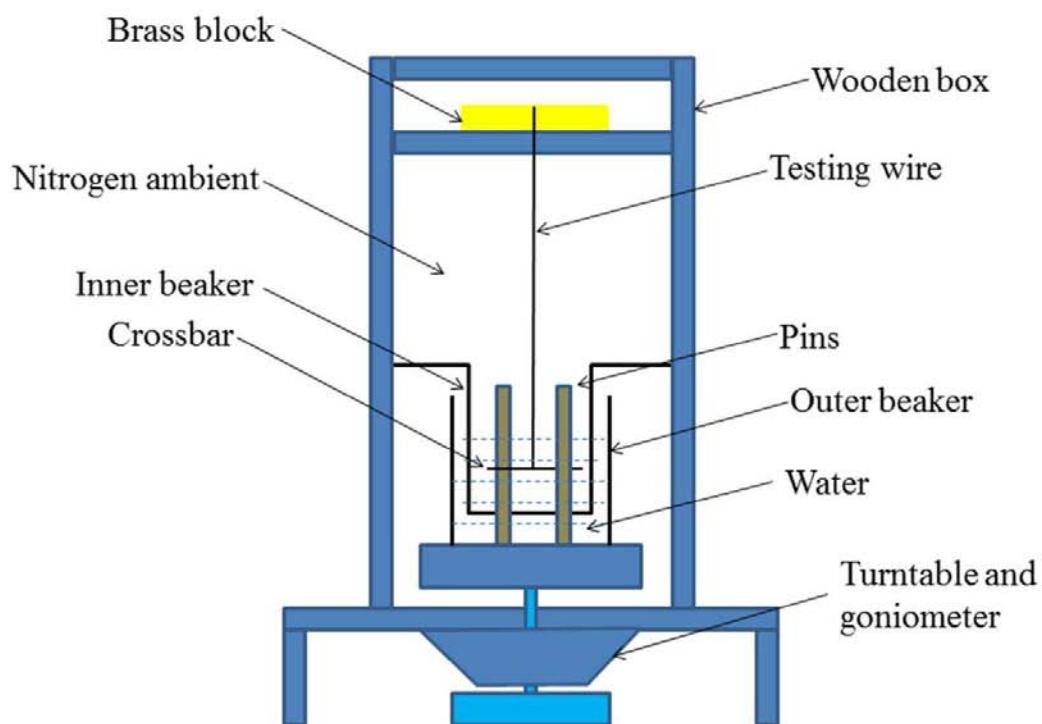


Figure 2.1 Schematic representation of the apparatus for torsion testing

The apparatus is shown schematically in Figure 2.1. On removal of the spool from the RTA furnace, the crossbar is fitted a few cm from the end of the wire. It is laid along the median line of a small square of 1 cm² copper foil, which is then folded over it. Both silver paint and

super glue was applied to the copper foil to fix the wire. Soldering with tin was also used for enhancing the electrical connection between the crossbar and the testing wire, especially for use in an electrolyte solution. Typically the foil and the glue add less than 5 mg to the weight of the assembly. The total tensile stress is still far smaller than the yield stress.

The reel is then mounted at the top of the wooden enclosure and the wire is lowered until the crossbar hangs between two drive pins. The wire is glued with the electrically conducting silver paint at the top to the brass block. Electrical connections are made to the brass block and the enclosure is filled with nitrogen to reduce oxidation of the copper wire. The crossbar is immersed in water. The pair of drive pins engages the crossbar to twist the wire to some angle. Electrical contact is made by adding sodium carbonate to the water to make it a current-carrying electrolyte and using a graphite anode. The *in situ* anneal is carried out by passing a current to heat the wire to 300 - 400 °C. The pair of concentric beakers are located above the centre of the turntable and goniometer.

2.3 Method and principle

The turntable is rotated to engage the pins with the crossbar, and then advanced to successively higher angles ϕ_L to load the wire. After each load angle it is backed off to unload the wire completely, and the angle at which the crossbar is free of the pins is the unload angle ϕ_U . These angles when multiplied by a/L where a is the radius of the wire and L is the gauge length, are the total torsion (the surface shear strain ε_S under load) and the plastic torsion (the unloaded surface shear strain ε_{pl} , a measure of the plasticity throughout the wire). When $\phi_U = 0$ the deformation is entirely elastic, see Figure 2.2.

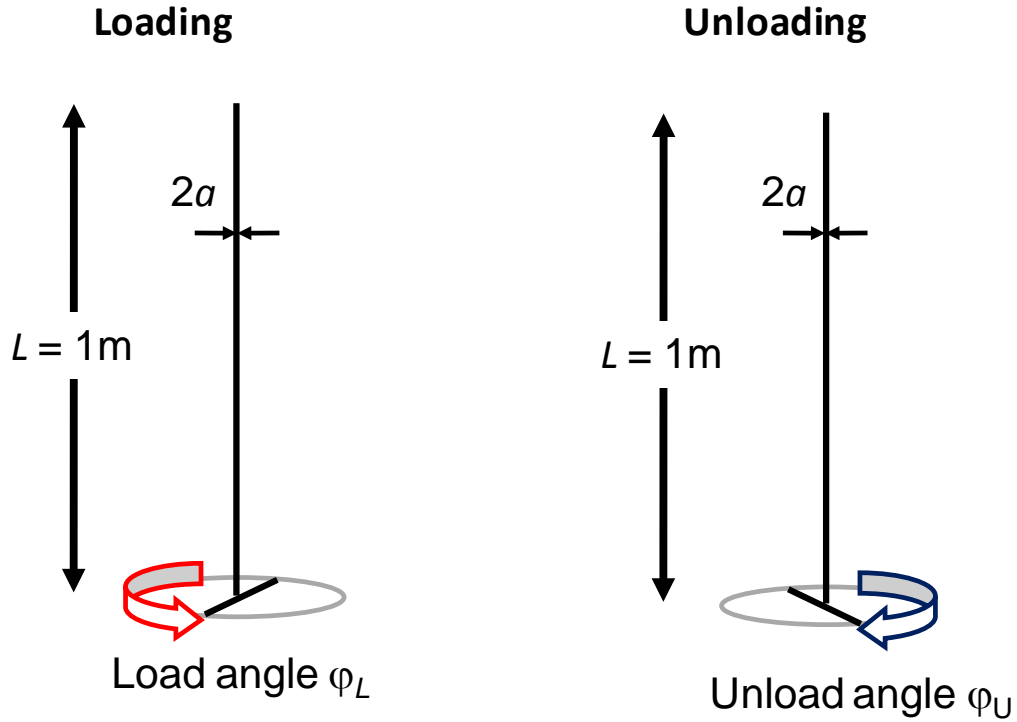


Figure 2.2 Loading-unload principle in wire torsion

Stresses can be deduced from the elastic recovery on unloading while plastic strain is identified with the unrecovered deformation. Simple definitions of instantaneous plasticity, creep and Bauschinger effects are not straightforward to apply in these experiments and particularly at very low strains. We consider together the experimental method and what it is that is really measured in these experiments.

For a wire under torsion, of radius a and length L , twisted through an angle ϕ , we have

$$\varepsilon_s = \phi_L \frac{a}{L} \quad \text{Equation 2.1}$$

And

$$\varepsilon_{pl} = \phi_U \frac{a}{L} \quad \text{Equation 2.2}$$

The load angle determines the total torsion ε_s , which may be expressed as the shear strain at the surface. The unload angle determines the plastic torsion ε_{pl} . Therefore the elastic strain is determined by

$$\varepsilon_{el} = \varepsilon_s - \varepsilon_{pl}$$

Equation 2.3

Figure 2.3 shows schematically what happens during the experiment. The dashed lines show schematically the ideal elastic-plastic behaviour and the solid lines show what may happen in reality. The arrows show loading to some angle ϕ_L and unloading along the elastic line, with unload angle ϕ_U indicated by the data-points on the x -axis. Cycle 1 shows ideal elastic behaviour while cycle 2 goes beyond the elastic limit, giving $\phi_U > 0$. The difference, $\phi_L - \phi_U$ gives the elastic torque correctly even if (cycle 3) there has been some plasticity or creep during the supposed elastic regime. If the wire is maintained under load for a while (cycle 4), creep occurs and can be monitored by periodic unloadings (unload path 6). However, plastic recovery during the unloading (unload path 5) cannot be detected and causes an overestimate of the torque under load by the amount indicated by the curly bracket. However, plastic recovery can be monitored as a function of time in the unload condition (unload points 7). The dotted line from A to B shows the effect of a tensile stress σ on the surface shear stress τ . The elastic line of cycle 1 corresponds to Hooke's Law in shear. The effect of a 2 MPa tensile stress is shown quantitatively with the cross at A at coordinates (0 $\mu\epsilon$, 2/3 MPa) and the cross at B at coordinates (84 $\mu\epsilon$, 4.2 MPa).

The wire is twisted to some load angle (ϕ_L) and then released. If the deformation is purely elastic the torque during loading and unloading follows the elastic line (load and unload paths 1 in Figure 2.3) and the torsion returns to the unload angle (ϕ_U) at the origin (point 1). During this cycle, the surface strain is $\varepsilon_s = \phi a/L$, where a is the radius of the wire and L is the gauge length, and the surface stress is $G\varepsilon_s$. When the wire is twisted further, into the plastic regime (cycle 2), the unload angle (point 2) gives the amount of plastic torsion $\phi_{pl} = \phi_U$ and the elastic torsion is then $\phi_{el} = \phi_L - \phi_U$. The torque Q is not measured in the load-unload method but can be deduced, as

$$Q = \frac{1}{2} \varepsilon_E G \pi a^3$$

Equation 2.4

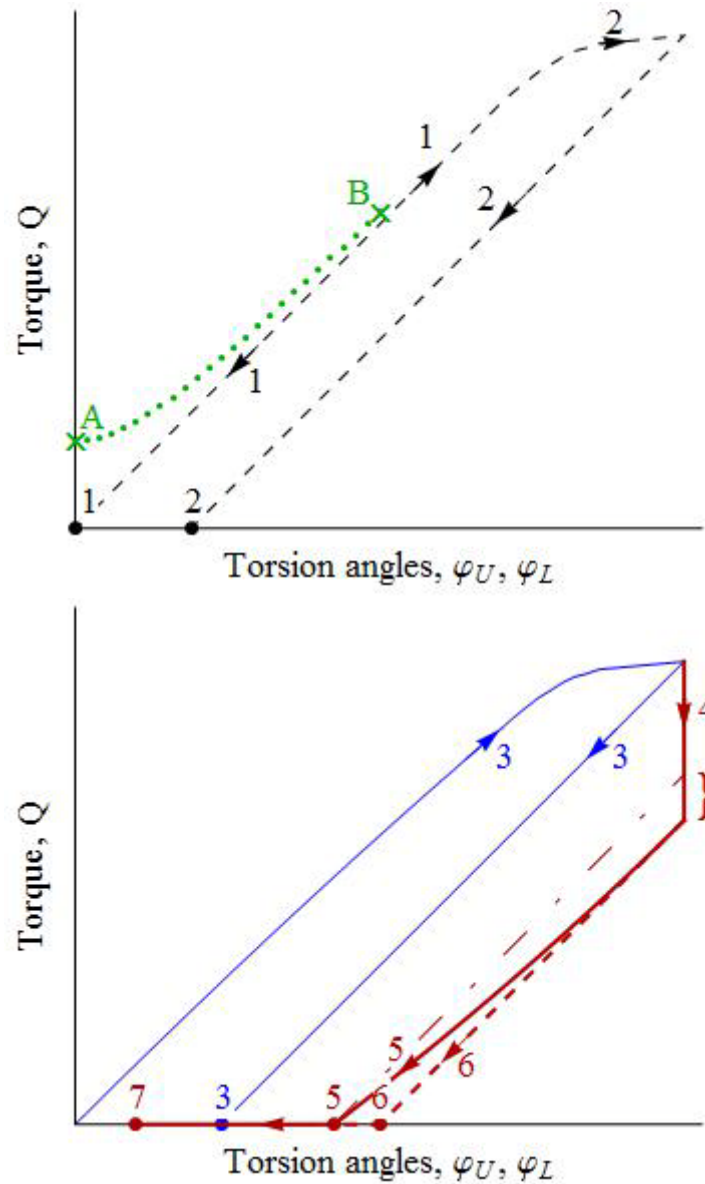


Figure 2.3 Schematic of the load-unload method for measuring the surface shear strain and its elastic and plastic strain components.

In a macroscopic experiment, plasticity initiates at the surface where the strain is highest, and a stress-strain curve can be deduced from the torque-torsion data. That is not possible here. When the wire diameter is small enough to reveal the size effect, Dunstan and Bushby [26] predicted a radial stress distribution different from the macroscopic case, with an increased stress at the surface. This was confirmed by Motz and Dunstan [35] in discrete dislocation dynamics simulations of beam bending.

Early plasticity or creep during loading may occur as shown by cycle 3 in Figure 2.3, and

results in increased values of ϕ_U . Creep may also be studied by maintaining the load angle for some time (path 4). On the other hand, plastic recovery during the unloading, as shown in the unload path 5, cannot be measured, and leads to an over-estimate of the torque under load indicated by the curly bracket. Plastic recovery after unloading, especially when assisted thermally, can easily be measured (path 7). It is well-established that plastic recovery can occur during and after unloading. It was reported by Bauschinger in 1880, and has been observed in micromechanical experiments for example by Demir and Raabe [36] and Kirchlechner *et al.* [37] in beam bending, by Liu *et al.* [15] in wire torsion, and by Kiener *et al.* [38]. in discrete dislocation dynamics simulations. It is a strong function of time and temperature. As discussed by Liu *et al.* [15], a consequence of plastic recovery on unloading is that the stress under load is overestimated in the load-unload method. However, this sort of error is not unique to the load-unload method. A load cell used to measure stress does not respond instantaneously. After the application of a given strain, creep occurring during the time required for the load cell to report means that the stress required to give the instantaneous plasticity is underestimated. However, unquestionably, the longer time between full load and measuring the unload angle in our experiments means that these errors are greater in our method.

In these experiments, we measure elastic and plastic strain, and with the limitations given above we can approximately estimate the surface shear stress under load. For copper wire, this is about 0.05 MPa per elastic microstrain. A 2 MPa tensile stress adds to the torsional shear stress as shown by the dotted line A-B in Figure 2.3; beyond about 80 $\mu\epsilon$ or 4MPa shear stress the tensile stress makes very little difference to the magnitude of the surface strain. However, and particularly at smaller radii where the shear stress is less and the 2 MPa normal stress remains more important, the relationship of the full elastic strain (stress) tensor to the individual slip systems (different in each grain) is not clear.

Macroscopically, plasticity may be considered to be permanent deformation after a load-unload cycle. Or microscopically plasticity may be defined in terms of the irreversible movement or creation of dislocations during a load-unload cycle. Both definitions have weaknesses, especially when plastic recovery on unloading is considered. The phenomena of creep under load and of plastic recovery on unloading show that the loaded state and the unloaded state can be – and generally are – metastable. Not shown in Figure 2.3 is the load reversal that we use. The same descriptions of the load-unload method apply there.

In a typical experiment leading to a plot of unload angle against load angle (see Figure 3.1), the load angle was increased in step of 5° per step in a time of a few seconds and immediately reversed to disengage the crossbar, letting the wire hang freely. The unload angle was again measured within a few seconds. During such an experiment, creep tests were carried out less frequently, generally every 60° , leaving the wire under load for successively longer periods of 2, 4, 8 and 15 minutes. Thermal annealing was carried out after each creep test for 10 seconds at successively higher temperatures of 100, 200 and 300°C . After loading the wire in one direction (forward) to some degree of plastic deformation, the direction of load was then reversed; several such cycles were carried out.

2.4 Characterization

Images of grains on the cylindrical surface of the wires were obtained by focused ion beam (FEI Quanta 3D FEG) microscopy, using the strong channelling contrast associated with the secondary electrons (see Figure 2.4). Grain sizes were estimated by the Heyn line intercept method [39], counting the number of grains along a line of specified length drawn on the image. Figure 2.5 gives a histogram of a typical size distribution. These estimates are not highly accurate but they are certainly representative.

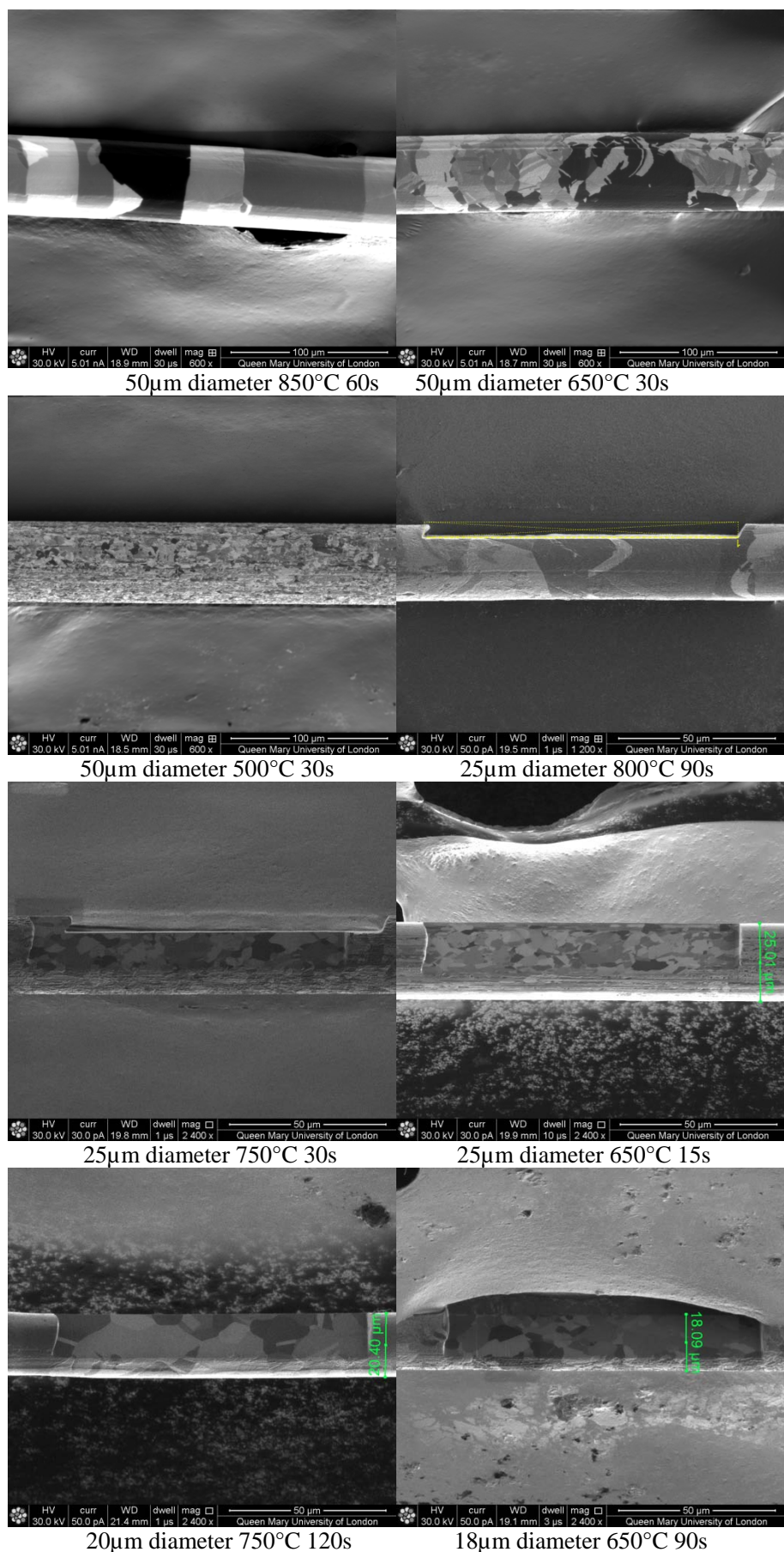


Figure 2.4 Grain size for all annealing conditions

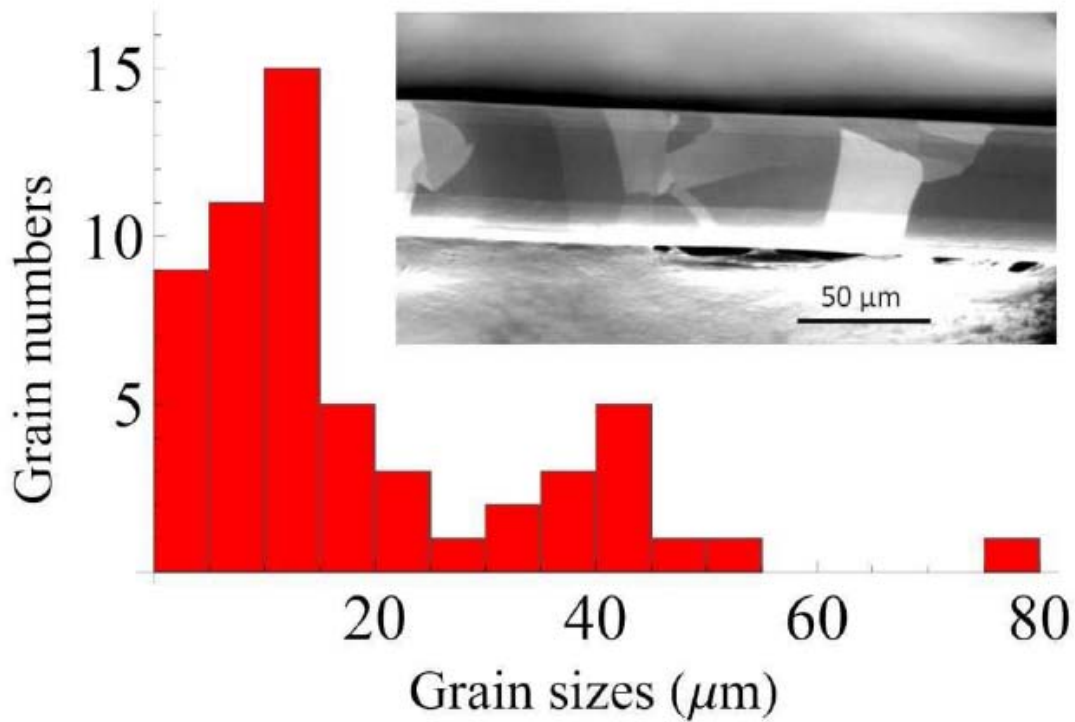


Figure 2.5 Grain distribution of the wire in Figure 3.1 over 1 mm length. Inset, FIB microscopy of the wire surface showing the grains strongly contrasted by their crystal orientation.

2.5 Twist per dislocation

Here the twist angle is ϕ , the twist (torsion) per unit length is $\kappa = \phi/L$ (L is the length of the wire), the surface strain is $\varepsilon_S = \kappa a$ (a is the wire diameter) and torsional strain is $\varepsilon(r) = \kappa r = \varepsilon_S r/a$.

Clearly, when no new dislocations are introduced and the motion of existing dislocations between metastable positions is ignored, the equilibrium position of the wire is $\phi_U = 0$. The smallest amount of plasticity that can be introduced along the whole wire consists of one single axial screw dislocation. In this case, the entire cross-section of the wire has undergone plastic deformation. On the other hand, the introduction of a dislocation near the surface will give an amount of plastic deformation less than this, and might be considered to be near-surface plasticity only. The Eshelby twist that this introduces is readily calculated and it is an

important quantity in assessing the experimental results. For a single axial screw dislocation, the shear strain field is $\varepsilon_d = b/2\pi r$ for r from r_0 to a , where b is the magnitude of the Burgers vector, r_0 (a core radius) is introduced to avoid divergence in calculations. The strain field due to torsion is $\varepsilon_k = \varepsilon_s r/a$. Adding the two strains, and integrating the resulting strain energy over the wire, we get

$$U = \frac{1}{2} G \int_{r_0}^a 2\pi r (\varepsilon_d + \varepsilon_k)^2 dr \quad \text{Equation 2.5}$$

Solving for the value of ε_s at which U is minimum, we obtain

$$\varepsilon_s = \frac{ab}{\pi(a^2 + r_0^2)} \approx \frac{b}{2a} \quad \text{Equation 2.6}$$

For the 50 μm copper wire, $a = 25 \times 10^{-6}$ m, $b \approx 0.25 \times 10^{-9}$ m, $r_0 \approx b$, giving $\varepsilon_s \approx 3 \mu\epsilon$. That is, 3 $\mu\epsilon$ of plastic strain corresponds to one new dislocation throughout the whole wire (or, of course, a larger number of dislocations in a fraction of the wire). On the other hand, to generate dislocations by the extension of existing dislocations requires a strain-thickness product from centre to surface of $\frac{1}{2} \varepsilon_s a \sim b$ [17, 26]. For the Burgers vector of copper ($b = 0.256$ nm) and the wire radius $a = 25 \mu\text{m}$, this corresponds to about 20 $\mu\epsilon$ elastic surface strain. To multiply dislocations by the operation of spiral sources requires about four times this or 80 $\mu\epsilon$ elastic surface strain [26]. Any bulk strength, e.g. due to Peierls stress, both adds directly to these values and also requires an elastic core radius r_e so that the strain-thickness product is calculated only from r_e to the surface [26].

2.6 Problem

There is one thing needed to be noticed. The crossbar did not always contact the two pins at the same time. Sometime it touched one pin first under low strain range during *in-situ* annealing. It might turn to touch two pins together in high strain (thousands micro-strain). Other time the crossbar only touched one pin during the whole test. The wires are positioned

to the centre to reduce this problem.

However, we have more interest on the changes of the load and unload angles instead of measuring accurate load and unload angles. The contacting issues did not affect the results significantly.

3. High resolution low strain torsion results

Now we present the low strain load-unload data obtained for different wire sizes.

In metallurgy, the yield point is described as where permanent or non-reversible deformation begins to occur. Below the elastic limit only elastic deformation happens and at higher stresses or strains plastic deformation occurs as well. Understanding size effects is crucial at low strain around the elastic limit, since structural failure (whether by fracture, creep or fatigue) is usually a consequence of exceeding the elastic limit [17]. However, the real elastic limit is rarely used in engineering since it is very difficult to detect. In general, different definitions of yield are used for practical purposes such as the 0.2% proof stress [40]. These engineering definitions of yield acknowledge that measurable plasticity has already occurred. Since we have one of the most sensitive torsion instruments, we might have a chance to define the real yield point, or at least explore the area that people are not familiar with.

Besides the majority of monotonic loading experiments, cyclic plasticity is also important. In practice, the failure of small-scale structures in service is usually due to cyclic loading [41]. Therefore cyclic deformation was also studied here.

The Bauschinger effect normally refers to the strength reduction on reversing strain after a forward direction deformation. It is a significant phenomenon found in most crystalline materials. Normally, all Bauschinger effects in bulk materials appear during the reverse loading. Recently, an anomalous Bauschinger effect has been observed in metallic thin films with passivation layers [42-44], in which the reverse flow already takes place on unloading.

Generally, the Bauschinger effect was attributed to a back stress [45]. On plastic deformation, dislocations would interact with barriers, such as other dislocations, grain boundaries and precipitates. These barriers would inhibit the dislocation movement. A back stress was formed spontaneously around the contact area. This back stress would hinder the further

production of the dislocations. While on reversing deformation, this back stress helped the dislocation move in the reverse direction, which means the flow stress would be lower.

3.1 Raw data presentation

To illustrate our results, Figure 3.1 shows how the raw data was obtained and displayed. The turntable was rotated to engage the pins with the crossbar initially at balance position, marked as 0° . Forward zero (generally anti-clockwise) and backward zero (clockwise, in the case of reversal loading) are marked separately. Then the load angle was increased by 10° per step (black dots) until 60° , each loading lasting about 15 seconds until the unload condition was restored. At 60° a creep test was performed by leaving the wire under load for 2, then 4, 8 and finally 15 minutes, unloading each time to determine ϕ_U . A thermal recovery test followed, in which the unloaded wire was heated to 100°C , 200°C and finally 300°C for 10 seconds at each temperature followed by a determination of ϕ_U . For larger strains, larger steps in load angle were taken, 20° per step for the next cycle and then 40° , with creep and thermal recovery tests as marked. However, load and unload angles in degrees have no generality (being dependent on the values of the wire radius (a), and the wire length (L)), so all data are presented as plastic strain as a function of total strain, as described in Chapter 2.

Up to $\varepsilon_S = 26 \mu\epsilon$ (60°), the data are extremely flat, that is, there is no change in unload angle. At the first creep test at $26 \mu\epsilon$, the unload angle changed about $0.5 \mu\epsilon$ (1°). After heating the wire, the unload angle recovered completely to the starting value. At the second creep test at $78 \mu\epsilon$ (180°), the unload angle changed $0.5 \mu\epsilon$ while the annealing recovered the unload angle beyond the original position $0.5 \mu\epsilon$. At the last creep at $183 \mu\epsilon$ (420°), the unload angle changed $3 \mu\epsilon$ while the annealing just restored the unload angle $1.5 \mu\epsilon$ (3°) (Figure 3.1 inset).

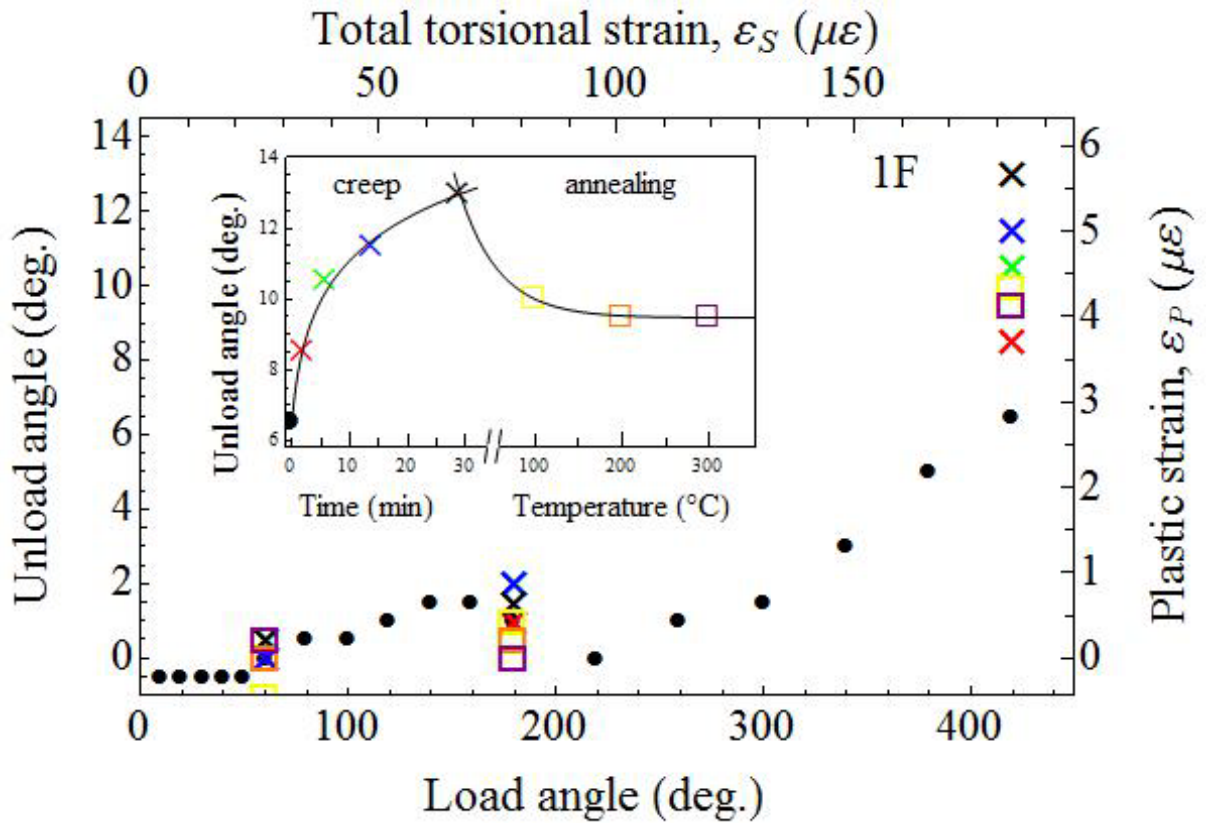


Figure 3.1 An example of the raw data from the first forward (1F) loading of a wire. The unload angle is plotted against the load angle. The dots (•) are the successive load-unload data points. Creep test data are indicated by the red, green, blue and black crosses, which represent successive loading for 2, 4, 8 and 15 minutes. Thermal-induced plastic recovery data are indicated by the yellow, orange and purple squares, which represent for successive heating to 100, 200 and 300 °C. The inset shows the data during creep and thermal recovery at a load angle of 420°.

3.2 Monotonic loading

3.2.1 Results of 50 μm diameter copper wire

Figure 3.2 shows the first forward (1F) direction load-unload data on 50 micron diameter 1 meter length copper wire with an average grain size 12 μm. Deformation was observed from the starting point while appearing to happen mainly during the creep tests. Before the first creep test at 26 μɛ total strain, the data was scattered around the x -axis, from -1 μɛ to 1.5 μɛ.

After that, the data is extremely flat until the second creep at 52 $\mu\epsilon$ total strain. Then the deformation was increased gradually. The creep at 131 $\mu\epsilon$, 157 $\mu\epsilon$ and 183 $\mu\epsilon$ total strain were partly recovered while the creep at 52 $\mu\epsilon$, 79 $\mu\epsilon$ and 105 $\mu\epsilon$ total strain were completely restored. There was a ‘step-like’ deformation around 83 $\mu\epsilon$ total strain, suddenly changed from 2.4 $\mu\epsilon$ to 3.1 $\mu\epsilon$, same as at 137 $\mu\epsilon$ and 151 $\mu\epsilon$ total strain. The scatter seems to be large at the beginning and then settle down.

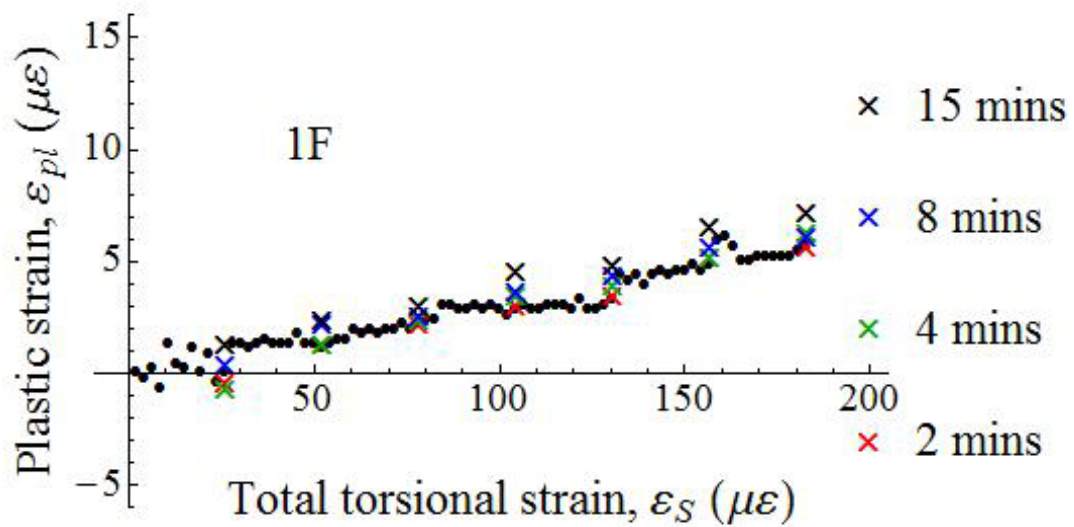


Figure 3.2 Plastic strain vs total torsional strain for a copper wire of 50 μm diameter, 1 m length, annealed at 850 $^{\circ}\text{C}$ 60s, grain size 12 μm . The black dots • are the successive load-unload data points for 1F loading. Creep test data are indicated by the red, green, blue and black crosses, which represent successive loading for 2, 4, 8 and 15 minutes.

Figure 3.3 is a second 1F direction load-unload data on 50 micron diameter 1 meter length copper wire with moderate grain size 3.3 μm . The data was quite stable around the x -axis until the creep test at 157 $\mu\epsilon$ total strain. The deformation was then increased. All three creep tests at total strain of 52 $\mu\epsilon$, 104 $\mu\epsilon$ and 157 $\mu\epsilon$ were all completely restored by waiting 15 minutes in room temperature, while the amount of the last creep was much larger than the first two creep tests.

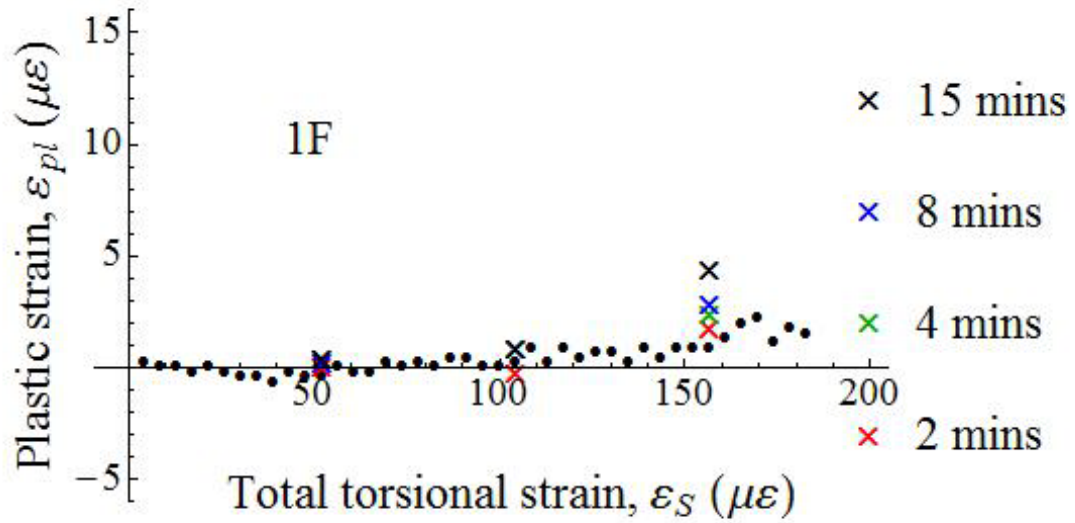


Figure 3.3 Plastic strain vs total torsional strain for a copper wire of 50 μm diameter, 1 m length, annealed at 650 $^{\circ}\text{C}$ 30s, grain size 3.3 μm . The black dots • are the successive load-unload data points for 1F loading. Creep test data are indicated by the red, green, blue and black crosses, which represent successive loading for 2, 4, 8 and 15 minutes.

Figure 3.4 shows data from a third 1F test on 50 micron diameter 1 meter length copper wire with the fine grain size of 2.6 μm . The data were extremely flat up to 78 $\mu\epsilon$ total strain. The data was also quite stable from 78 $\mu\epsilon$ to 183 $\mu\epsilon$ total strain. The creep at 78 $\mu\epsilon$ was partly recovered while the creep of the other three tests were all fully recovered. The amount of four creep was gradually increasing. There was also a ‘step-like’ change at total strain of 78 $\mu\epsilon$.

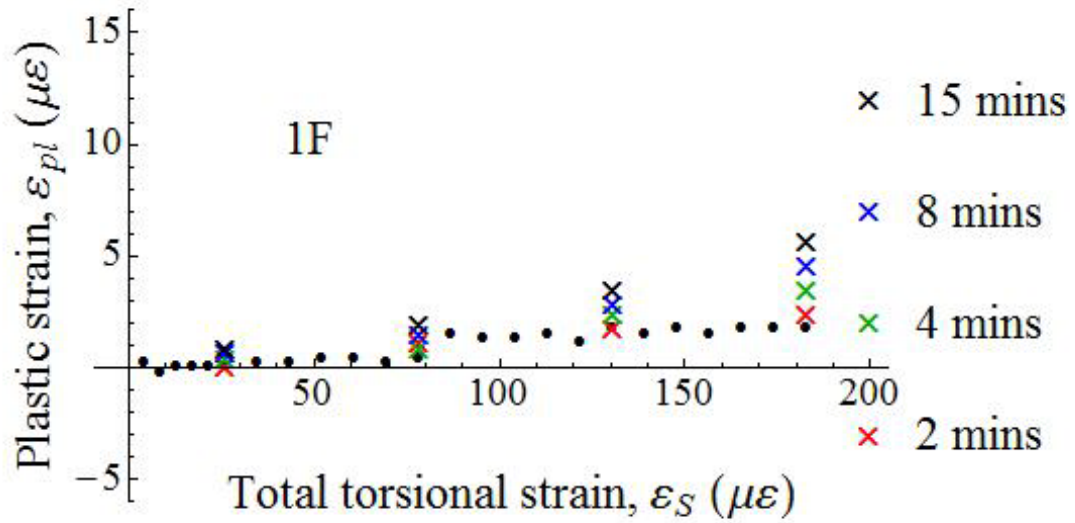


Figure 3.4 Plastic strain vs total torsional strain for a copper wire of 50 μm diameter, 1 m length, annealed at 500 $^{\circ}\text{C}$ 30s, grain size 2.6 μm . The black dots • are the successive load-unload data points for 1F loading. Creep test data are indicated by the red, green, blue and black crosses, which represent successive loading for 2, 4, 8 and 15 minutes.

3.2.2 Results of 25 μm diameter copper wire

Figure 3.5 is a first 1F direction load-unload data on 25 micron diameter 0.5 meter length copper wire with large grain size 10 μm . The data was scattered below the x -axis up to 26 $\mu\epsilon$ total strain, from -2 to 0 $\mu\epsilon$. Then the deformation was increased slightly up to total strain of 183 $\mu\epsilon$. The creep at 26 $\mu\epsilon$ total strain was not recovered at all while the creep at 78 $\mu\epsilon$ was partly recovered. The amount of three creep was slightly increasing. There was a ‘step-like’ deformation at 31 $\mu\epsilon$ total strain from -0.5 $\mu\epsilon$ to 1.5 $\mu\epsilon$.

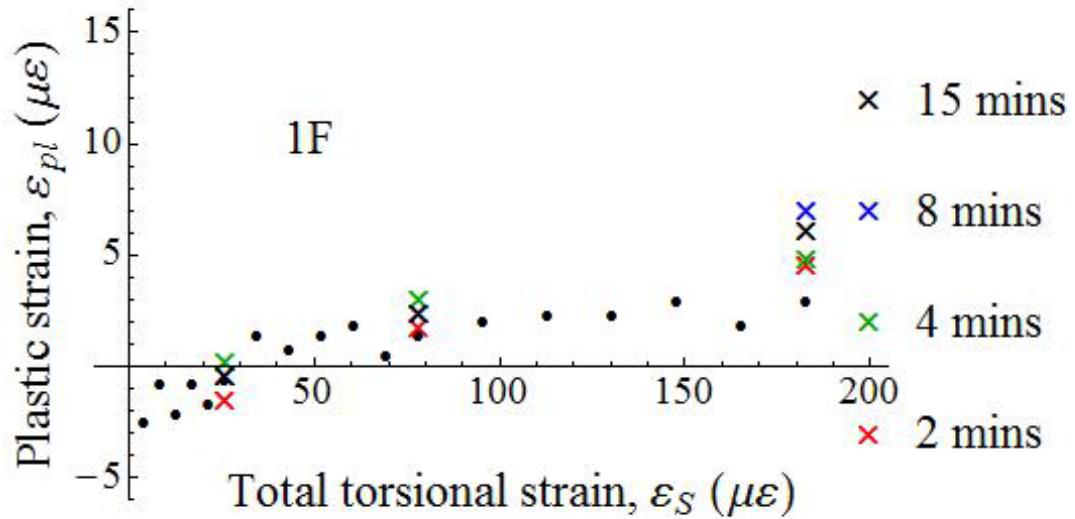


Figure 3.5 Plastic strain vs total torsional strain for a copper wire of 25 μm diameter, 0.5 m length, annealed at 800 $^{\circ}\text{C}$ 90s, grain size 10 μm . The black dots • are the successive load-unload data points for 1F loading. Creep test data are indicated by the red, green, blue and black crosses, which represent successive loading for 2, 4, 8 and 15 minutes.

Figure 3.6 is a second 1F direction load-unload data on 25 micron diameter 0.5 meter length copper wire with moderate grain size 3.6 μm . Deformation was observed from the starting point. The data was scattered around the x -axis up to 183 $\mu\epsilon$ total strain, from -6 $\mu\epsilon$ to 7 $\mu\epsilon$. The creep at 52 $\mu\epsilon$, 78 $\mu\epsilon$, 104 $\mu\epsilon$ and 131 $\mu\epsilon$ total strain was partly recovered. ‘Step-like’ deformation happened several times.

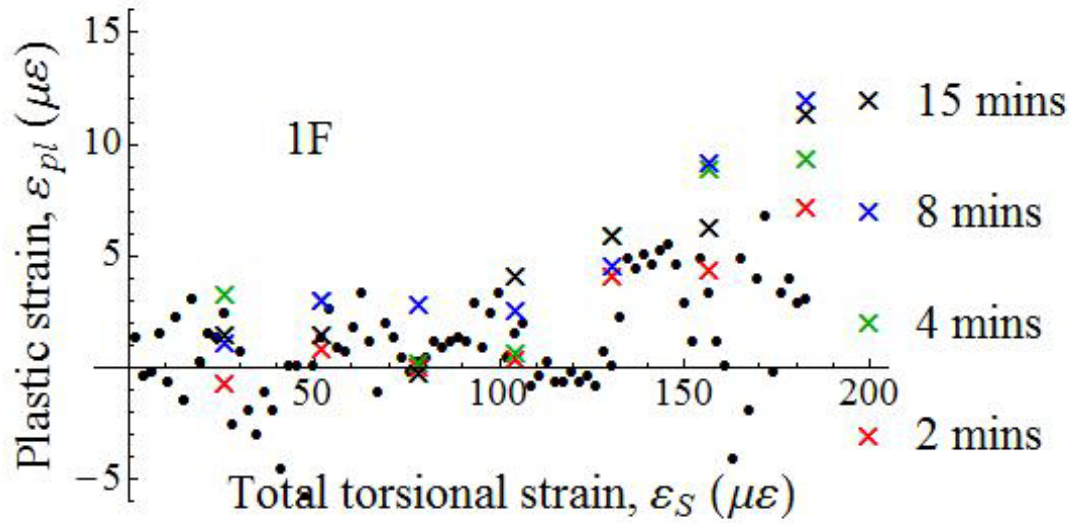


Figure 3.6 Plastic strain vs total torsional strain for a copper wire of 25 μm diameter, 0.5 m length, annealed at 750 $^{\circ}\text{C}$ 30s, grain size 3.6 μm . The black dots • are the successive load-unload data points for 1F loading. Creep test data are indicated by the red, green, blue and black crosses, which represent successive loading for 2, 4, 8 and 15 minutes.

Figure 3.7 is a third 1F direction load-unload data on 25 micron diameter 0.5 meter length copper wire with finest grain size 3.2 μm . The data was quite flat until 21 $\mu\epsilon$ total strain. Then the data was scattered around the x -axis up to total strain of 157 $\mu\epsilon$. After that, the deformation increased. The creep at 52 $\mu\epsilon$ total strain was fully recovered while the creep at 157 $\mu\epsilon$ and at 183 $\mu\epsilon$ total strain were partly recovered. The amount of creep was increasing gradually. ‘Step-like’ deformation occurred from 4.4 $\mu\epsilon$ to 7.2 $\mu\epsilon$ at 164 $\mu\epsilon$ total strain, and from 9.0 $\mu\epsilon$ to 3.7 $\mu\epsilon$ at 175 $\mu\epsilon$ total strain.

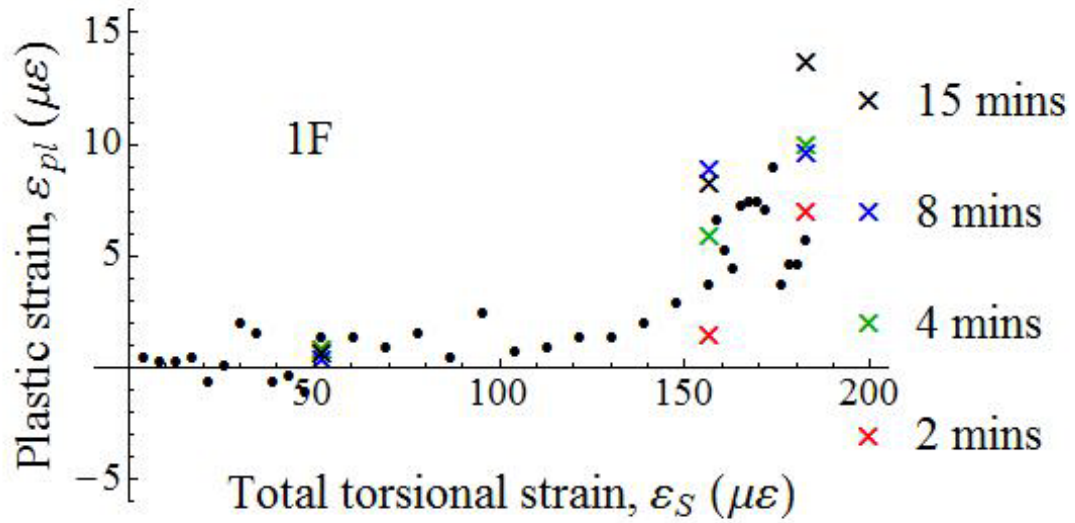


Figure 3.7 Plastic strain vs total torsional strain for a copper wire of 25 μm diameter, 0.5 m length, annealed at 650 $^{\circ}\text{C}$ 15s, grain size 3.2 μm . The black dots • are the successive load-unload data points for 1F loading. Creep test data are indicated by the red, green, blue and black crosses, which represent successive loading for 2, 4, 8 and 15 minutes.

3.2.3 Result of 20 μm diameter copper wire

Figure 3.8 is a 1F direction load-unload data on 20 micron diameter 0.5 meter length copper wire with grain size 7.7 μm . The data was scattered around $\varepsilon_{pl} = 3 \mu\epsilon$ up to 170 $\mu\epsilon$ total strain. The creep at 20 $\mu\epsilon$, 62 $\mu\epsilon$ and 125 $\mu\epsilon$ was all partly recovered. ‘Step-like’ deformation occurred from 3.2 $\mu\epsilon$ to 10.1 $\mu\epsilon$ at 141 $\mu\epsilon$ total strain, from 8 $\mu\epsilon$ to 2.7 $\mu\epsilon$ at 162 $\mu\epsilon$ total strain and from 3.7 $\mu\epsilon$ to 9.7 $\mu\epsilon$ at 182 total strain.

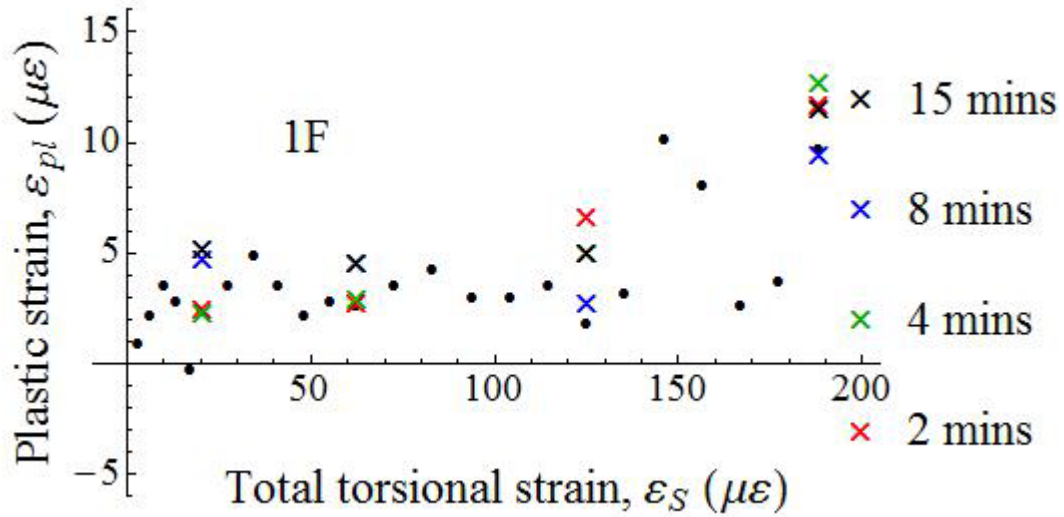


Figure 3.8 Plastic strain vs total torsional strain for a copper wire of 20 μm diameter, 0.5 m length, annealed at 750 °C 120s, grain size 7.7 μm . The black dots • are the successive load-unload data points for 1F loading. Creep test data are indicated by the red, green, blue and black crosses, which represent successive loading for 2, 4, 8 and 15 minutes.

3.2.4 Result of 18 μm diameter copper wire

Figure 3.9 is a 1F direction load-unload data on 18 micron diameter 0.25 meter length copper wire with grain size 6.9 μm . The data was scattered around the x -axis up to 170 $\mu\epsilon$ total strain.

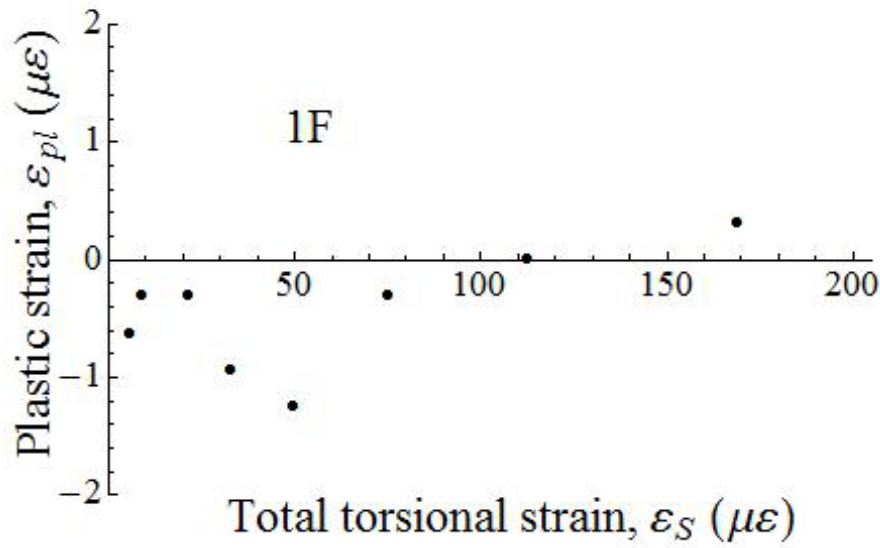


Figure 3.9 Plastic strain vs total torsional strain for a copper wire of 18 μm diameter, 0.25 m length, annealed at 650 $^{\circ}\text{C}$ 90s, grain size 6.5 μm . The black dots • are the successive load-unload data points for 1F loading.

3.3 Reverse loading

After the observation of the onset of deformation in monotonic tests, cyclic deformation was also studied.

3.3.1 Results of 50 μm diameter copper wire

Figure 3.10 and Figure 3.11 are a series of forward (1F and 3F) and backward (2B and 4B) cycles in 50 μm diameter copper wire with grain size 12 μm . In Figure 3.10 the first forward and backward cycles are shown to a total strain of 180 $\mu\epsilon$, -130 $\mu\epsilon$. Deformation was observed from the beginning. It increased gradually both in 1F and 2B with the total strain. Creep was quite small in this low strain area. It was fully recovered up to -130 $\mu\epsilon$ and 180 $\mu\epsilon$ total strain.

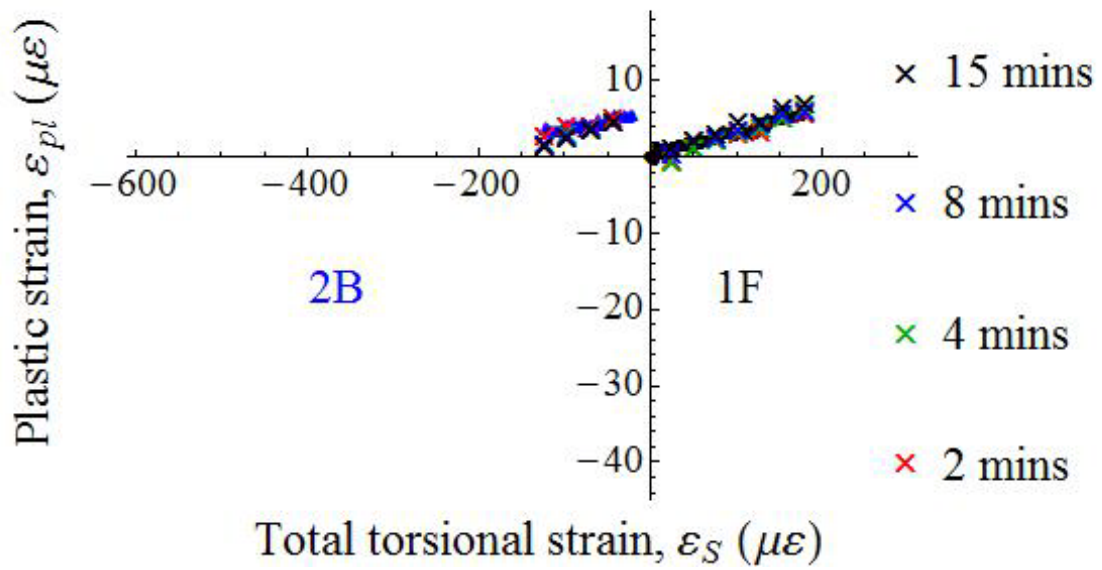


Figure 3.10 Plastic strain vs total torsional strain for a copper wire of 50 μm diameter, 1 m length, annealed at 850 $^{\circ}\text{C}$ 60s. The black dots \bullet are the successive load-unload data points for 1F loading and blue triangle \blacktriangle are the load-unload data for first reversal (2B) loading. Creep test data are indicated by the red, green, blue and black crosses, which represent successive loading for 2, 4, 8 and 15 minutes.

In Figure 3.11, the second forward and backward cycles are shown to a total strain of 180 $\mu\epsilon$, -260 $\mu\epsilon$. In 3F, the data was quite flat until 100 $\mu\epsilon$ total strain. Then the deformation increased gradually. Creep slightly increased at larger total strain. It was fully recovered. On reversing to 4B, creep became larger on higher strain. It was only partly recovered here.

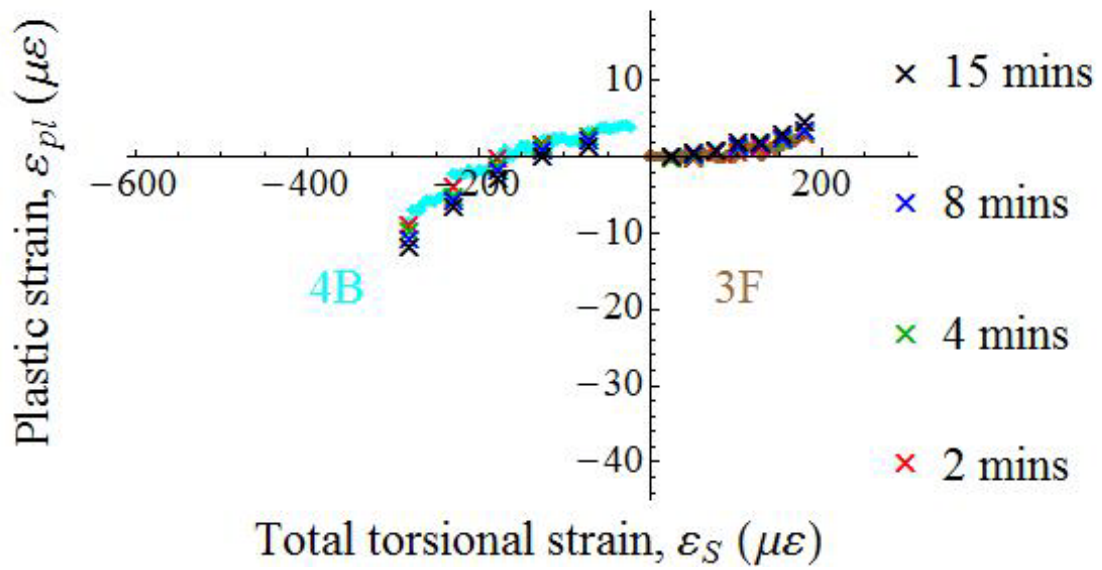


Figure 3.11 Plastic strain vs total torsional strain for a copper wire of 50 μm diameter, 1 m length, annealed at 850 $^{\circ}\text{C}$ 60s. The brown dots \bullet are the successive load-unload data points for 3F loading and cyan rhombus \blacklozenge are the load-unload data for second reversal (4B) loading. Creep test data are indicated by the red, green, blue and black crosses, which represent successive loading for 2, 4, 8 and 15 minutes.

Figure 3.12 and Figure 3.13 are second series of forward (1F and 3F) and backward (2B and 4B) cycles in 50 μm diameter copper wire with grain size 3.3 μm . In 1F of Figure 3.12, the data was extremely stable up to 155 $\mu\text{ε}$ total strain. Then the deformation increased gradually. Creep clearly increased at larger total strain. The creep at 50 $\mu\text{ε}$ and 100 $\mu\text{ε}$ total strain was fully recovered while the creep at 155 $\mu\text{ε}$, 208 $\mu\text{ε}$ and 259 $\mu\text{ε}$ total strain was partly recovered. On reversing, the deformation in 2B increased faster than 1F. Creep was partly recovered at -70 $\mu\text{ε}$ total strain while fully recovered at -121 $\mu\text{ε}$ and -174 $\mu\text{ε}$ total strain. ‘Step-like’ deformation at -70 $\mu\text{ε}$ total strain occurred from 8.2 $\mu\text{ε}$ to 3.9 $\mu\text{ε}$.

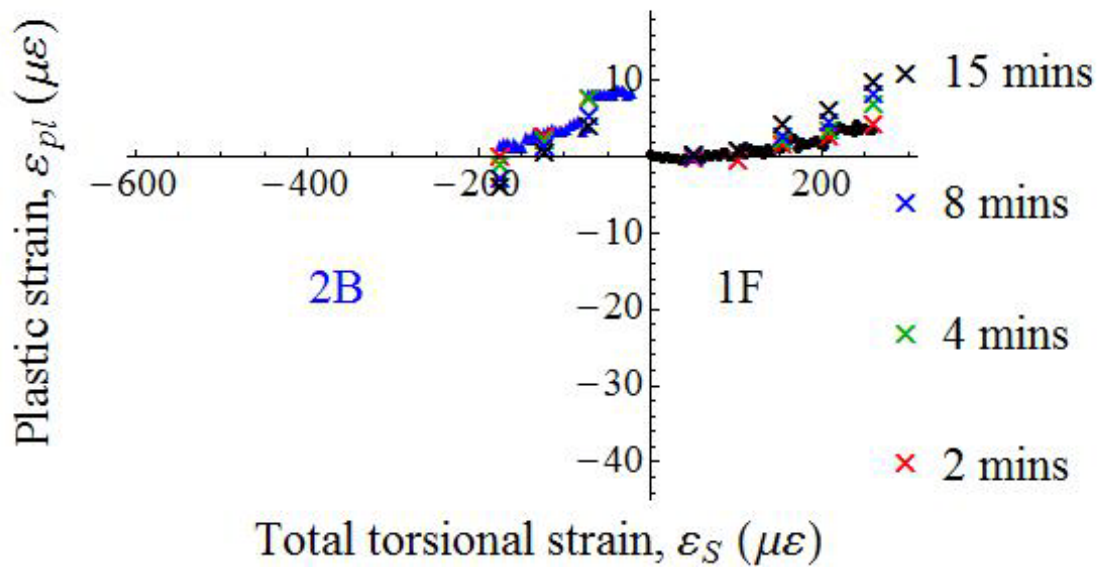


Figure 3.12 Plastic strain vs total torsional strain for a copper wire of 50 μm diameter, 1 m length, annealed at 650 $^{\circ}\text{C}$ 30s. The black dots • are the successive load-unload data points for 1F loading and blue triangle ▲ are the load-unload data for first reversal (2B) loading. Creep test data are indicated by the red, green, blue and black crosses, which represent successive loading for 2, 4, 8 and 15 minutes.

In Figure 3.13, 3F and 4B are shown to a total strain of 262 $\mu\epsilon$, -567 $\mu\epsilon$. In 3F, the data was very steady up to 155 $\mu\epsilon$ total strain. After the creep at 155 $\mu\epsilon$ total strain, the data shows stability up to 260 $\mu\epsilon$ total strain. Creep increased gradually with total strain. Creep was partly recovered at 156 $\mu\epsilon$ total strain while completely recovered at 51 $\mu\epsilon$, 103 $\mu\epsilon$ and 208 $\mu\epsilon$ total strain. On reversing to 4B, the deformation grew much quicker than in 3F. Creep also became much larger on higher strain. It was only partly recovered.

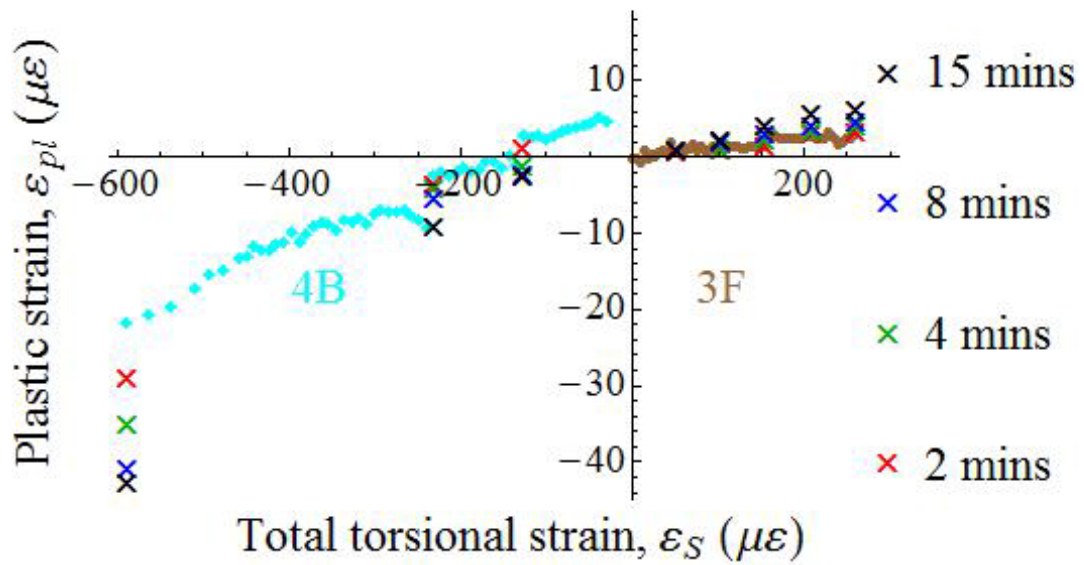


Figure 3.13 Plastic strain vs total torsional strain for a copper wire of 50 μm diameter, 1 m length, annealed at 650 $^{\circ}\text{C}$ 30s. The brown dots • are the successive load-unload data points for 3F loading and cyan rhombus ♦ are the load-unload data for second reversal (4B) loading. Creep test data are indicated by the red, green, blue and black crosses, which represent successive loading for 2, 4, 8 and 15 minutes.

Figure 3.14 and Figure 3.15 are the third series of forward (1F and 3F) and backward (2B and 4B) cycles in 50 μm diameter copper wire with grain size 2.6 μm . In the 1F of Figure 3.14, the data was extremely flat up to 78 $\mu\text{ε}$ total strain. After that, the deformation slightly increased while mainly happening during the creep tests. Creep gradually increased with total strain. It was partly recovered at 78 $\mu\text{ε}$ total strain while fully recovered at 26 $\mu\text{ε}$, 131 $\mu\text{ε}$ and 183 $\mu\text{ε}$ total strain. On reversing the loading direction to 2B, deformation was observed from the beginning. Creep was partly recovered at -146 $\mu\text{ε}$ total strain while fully recovered at -40 $\mu\text{ε}$ total strain. ‘Step-like’ deformation around -100 $\mu\text{ε}$ total strain occurred from 3.3 $\mu\text{ε}$ to 0 $\mu\text{ε}$.

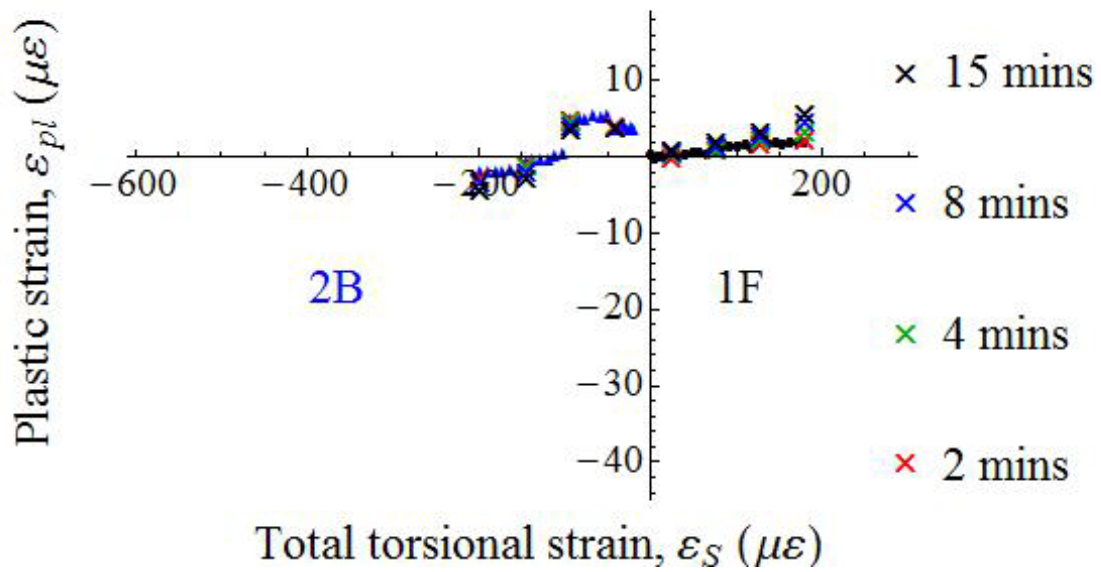


Figure 3.14 Plastic strain vs total torsional strain for a copper wire of 50 μm diameter, 1 m length, annealed at 500 $^{\circ}\text{C}$ 30s. The black dots • are the successive load-unload data points for 1F loading and blue triangle ▲ are the load-unload data for first reversal (2B) loading. Creep test data are indicated by the red, green, blue and black crosses, which represent successive loading for 2, 4, 8 and 15 minutes.

In Figure 3.15, 3F and 4B are shown to a total strain of 180 $\mu\epsilon$, -194 $\mu\epsilon$. In 3F, the data was quite flat up to 26 $\mu\epsilon$ total strain. Then the deformation increased slightly. Creep also increased with total strain. The creep was all fully recovered. On reversing, the deformation increased slowly while mainly occurring during creep tests. The creep increased gradually. It was always fully recovered. ‘Step-like’ deformation occurred around 30 $\mu\epsilon$ total strain, from -0.4 $\mu\epsilon$ to 1.5 $\mu\epsilon$.

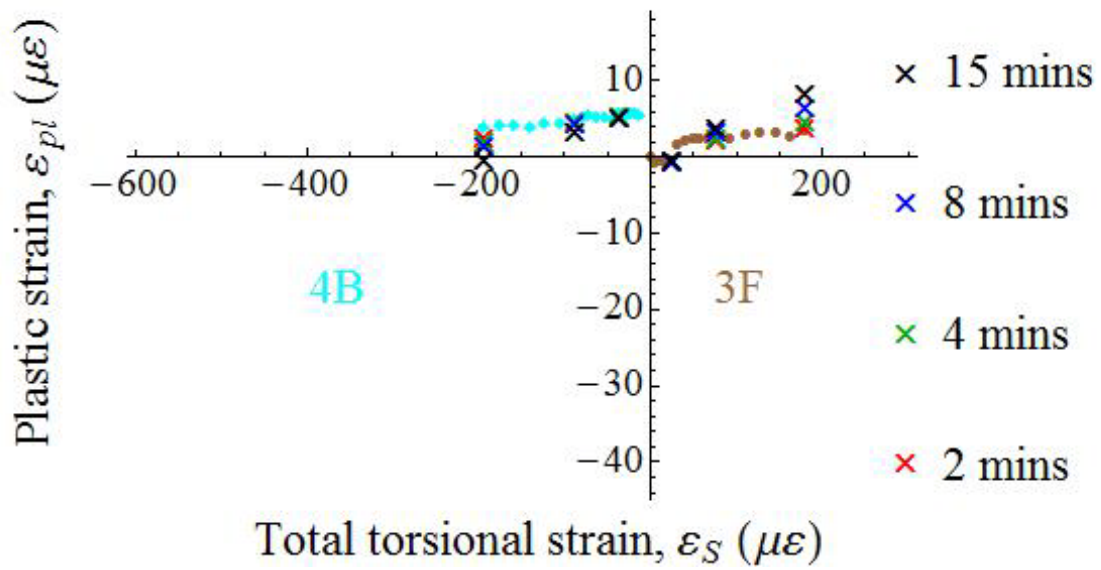


Figure 3.15 Plastic strain vs total torsional strain for a copper wire of 50 μm diameter, 1 m length, annealed at 500 $^{\circ}\text{C}$ 30s. The brown dots • are the successive load-unload data points for 3F loading and cyan rhombus \blacklozenge are the load-unload data for second reversal (4B) loading. Creep test data are indicated by the red, green, blue and black crosses, which represent successive loading for 2, 4, 8 and 15 minutes.

3.3.2 Results of 25 μm diameter copper wire

Figure 3.16 and Figure 3.17 are a series of forward (1F and 3F) and backward (2B and 4B) cycles in 25 μm diameter copper wire with grain size 10 μm . In Figure 3.16, 1F and 2B are shown to a total strain of -280 $\mu\epsilon$, 183 $\mu\epsilon$. In 3F the data was scattered around the x -axis up to 104 $\mu\epsilon$ total strain. Then it was increased gradually. Creep was increased slightly with the total strain. It was fully recovered before 104 $\mu\epsilon$ total strain while partly recovered from 104 $\mu\epsilon$ to 180 $\mu\epsilon$ total strain. Reversing to 2B direction, the deformation was observed from the beginning. It increased largely up to -60 $\mu\epsilon$ total strain. Afterwards it was scattered around the x -axis again. Creep increased gradually with the total strain. It was fully recovered.

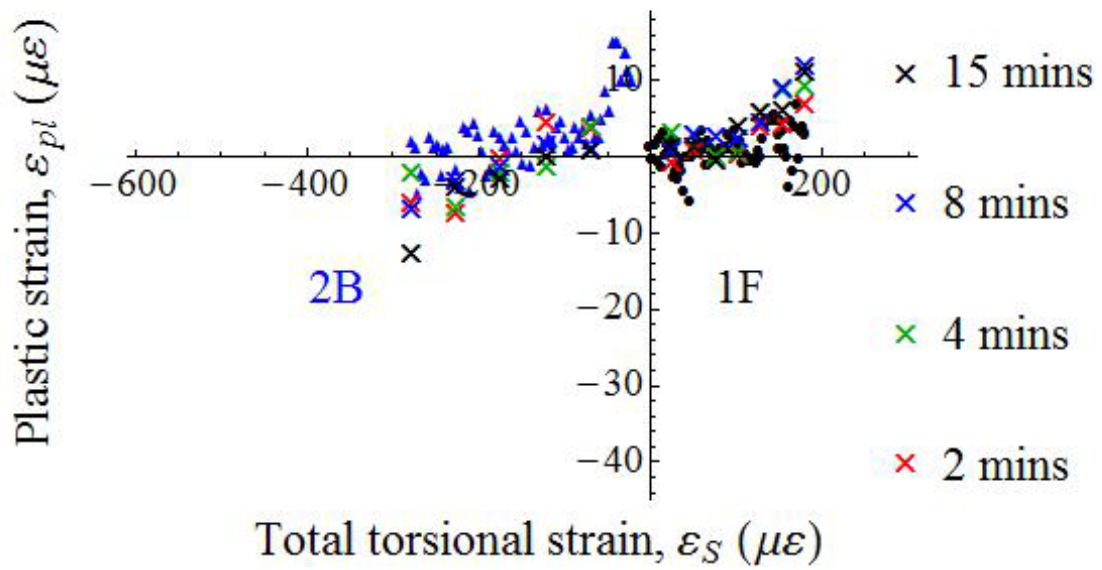


Figure 3.16 Plastic strain vs total torsional strain for a copper wire of 25 μm diameter, 0.5 m length, annealed at 750 $^{\circ}\text{C}$ 30s. The black dots • are the successive load-unload data points for 1F loading and blue triangle ▲ are the load-unload data for first reversal (2B) loading. Creep test data are indicated by the red, green, blue and black crosses, which represent successive loading for 2, 4, 8 and 15 minutes.

In Figure 3.17, 3F and 4B are shown to a total strain of 260 $\mu\epsilon$, -480 $\mu\epsilon$. In 3F, the data was scattered around the x -axis up to 155 $\mu\epsilon$ total strain. It increased with much noise until 260 $\mu\epsilon$ total strain. Creep increased with total strain. It was fully recovered before 101 $\mu\epsilon$ total strain while partly recovered afterwards. On reversing to 4B, the deformation increased faster than 3F and mainly happening during creep tests. Creep increased with total strain. And it was partly recovered.

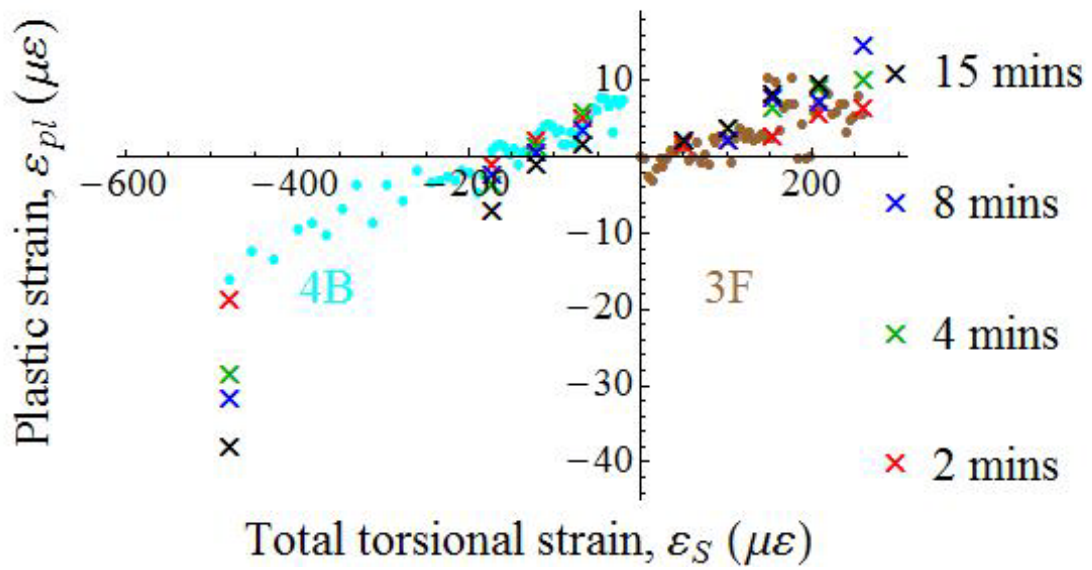


Figure 3.17 Plastic strain vs total torsional strain for a copper wire of 25 μm diameter, 0.5 m length, annealed at 750 $^{\circ}\text{C}$ 30s. The brown dots • are the successive load-unload data points for 3F loading and cyan rhombus \blacklozenge are the load-unload data for second reversal (4B) loading. Creep test data are indicated by the red, green, blue and black crosses, which represent successive loading for 2, 4, 8 and 15 minutes.

Figure 3.18 and Figure 3.19 are a second series of forward (1F and 3F) and backward (2B and 4B) cycles in 25 μm diameter copper wire with grain size of 3.2 μm . In Figure 3.18, 1F and 2B are shown to a total strain of -120 $\mu\epsilon$, 183 $\mu\epsilon$. The data was fairly stable up to 150 $\mu\epsilon$ total strain. The deformation then increased. Creep increased gradually. It was fully recovered at 52 $\mu\epsilon$ total strain while partly recovered at 157 $\mu\epsilon$ and 183 $\mu\epsilon$ total strain. On reversing to 2B, the deformation increased much faster than 1F. Creep slightly increased. And it was fully recovered up to -70 $\mu\epsilon$ total strain while partly recovered from -70 $\mu\epsilon$ to -120 $\mu\epsilon$ total strain.

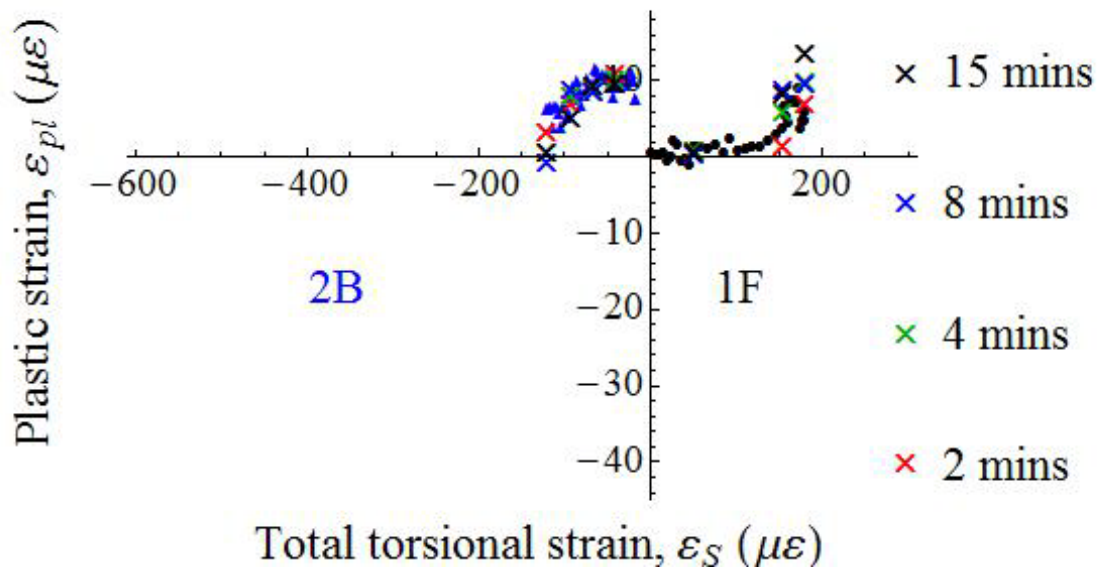


Figure 3.18 Plastic strain vs total torsional strain for a copper wire of 25 μm diameter, 0.5 m length, annealed at 650 $^{\circ}\text{C}$ 15s. The black dots • are the successive load-unload data points for 1F loading and blue triangle ▲ are the load-unload data for first reversal (2B) loading. Creep test data are indicated by the red, green, blue and black crosses, which represent successive loading for 2, 4, 8 and 15 minutes.

In Figure 3.19, 3F and 4B are shown to a total strain of 230 $\mu\epsilon$, -510 $\mu\epsilon$. In 3F the deformation was observed from starting point. The data was scattered around the x -axis up to 230 $\mu\epsilon$ total strain. And it was increasing slowly. Creep was quite similar. It was partly recovered. Reversing the loading direction to 4B, the deformation increased clearly while mainly occurring during creep tests. Creep increased with total strain. It was fully recovered at -180 $\mu\epsilon$ total strain while partly recovered in the other four creep tests.

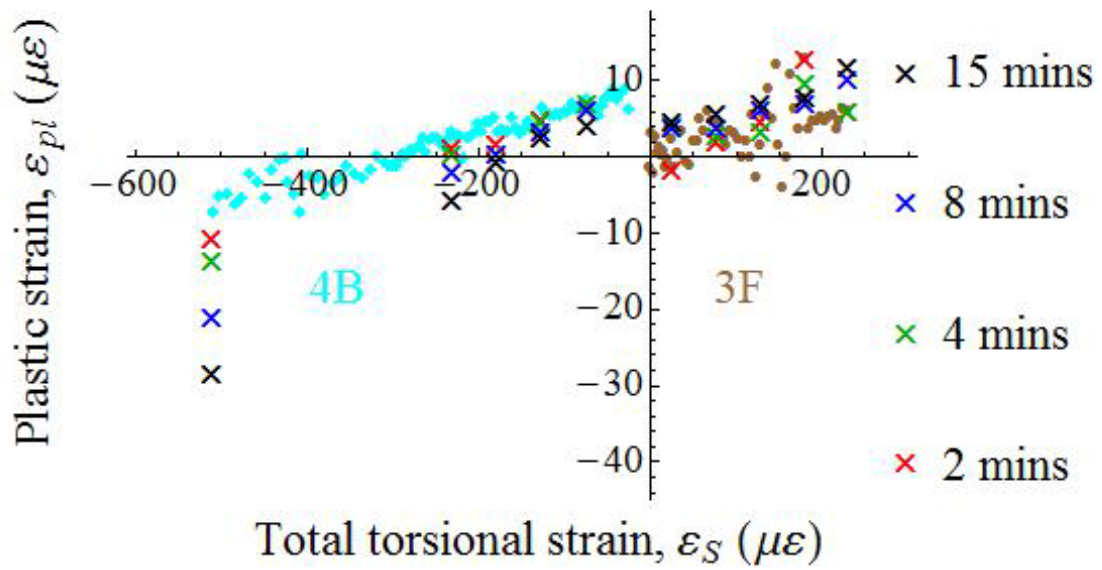


Figure 3.19 Plastic strain vs total torsional strain for a copper wire of 25 μm diameter 0.5 m length, annealed at 650 $^{\circ}\text{C}$ 15s. The brown dots • are the successive load-unload data points for 3F loading and cyan rhombus ◆ are the load-unload data for second reversal (4B) loading. Creep test data are indicated by the red, green, blue and black crosses, which represent successive loading for 2, 4, 8 and 15 minutes.

3.4 Thermal recovery

Figure 3.20 shows data for a 50 μm diameter 1 meter length copper wire with grain size of 8 μm . The data was scattered around the x -axis up to 25 $\mu\epsilon$ total strain. It was fairly stable from 25 $\mu\epsilon$ to 78 $\mu\epsilon$ total strain. Then deformation increased clearly with total strain. Creep increased slowly. The thermal anneals at 26 $\mu\epsilon$ and 78 $\mu\epsilon$ total strain gave strain recoveries even more than any deformation so far imposed. That is, the wire untwisted to -2 $\mu\epsilon$ and then -4 $\mu\epsilon$, beyond its starting position.

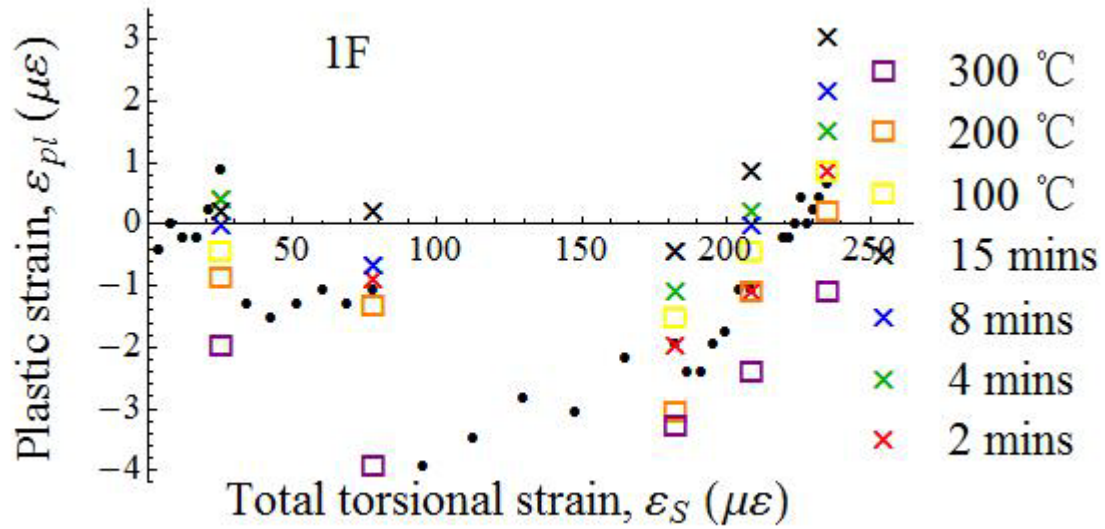


Figure 3.20 Plastic strain vs total torsional strain for a copper wire of 50 μm diameter, 1 m length, average grain size 8 μm . The black dots • are the successive load-unload data points for 1F loading. Creep test data are indicated by the red, green, blue and black crosses, which represent successive loading for 2, 4, 8 and 15 minutes. Thermally-induced plastic recovery data are indicated by the yellow, orange and purple squares, which represent successive heating to 100, 200 and 300°C.

Figure 3.21 are a series of forward (F) and backward (B) cycles load-unload data on 50 micron diameter 1 meter length copper wire with large grain size 8 μm . In (a) and (b), the first two forward and backward cycles (1F & 2B, 3F & 4B) are shown to a total strain of + 80 $\mu\epsilon$, -100 $\mu\epsilon$. Deformation was observed from the outset while appearing to happen mainly during the creep tests. Deformation increased slowly. Creep was all fully recovered with the exception of 100 $\mu\epsilon$ total strain in 4B. ‘Step-like’ deformation at -65 $\mu\epsilon$ total strain in 2B occurred from 2.3 $\mu\epsilon$ to 1.2 $\mu\epsilon$ and at 14 $\mu\epsilon$ total strain in 3F occurred from 1.5 $\mu\epsilon$ to 2.6 $\mu\epsilon$. In (c), data was fairly stable up to 78 $\mu\epsilon$ total strain in 5F. Deformation then increased with total strain. Creep gradually increased and fully recovered by thermal annealing. On reversing to 6B, deformation was observed immediately and increased much faster. Creep also

increased gradually. It was fully recovered at $-42\ \mu\epsilon$ and $-95\ \mu\epsilon$ total strain while partly recovered at $-147\ \mu\epsilon$ and $200\ \mu\epsilon$ total strain.

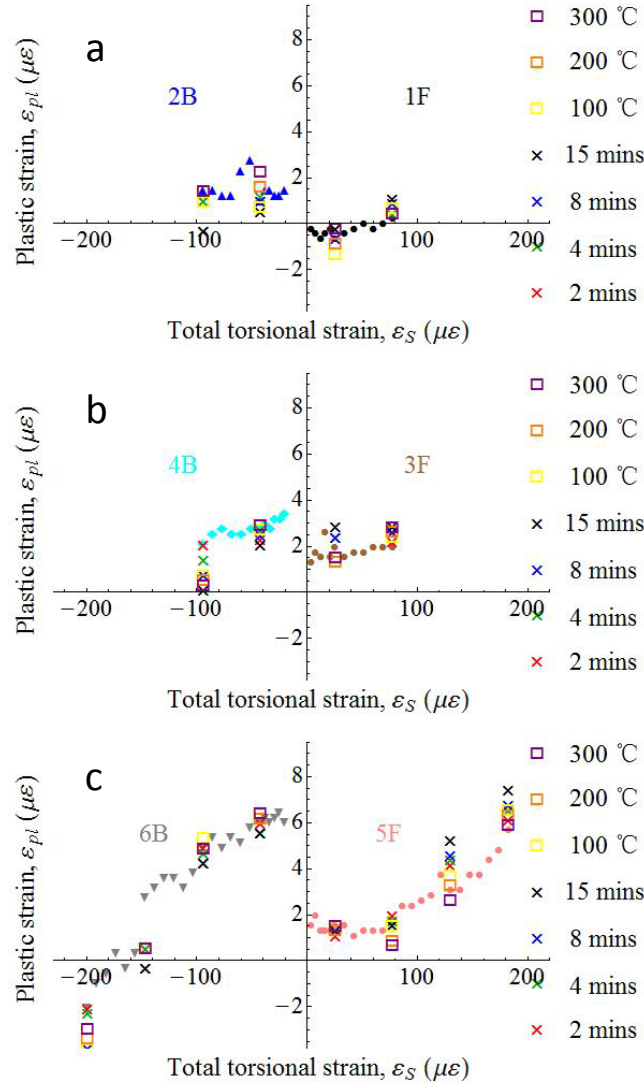


Figure 3.21 Plastic strain vs total torsional strain for a copper wire of 50 μm diameter 1 m length, average grain size is 8 μm . The black, brown and pink dots • are the successive load-unload data points for forwards loading and blue \blacktriangle , cyan \blacklozenge and grey \blacktriangledown are the successive load-unload data points for reverse loading. Creep test data are indicated by the red, green, blue and black crosses, which represent successive loading for 2, 4, 8 and 15 minutes. Thermally-induced plastic recovery data are indicated by the yellow, orange and purple squares, which represent successive heating to 100, 200 and 300°C. a) first forward 1F and reverse 2B cycles, b) second forwards 3F and reverse 4B cycles, c) third forwards 5F and reverse 6B cycles.

3.5 Summary

3.5.1 Sensitivity

There are many cases where the scatter in the data is as little as 1 $\mu\epsilon$ or better, e.g. from 160 $\mu\epsilon$ to 183 $\mu\epsilon$ total strain in Figure 3.2, from 105 $\mu\epsilon$ to 157 $\mu\epsilon$ total strain in Figure 3.3 and from 130 $\mu\epsilon$ to 183 $\mu\epsilon$ total strain in Figure 3.4. Other times, the scatter between successive points is around 2 $\mu\epsilon$, e.g. from 0 $\mu\epsilon$ to 26 $\mu\epsilon$ total strain in Figure 3.2, from 157 $\mu\epsilon$ to 183 $\mu\epsilon$ total strain in Figure 3.3.

In the smaller wires, these scatter become 5 $\mu\epsilon$ or more as seen e.g. from 157 $\mu\epsilon$ to 183 $\mu\epsilon$ in Figure 3.6, from 157 $\mu\epsilon$ to 183 $\mu\epsilon$ in Figure 3.7 and from 135 $\mu\epsilon$ to 188 $\mu\epsilon$ in Figure 3.8.

From this, the sensitivity is smaller than 1 $\mu\epsilon$ for 50 μm diameter wire, 5 $\mu\epsilon$ for 25 μm diameter wire, 5 $\mu\epsilon$ for 20 μm diameter wire and 2 $\mu\epsilon$ for 18 μm diameter wire. Then, we consider that the small scatter is the random error in the data from reading the unload angle, while the larger scatter is actually due to dislocation events in the wire. What event, is not fully understood here. The reason may be due to the unstable plastic table, metro passed by *etc.*

3.5.2 Elastic limit

Where the data is flat to within the random error we call this elastic deformation within the sensitivity. For monotonic loading, this occurs in Figure 3.2 from 160 $\mu\epsilon$ to 183 $\mu\epsilon$ total strain, in Figure 3.3 from 155 $\mu\epsilon$ to 183 $\mu\epsilon$ total strain, in Figure 3.4 from 130 $\mu\epsilon$ to 182 $\mu\epsilon$ total strain, in Figure 3.5 from 90 $\mu\epsilon$ to 170 $\mu\epsilon$ total strain, in Figure 3.6 from 157 $\mu\epsilon$ to 183 $\mu\epsilon$, in Figure 3.7 from 60 $\mu\epsilon$ to 103 $\mu\epsilon$ total strain, in Figure 3.8 from 62 $\mu\epsilon$ to 125 $\mu\epsilon$ total strain, in Figure 3.9 from 70 $\mu\epsilon$ to 170 $\mu\epsilon$ total strain.

Therefore the yield points defined by the elastic sensitivity limit in monotonic loading are 160 $\mu\epsilon$ in Figure 3.6, 140 $\mu\epsilon$ in Figure 3.7 and 150 $\mu\epsilon$ in Figure 3.8. The earlier data is still in the

elastic region.

For cyclic loading, this occurs in Figure 3.11 from 130 $\mu\epsilon$ to 155 $\mu\epsilon$ total strain of 3F and -180 $\mu\epsilon$ to -230 $\mu\epsilon$ total strain of 4B, in Figure 3.12 from 210 $\mu\epsilon$ to 260 $\mu\epsilon$ total strain of 1F and from -20 $\mu\epsilon$ to -70 $\mu\epsilon$ total strain of 2B, in Figure 3.13 from 207 $\mu\epsilon$ to 260 $\mu\epsilon$ total strain of 3F and from -130 $\mu\epsilon$ to -230 $\mu\epsilon$ total strain of 4B, in Figure 3.14 from 130 $\mu\epsilon$ to 180 $\mu\epsilon$ total strain of 1F and from -145 $\mu\epsilon$ to -200 $\mu\epsilon$ total strain of 2B, in Figure 3.15 from 77 $\mu\epsilon$ to 180 $\mu\epsilon$ total strain of 3F and from -88 $\mu\epsilon$ to -194 $\mu\epsilon$ total strain of 4B, in Figure 3.17 from 208 $\mu\epsilon$ to 260 $\mu\epsilon$ total strain of 3F and from -173 to -242 $\mu\epsilon$ total strain of 4B, in Figure 3.18 from 52 $\mu\epsilon$ to 130 $\mu\epsilon$ total strain of 1F and -38 $\mu\epsilon$ to -65 $\mu\epsilon$ total strain of 2B, in Figure 3.19 from 182 $\mu\epsilon$ to 230 $\mu\epsilon$ total strain of 3F and from -127 $\mu\epsilon$ to -180 $\mu\epsilon$ total strain of 4B.

Therefore the yield points by the elastic sensitivity limit that appear in cyclic loading are 170 $\mu\epsilon$ in Figure 3.11 and -450 $\mu\epsilon$ in Figure 3.13. The yield points in Figure 3.16 and Figure 3.18 are the same as in monotonic loading. The earlier data is still in the elastic region.

For cyclic loading with thermal-induced recovery, this occurs in Figure 3.20 from 25 $\mu\epsilon$ to 78 $\mu\epsilon$ total strain of 1F, in Figure 3.21 from 0 $\mu\epsilon$ to 78 $\mu\epsilon$ total strain of 1F, 3F and 5F, from -21 $\mu\epsilon$ to -96 $\mu\epsilon$ total strain of 2B, 4B and 6B.

Therefore the yield points by the elastic sensitivity limit that appear in cyclic loading with thermal recovery are 130 $\mu\epsilon$ in Figure 3. 20 and 160 $\mu\epsilon$ in Figure 3.21.

Then the yield points by elastic limit were plotted against the grain size and wire radius (sample size), see Figure 3.22. Except for the 50 micron diameter grain size 3.3 μm copper wire, all other data show no clear correlation with the grain size or wire radius.

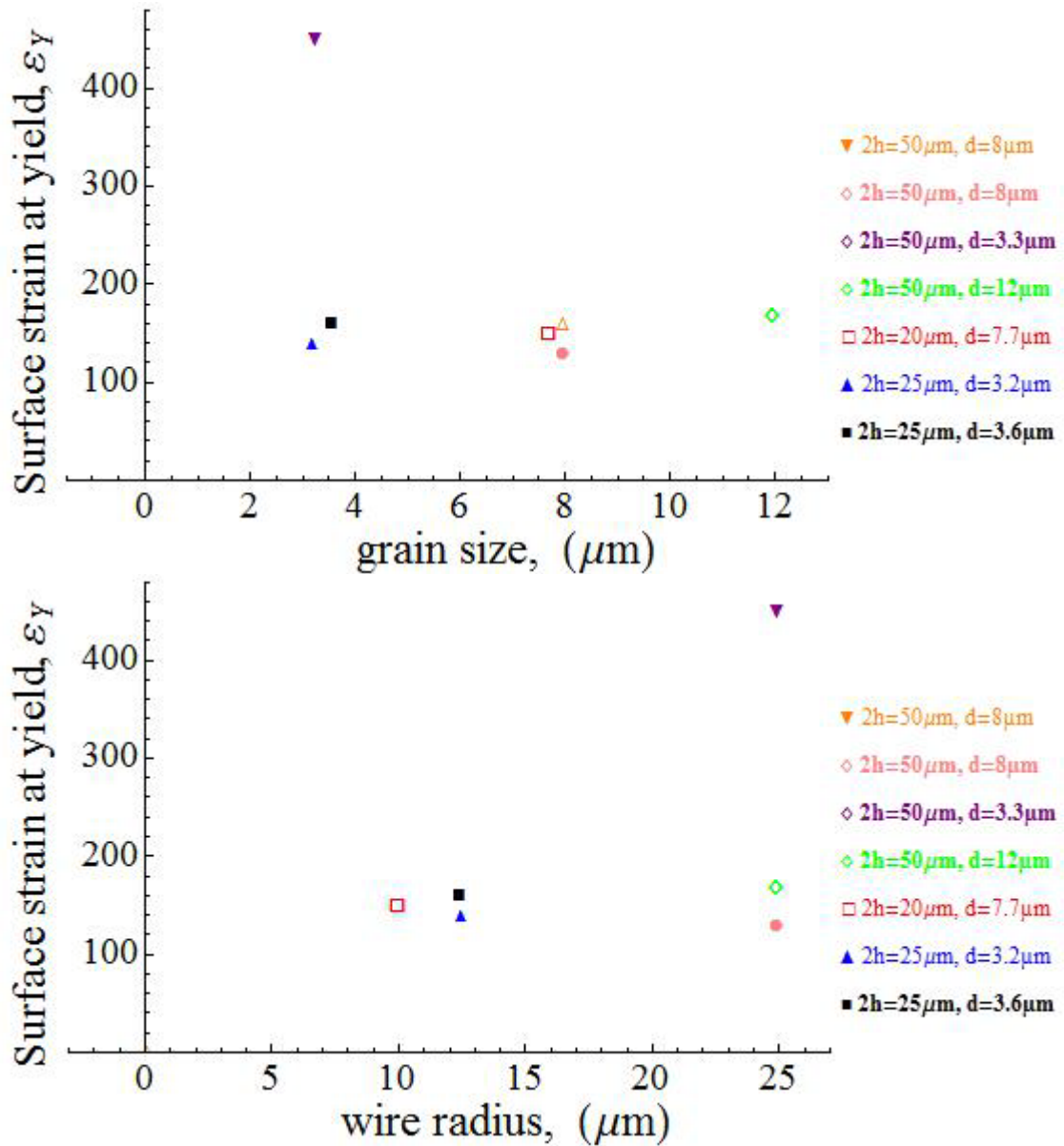


Figure 3.22 Yield strain (elastic sensitivity limit) versus grain size and wire radius (sample size) in low strain

3.5.3 Creep

Creep deformation generally increased with time increasing, as seen in Figure 3.1 inset. However, there were lots of exceptions, e.g. as seen in the creep at 26 $\mu\epsilon$ total strain in Figure 3.5, the wire was recovered firstly (red cross) then deformed further (green cross), and finally recovered to its original position; or in the creep at 183 $\mu\epsilon$ total strain in the same figure, it was deforming up to 8 minutes creep then turned to recovery at 15 minutes creep.

Creep was normally larger at higher strain, as seen in the four creep tests in Figure 3.4. However, there are no significant differences among the seven creep tests at different strains in Figure 3.2.

3.5.4 Recovery

Two kinds of recovery behaviours occurred in all of the above; one is room temperature recovery (RTR) and the other is thermal-induced recovery (TR). The RTR is normally fully recovered in low strain, as seen in creep at 52 $\mu\epsilon$ total strain and 103 $\mu\epsilon$ total strain in Figure 3.2. On the other hand, there are part-recovery behaviours or even no recovery, as seen in creep at 78 $\mu\epsilon$ total strain and 26 $\mu\epsilon$ total strain in the same figure.

For the TR, it was fully recovered in low strain, as seen in Figure 3.21 from 0 $\mu\epsilon$ to 100 $\mu\epsilon$ total strain. It was partly recovered in high strain, as seen in Figure 3.21 (c) from 130 $\mu\epsilon$ total strain. There is also exception as seen in Figure 3.20, the creep at 26 $\mu\epsilon$ and 78 $\mu\epsilon$ total strain were recovered much further than its original position.

3.5.5 Cyclic loading (Bauschinger effect)

Reversing the load direction in low strain, as seen in Figure 3.21 (a) and (b), the deformation was only up to 2 $\mu\epsilon$. There are no significant differences between the forward loading direction (1F, 3F) and backward loading direction (2B, 4B).

Reversing loading at relatively higher strain, as seen in Figure 3.21 (c), the reversing loading (6B) grew faster than the forward loading (5F).

4. High strain torsion results

4.1 Strengthening background of metal materials

It is generally understood that in metallic crystals, plastic deformation is usually caused on a microscopic scale by defects called dislocations, which are generated and moved by shear stress within the crystals. The strength of metal materials is generally determined by the ability of dislocations to multiply and move through the crystalline material. Therefore strengthening of metals depends on reducing the dislocation motions. Mechanisms of strengthening include grain boundary strengthening, solid solution strengthening and strain hardening.

In grain boundary strengthening, the grain boundaries act as obstacle hindering further dislocation spread. Therefore energy is required for dislocations to change direction or pass the boundaries or be generated in the neighbouring grains. The extra energy will hence increase the yield strength of the materials. Generally, the area of grain boundaries increases with decreasing grain size. Dislocation propagation is more difficult as a result. The relation of this strengthening mechanism was named as Hall-Petch [5, 6] effect:

$$\sigma_y = \sigma_0 + \frac{k_d}{\sqrt{d}} \quad \text{Equation 4.1}$$

where σ_y is the yield stress, σ_0 is a materials constant for the starting stress for dislocation movement (or the resistance of the lattice to dislocation motion), k_d is the strengthening coefficient (a constant specific to each material), and d is the average grain diameter. Recently, Dunstan *et al.* [46] have suggested that this relationship is not the best description of grain size strengthening and describe the behaviour in terms of dislocation source size within the crystals. The stress to operate a dislocation source is inversely proportional to the grain size.

Solid solution strengthening is due to atoms of another element that goes into interstitial or substitutional positions in the crystal. The solute atoms cause lattice distortions that hinder dislocation propagation. Local stress fields around solute atoms are formed. They interact with nearby dislocations, which also causes the increasing in the yield strength. Therefore the strength of the material is enhanced.

Strain hardening, also known as work hardening or cold working, is the strengthening of a metal by plastic deformation when a metal is beyond the yield point. At normal temperatures the dislocations are not removed by annealing. Instead, the dislocations accumulate and may interact with each other. The material becomes increasingly saturated with dislocations, a resistance to dislocation motion develops and more dislocations hinder source operation, which leads to the observed strengthening in the material.

4.2 Work hardening background

4.2.1 Work hardening in singlecrystal

The typical stress–strain curve of single crystals is shown in Figure 4.1, more commonly observed in fcc structures but also applicable to the bcc lattice [47, 48]. Three regions of hardening are experimentally distinguishable.

Stage I, or the easy glide area, immediately follows the yield point and is characterized by a low rate of work hardening. The quantity of dislocation sources is constant, the slip planes are not piled-up with dislocations and the space between the moving dislocations is large.

Stage II, or the athermal hardening area, shows a rapid increase in work hardening rate. More dislocations are produced by new dislocation sources with increasing load. Then the dislocations start pile-up and restrain each other. As the most favourable slip plane are filled with pile-ups, multiple slip starts on all possible planes, which further restricts the dislocation movement. The stress needs to be increased significantly as the strain increases.

Stage III, or the parabolic hardening area, exhibits a decreasing rate of work-hardening. In contrast to the linear hardening, stage III is sensitive to temperature and strain rate.

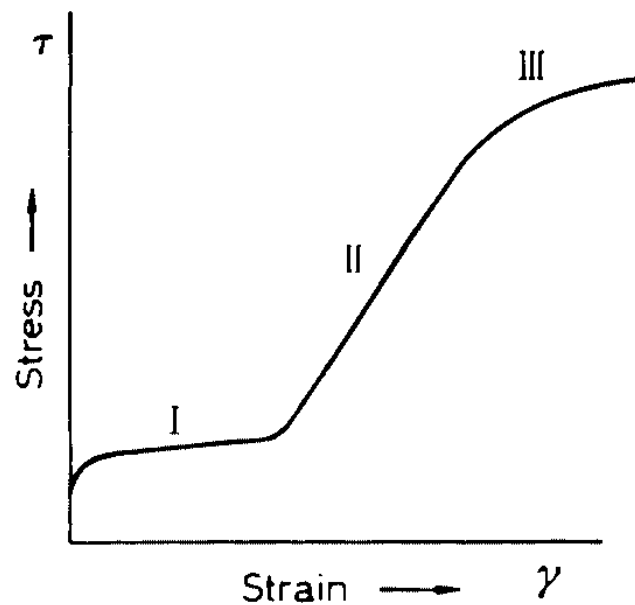


Figure 4.1 Three stages of stress–strain curve in single crystal (Reproduced from *Modern physical metallurgy and materials engineering*, 1999)

4.2.2 Work hardening in polycrystals

The stress-strain behaviour of fcc and bcc polycrystalline metals exhibits the same modes as in single crystals; interactions of dislocations give rise to local dislocation tangles gradually developing into three-dimensional networks. The stress-strain curve of an fcc polycrystalline material resembles the shape for the fcc single crystal, but occurs at higher stresses.

4.2.3 Work hardening theory

All theories of work-hardening depend on one assumption, announced by Taylor in 1934, that some dislocations become ‘stuck’ inside the crystal and act as sources of internal stress which opposes the motion of other gliding dislocations.

For a given dislocation distribution the dislocation density ρ is simply related to the flow stress τ by an equation of the form

$$\tau = \tau_0 + \alpha \mu b \rho^{1/2} \quad \text{Equation 4.2}$$

where α is a correction factor specific to the material, μ is the shear modulus, b is the magnitude of the Burgers vector and τ_0 is the intrinsic strength of the material with low dislocation density.

However, Taylor's theory only took account of the edge dislocations. Screw dislocations are not involved, hence cross-slip is not considered. Dislocations on different planes can trap each other and may not be able to move independently. Finally, deformation is not always homogeneous.

Many other theories of work-hardening similar to Taylor exist but all seem to be oversimplified, since work hardening depends not so much on individual dislocations as on the group behaviour of large quantities of them. The work-hardening behaviour in metals with a cubic structure is more complicated because of the large number of available slip systems. That is the reason why we need more experimental evidence related to these metals, particularly those with fcc structures.

4.3 High strain results

4.3.1 Deformation distribution

After the detailed low-strain experiments in previous chapter, a wire was measured under higher strains up to unit strain, $\epsilon_S = 1$. The very low strain data were collected using the whole 1 m wire. Then, to speed up the high-strain experiment, the wire was cut to several 20 cm lengths. Creep tests were carried out less frequently. In Figure 4.2, data from the bottom 20 cm is shown as 5F (black dots) and data from 20 cm taken from the middle 20 cm lengths is shown as 6F (red square). The creep deformation was much smaller in values than the total torsional strain. However, it increased gradually with total strain. We will discuss the creep in detail later in 4.3.3.

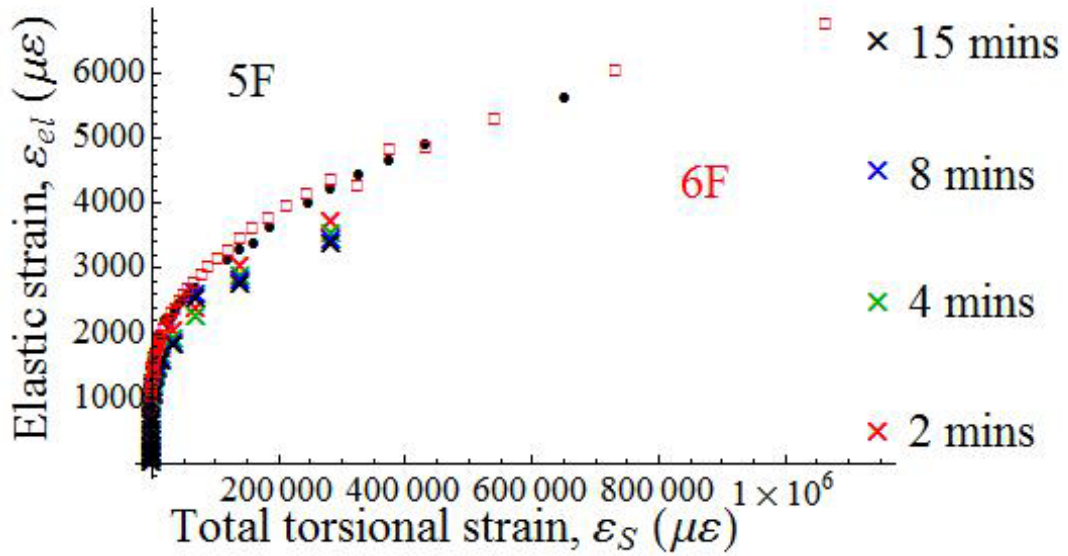


Figure 4.2 A wire taken to unity strain (50 μm diameter copper wire, 1m length, annealed at 850 $^{\circ}\text{C}$ for 60s , average grain size is about 20 μm). The dot symbols and squares are data for 2 different 20cm sections of the wire, 5F and 6F, taken to high strain. The red, green, blue and black crosses indicate creep under 2 minutes, 4 minutes, 8 minutes and 15 minutes load.

4.3.2 Strain hardening

Five different copper wires were taken to 1000 $\mu\text{ɛ}$ total strain (Figure 4.3). The plastic deformation increased slowly, almost flat up to 200 $\mu\text{ɛ}$ total strain. Then the deformation increased at various rates. The large grain size data, for $d \geq 10 \mu\text{m}$ (black dots and green rhombus), were increasing faster than the small grain size data, for $d \leq 10 \mu\text{m}$ (red square, blue triangle and purple inverted triangle).

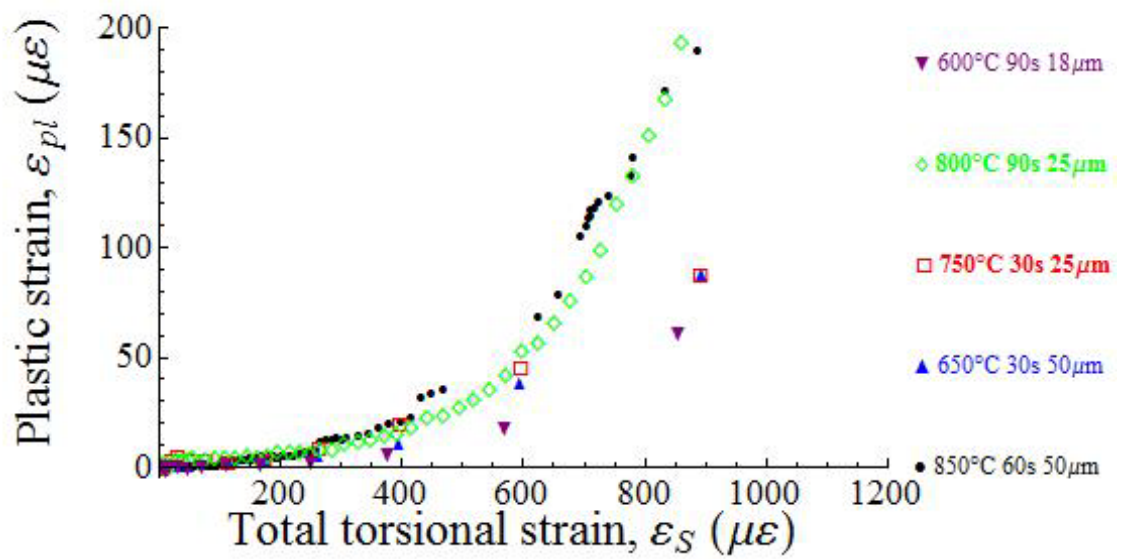


Figure 4.3 Five wires were taken to 1000 $\mu\epsilon$ total strain. The black dot \bullet symbols are 50 μm diameter copper wire, 1m length, annealed at 850 $^{\circ}\text{C}$ for 60s, grain size 12 μm ; the blue triangle \blacktriangle symbols are 50 μm diameter copper wire, 1m length, annealed at 650 $^{\circ}\text{C}$ for 30s, grain size 3.3 μm ; the red square \square symbols are 25 μm diameter copper wire, 0.5m length, annealed at 750 $^{\circ}\text{C}$ for 30s, grain size 3.6 μm ; the green rhombus symbols are 25 μm diameter copper wire, 0.5m length, annealed at 800 $^{\circ}\text{C}$ for 90s, grain size 10 μm ; the purple inverted triangle \blacktriangledown symbols are 18 μm diameter copper wire, 0.25m length, annealed at 600 $^{\circ}\text{C}$ for 90s, grain size 6.5 μm .

The same copper wires were then taken to unit strain in Figure 4.4. The elastic strain of smaller grain size data sets (red square and blue triangle) increased fast up to 4000 $\mu\epsilon$ elastic strain. Then the elastic strain increased slowly up to 1.1 ϵ total strain. The elastic strain of large grain size data sets (black dots, green rhombus and purple inverted triangle) increased fast up to 2000 $\mu\epsilon$ elastic strain. Then the elastic strain increased slowly up to 1.05 ϵ total strain. The elastic strain of small grain size data sets was clearly larger than the elastic strain of the large grain size data sets above 50000 $\mu\epsilon$ total strain.

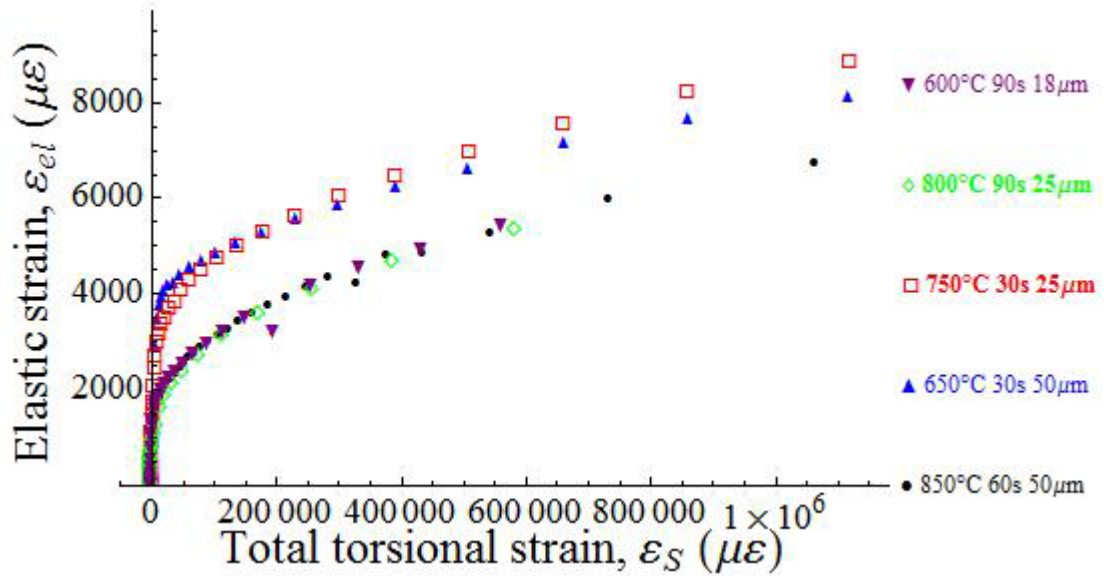


Figure 4.4 The wires of Figure 4. 3 taken to unity strain. The black dot • symbols are 50 μm diameter copper wire, 1m length, annealed at 850 $^{\circ}\text{C}$ for 60s, grain size 12 μm ; the blue triangle \blacktriangle symbols are 50 μm diameter copper wire, 1m length, annealed at 650 $^{\circ}\text{C}$ for 30s, grain size 3.3 μm ; the red square \square symbols are 25 μm diameter copper wire, 0.5m length, annealed at 750 $^{\circ}\text{C}$ for 30s, grain size 3.6 μm ; the green rhombus \diamond symbols are 25 μm diameter copper wire, 0.5m length, annealed at 800 $^{\circ}\text{C}$ for 90s, grain size 10 μm ; the purple inverted triangle \blacktriangledown symbols are 18 μm diameter copper wire, 0.25m length, annealed at 600 $^{\circ}\text{C}$ for 90s, grain size 6.5 μm .

4.3.3. Creep deformation

To illustrate the creep behaviour, the creep data in Figure 4.4 were plotted in a log-log coordinate system in Figure 4.5. The x-axes are total torsion strain and elastic strain while y-axes are the creep deformation. Overall, in the left figure all data are shown as two straight lines. The slope of data in the low strain region is larger than the slope of data in the high strain region. In the right figure, the creep deformation is linear with the elastic deformation. They are in a band with fixed width. The creep deformation increased with total strain and with time. The slope of the creep curves increased gradually. The creep deformation was always much smaller than the total strain, especially at high strain. The smaller grain size

data (3.3 μm , 3.6 μm) were slightly above the other three data sets from around 4000 $\mu\epsilon$ total strain. This might correspond with behaviours in Figure 4.4.

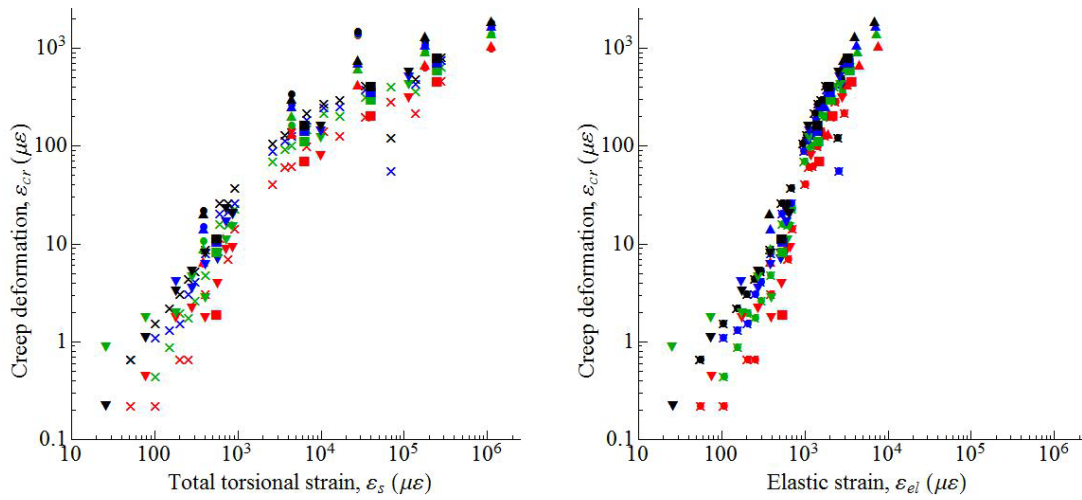


Figure 4.5 Creep deformation of the wires in Figure 4.4 are shown in the same log-log coordinate system. Red, green, blue and black symbols indicate creep under 2 minutes, 4 minutes, 8 minutes and 15 minutes load. The \times symbol is 50 μm diameter copper wire, 1m length, annealed at 850 $^{\circ}\text{C}$ for 60s, grain size 12 μm ; the \bullet symbol is 50 μm diameter copper wire, 1m length, annealed at 650 $^{\circ}\text{C}$ for 30s, grain size 3.3 μm ; the \blacktriangle symbols is 25 μm diameter copper wire, 0.5m length, annealed at 750 $^{\circ}\text{C}$ for 30s, grain size 3.6 μm ; the \blacktriangledown symbols is 25 μm diameter copper wire, 0.5m length, annealed at 800 $^{\circ}\text{C}$ for 90s, grain size 10 μm ; the \blacksquare symbols is 18 μm diameter copper wire, 0.25m length, annealed at 600 $^{\circ}\text{C}$ for 90s, grain size 6.5 μm .

The creep strain rates were plotted in Figure 4.6. It shows great similarity with the figure of creep deformation versus elastic strain in Figure 4.5. At each creep test, the creep strain rate decreases with time, as expected and seen here where the red symbols, corresponding to the shortest time under load, lie towards the upper left and the black symbols towards the lower right, corresponding to the longest times under load. For copper at room temperature the creep mechanism is likely to be that of dislocation unlocking in response to the stress and random thermal fluctuations over time. At higher stress (applied elastic strain in this case),

more dislocations will be unlocked giving higher total creep strain, the dependence, however, is expected to be near linear with applied stress.

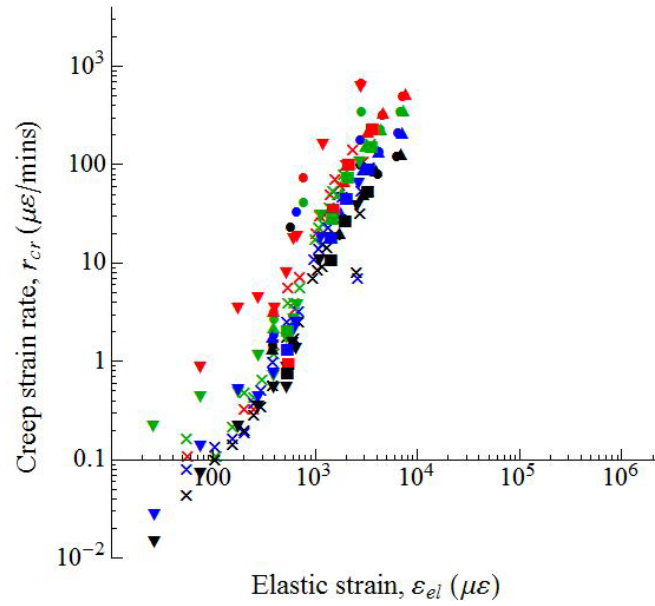


Figure 4.6 Creep strain rate versus elastic strain

4.3.4 Ramberg-Osgood fitting on high strain

The classic Ramberg-Osgood equation for the stress-strain relationship in work-hardening metals such as Cu may be rewritten in terms of elastic strain and plastic strain as,

$$\varepsilon_s = \varepsilon_{el} + \varepsilon_{pl} = \varepsilon_{el} + k\varepsilon_{el}^n \quad \text{Equation 4.3}$$

Walter *et al.* [12] gave a version appropriate to torsion, which however differs from Equation.4.3 for uniaxial testing only in the value of k . The Ramberg-Osgood equation fits our data over this very wide range to remarkable accuracy (solid blue curves in Figure 4.7) with exponents close to $n = 3$ (actually 3.04 ± 0.02 for the 50 μm wire and 3.14 ± 0.01 for the 25 μm wire, to compare with the value of Kraft of 2.0 in their gold wires). However, there are discrepancies at low strain, detectable because of the high quality of the data in this region. This is shown in more detail in Figure 4.7 (c) and (d), in which the x -axis is expanded by a factor of 100. Fitting just to the data in the region $0 < \varepsilon_s < 0.03$, we get the fits shown in

blue (dashed), for which n is increased to 4 (actually 3.98 ± 0.07) for the 50 μm wire and is unchanged at 3.14 for the 25 μm wire. These fits are also shown in Figure 4.7 (a) and (b). Finally, the quality of both of these fits at very low plastic strain is shown in Figure 4.7 (e) and (f). For both wires, the fits predict an earlier departure from the elastic line and much higher early plasticity than is observed in the data.

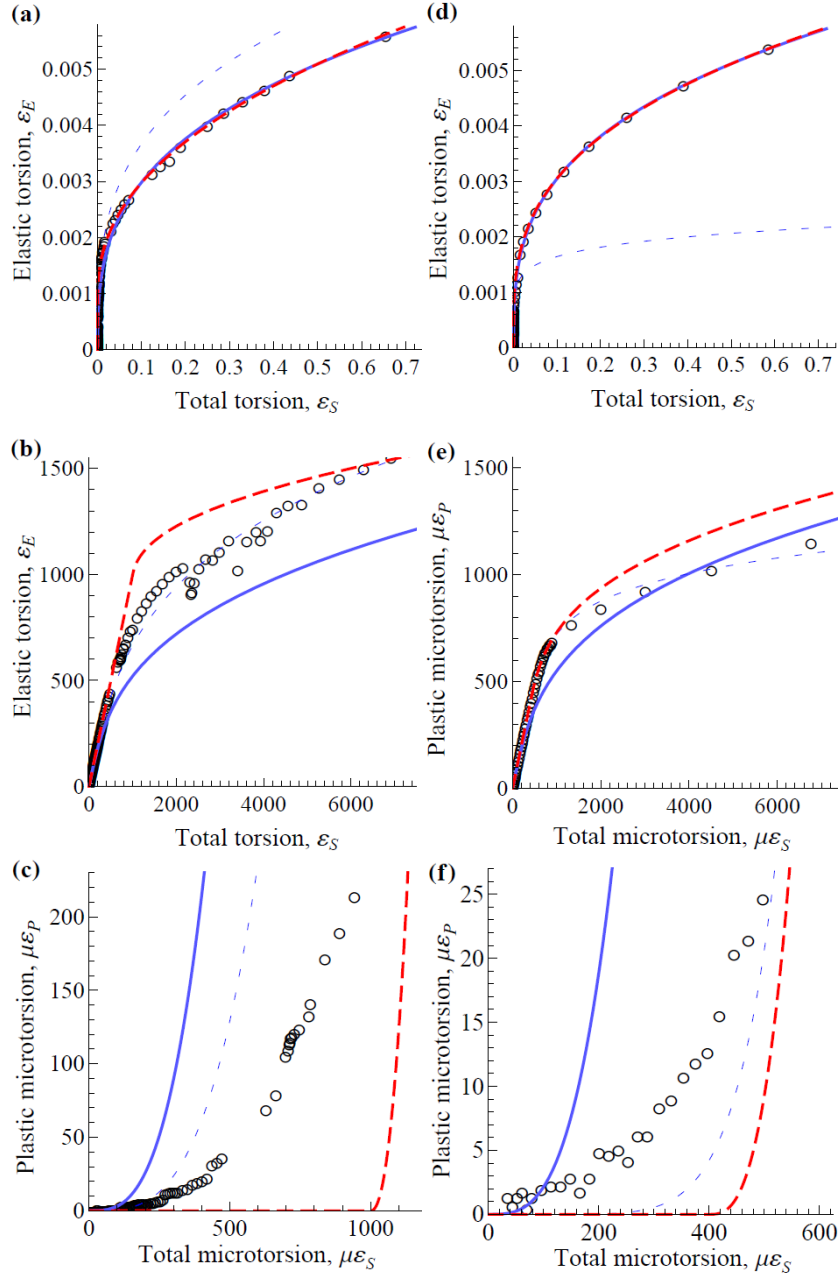


Figure 4.7 Ramberg-Osgood fitting for 50 μm diameter copper wire (a), (b), (c) and 25 μm diameter copper wire (d), (e), (f). The solid blue line is WK model, fitted over the whole range of the data; the red dashed line is σ_0 model, fitted over the range excluding the data below the yield strength; the dashed blue line is WK Low model, fitted only over the low strain data. All three models are plotted in three different scales: (a), (d) are in the range of strain from 0 to 0.7; (b), (e) are in the range of strain from 0 to 7000 $\mu\epsilon$; (c) is in the range of strain from 0 to 1200 $\mu\epsilon$ for 50 μm diameter copper wire and (f) is in the range of strain from 0 to 630 $\mu\epsilon$ for 25 μm diameter copper wire.

The Ramberg-Osgood fitting parameters on various conditions are shown in Table 1. From the table, there is not any clear relationship between the fitting parameters (α & n) and length scales (grain size & sample size) and it can be seen that for different regions of the loading, the fitting parameters are changed dramatically. For example, in one 50 μm diameter wire with grain size 12 μm , $n = 3.04$ and $\alpha = 4.72 \times 10^6$ in the R-O fitting from 0 to unit strain (actually 0.7 ϵ) while $n = 3.32$ and $\alpha = 1.17 \times 10^7$ in the R-O fitting from 0 to 1000 $\mu\epsilon$. And in another 50 μm wire with grain size 3.3 μm , $n = 4.43$ and $\alpha = 2.03 \times 10^9$ in R-O fitting from 0 to 0.7 ϵ while $n = 1.15$ and $\alpha = 2.68$ in the R-O fitting from 0 to 1000 $\mu\epsilon$. Where R-O fits are made to data in the literature for macroscopic tensile tests, the fitting parameters are rarely reported and even if they were, this analysis shows that the parameters are just mathematical fitting parameters with little physical significance.

| | | | | | | | | | |
|---|---|----------|--------------------------|-------------------------|--|---|----------|-------------------------|-------------------------|
| 50 μm diameter wire, 12 μm grain size | Whole strain range (WK model) | | Estimate | Standard error | 50 μm diameter wire, 3.3 μm grain size | Whole strain range (WK model) | | Estimate | Standard error |
| | | α | 4.72297x10 ⁶ | 541423 | | | α | 2.02723x10 ⁹ | 9.13296x10 ⁸ |
| | | n | 3.0439 | 0.0214211 | | | n | 4.42933 | 0.0919344 |
| | Whole strain range with yield (σ_0 model) | | Estimate | Standard error | | Whole strain range with yield (σ_0 model) | | Estimate | Standard error |
| | | α | 108372 | 10621.4 | | | α | 44185.1 | 7061.36 |
| | | n | 2.23652 | 0.0175109 | | | n | 1.97602 | 0.0287652 |
| | Low strain range (WK Low model) | | Estimate | Standard error | | Low strain range (WK Low model) | | Estimate | Standard error |
| | | α | 1.17069x10 ⁷ | 7.00611x10 ⁶ | | | α | 2.68321 | 17.3581 |
| | | n | 3.31941 | 0.0902173 | | | n | 1.15218 | 0.94969 |
| 25 μm diameter wire, 10 μm grain size | Whole strain range (WK model) | | Estimate | Standard error | 25 μm diameter wire, 3.6 μm grain size | Whole strain range (WK model) | | Estimate | Standard error |
| | | α | 7.71521x10 ⁶ | 246534 | | | α | 3.7403x10 ⁷ | 9.96657x10 ⁶ |
| | | n | 3.13986 | 0.00599608 | | | n | 3.66252 | 0.0550872 |
| | Whole strain range with yield (σ_0 model) | | Estimate | Standard error | | Whole strain range with yield (σ_0 model) | | Estimate | Standard error |
| | | α | 1.85838x10 ⁶ | 200558 | | | α | 32463.1 | 3516.38 |
| | | n | 2.82636 | 0.0199235 | | | n | 2.00287 | 0.0203326 |
| | Low strain range (WK Low model) | | Estimate | Standard error | | Low strain range (WK Low model) | | Estimate | Standard error |
| | | α | 8.83037x10 ¹⁵ | 0 | | | α | 6.40967x10 ⁷ | 1.42928x10 ⁸ |
| | | n | 6.08068 | 0.00349461 | | | n | 3.90036 | 0.339484 |

Table 1 Ramberg-Osgood fitting parameters on various sample sizes and grain sizes

According to Figure 4.8 (reported from Dunstan and Bushby's article [49]), various experiments results showed that the micromechanical behaviours are size dependent. The

solid line is the minimum strength due to the curvature of dislocation in a confined space l_{eff} . The absence of any experimental data below this minimum strength is strong confirmation of this interpretation. Same behaviours have been observed for copper in three geometries, tension (black crosses) flexure (black pluses) and torsion (black dots) and for well annealed metals the slopes for each set of data are close to 1, implying that the same mechanism is operating in all these geometries.

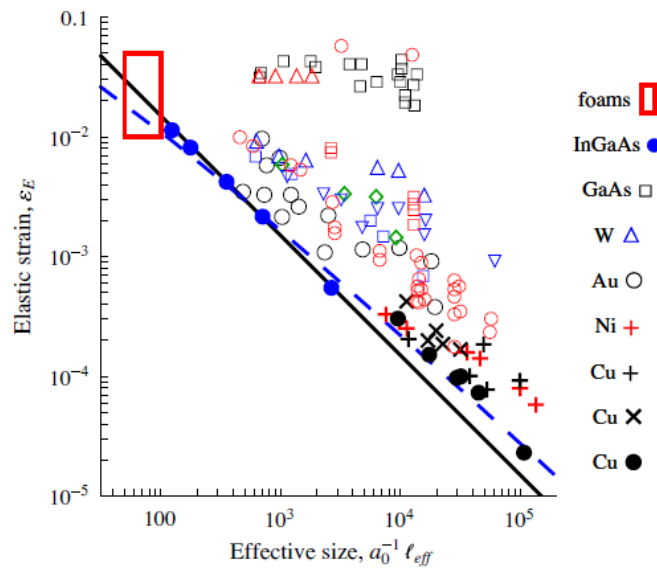


Figure 4.8 Elastic strain of various mechanical tests versus effective size, where open symbols for pillar compression, solid circles for InGaAs layers and for polycrystalline Cu wire in torsion, (+) for foils in flexure and (×) for wire in tension and (open rectangle) for tungsten nanofoams, where a_0 is the lattice parameter. (Reproduced from Dunstan and Bushby, 2013)

4.4 Summary

4.4.1 Deformation pattern in high strain

In Figure 4.2, both 5F and 6F showed a nearly identical curve in this plot. When the wire was shortened for loading to high strain, there was no discontinuity from data obtained at low strain over the whole 1m wire. This demonstrates that deformation at low strain occurred all

through the whole wire rather than being concentrated in some part.

4.4.2 Creep

In Figure 4.5, the creep deformation was increasing faster as a function of total strain from 10 $\mu\epsilon$ to 1000 $\mu\epsilon$ total strain than the creep deformation from 3000 $\mu\epsilon$ to unit strain.

There is a linear correlation between the creep deformation and elastic strain in Figure 4.5. And both creep strain and creep strain rate have similar correlation with the elastic strain and could be associated with expected dislocation creep mechanisms.

4.4.3 Theory fitting on high strain

The mechanism of plasticity and strain-hardening that gives the excellent fits to Equation.4.3 over the wide range of strain from about 2×10^{-3} to 0.7 cannot still be operative at the lowest strains, as less plastic deformation is observed than predicted. The simplest way to understand this is in terms of a yield strain ϵ_0 . We therefore rewrite Equation.4.3 as

$$\begin{aligned} \epsilon_s &= \epsilon_{el} + \epsilon_{pl} = \epsilon_{el} & \epsilon_s < \epsilon_0 \\ \epsilon_s &= \epsilon_{el} + k(\epsilon_{pl} - \epsilon_0)^n & \epsilon_s > \epsilon_0 \end{aligned} \quad \text{Equation 4.4}$$

Using Equation.4.4, good fits to the data $10^{-3} < \epsilon_s < 0.7$ are obtained, with $\epsilon_0 = 10^{-3}$ for both wires and with $n = 2.24 \pm 0.02$ for the 50 μm wire and $n = 2.83 \pm 0.02$ for the 25 μm wire, as shown in Figure 4.7 (a) and (b). In Figure 4.7 (e) and (f) we see that these fits predict less plastic deformation than is observed at very low strains. This is consistent with plausible mechanisms, if Equation.4.4 describes dislocation multiplication. Below the yield strength ϵ_0 at which multiplication would start (sources begin to operate), a small amount of plasticity may occur through the motion and elongation of existing dislocations. Further interpretation of these data awaits a more complete dataset.

The high strain results basically agree with current knowledge. Its main usage is extrapolating back to the low strain results.

4.4.4 Length scale

Ehrler [50] modified the slip distance theory [51] to combine both microstructural constraints and dimensional constraints together to account for the size effects in foil bending experiment.

He found that:

$$M_n \propto \frac{1}{h} + \frac{1}{d} = \frac{1}{l_{eff}} \quad \text{Equation 4.5}$$

where M_n is bending moment, d is the grain size, h is the film thickness and l_{eff} is the effective length. Bushby and Dunstan [52] extended this idea to thin wire torsion using h equal to the wire radius.

5. Discussion

5.0 Data comparison with literature

The data in the literature reviews are not sensitive enough in such low strain area. None of them are capable to explore such low strain area. Compared between our data and Walter & Kraft data, their results in low strain, e.g. $< 1000 \mu\epsilon$, are totally lost in noise, see Figure 5.1.

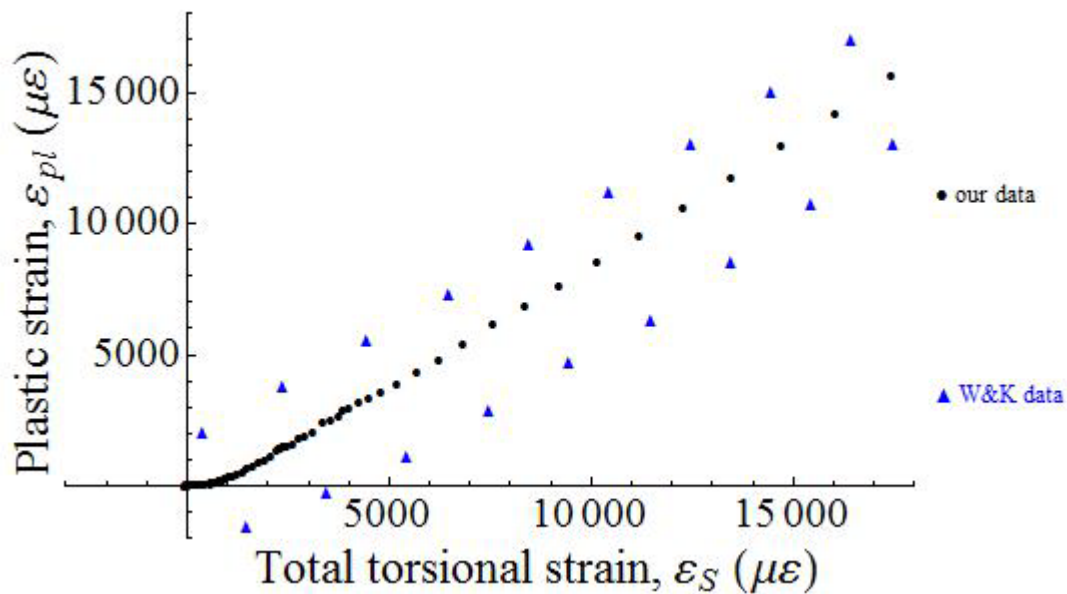


Figure 5.1 Comparisons between our data and Walter & Kraft data, black dots are our data and blue triangles are schematic representation of the data of Walter & Kraft and its scatter.

The high strain results were also compared with Fleck's high strain results, as seen in Figure 5.2. The curves are similar in shape but with different exponents. The micromechanical behaviours were not clear through these comparisons. The differences could be due to grain size, which was not considered by Fleck, or some unknown variables in specimen preparation. In Fleck's data, if their grain sizes are assumed similar to their wire diameters, a comparison with similar combined length scales was also made. The combined length scale of red dashed line is $0.2 \mu\text{m}^{-1}$ (20 μm diameter 20 μm grain size copper wire). The combined length scale of blue solid line is $0.15 \mu\text{m}^{-1}$ (15 μm diameter 15 μm grain size copper wire). The combined

length scale of our high strain data is $0.1233 \mu\text{m}^{-1}$ ($50 \mu\text{m}$ diameter $12 \mu\text{m}$ grain size copper wire). The similar combined length scales have similar behaviours. The differences in behaviours could be improved with more accurate data.

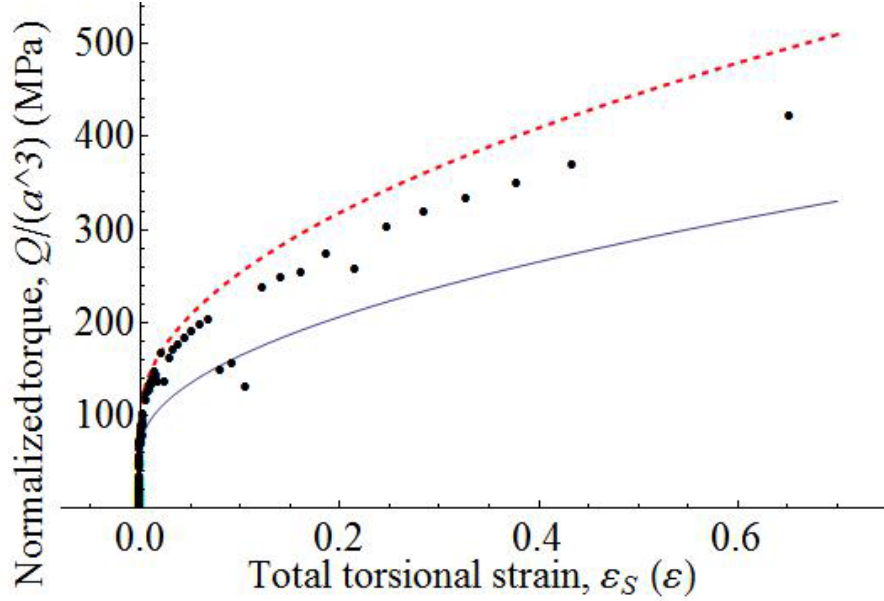


Figure 5.2 Comparisons between our data and Fleck's data. Black dots are our data ($50 \mu\text{m}$ diameter copper wire, grain size $12 \mu\text{m}$). Red dashed line and blue solid line are schematic representation of the data of Fleck's data ($30 \mu\text{m}$ diameter copper wire, grain size $30 \mu\text{m}$ and $15 \mu\text{m}$ diameter copper wire, grain size $15 \mu\text{m}$).

5.1 Yield points

From research results, there are indeed yield points at micron strain scales. However, various descriptions of the yield point can be made, e.g. from elastic limit, creep and recovery *etc.*

5.1.1 Elastic limit

In chapter 3.5.2, elastic behaviour is clearly observed at low strains. Below the elastic limit, dislocations might sometime move from one place to another place, causing some continuous or step-wise deformation. However, there is essentially no difference between the

deformation patterns in these cycles, within the sensitivity of the measurement, seen in Figure 3.21 (a) (b). Dislocation source operation need not be invoked in that regime.

Plasticity should occur after the elastic limit. Therefore the yield point could be defined as the end of any elastic behaviour in the first place, as seen in chapter 3.5.2.

At low strain regime, the yield points by elastic limit of monotonic loading are $160 \mu\epsilon$ in Figure 3.6 (25 μm diameter 3.6 μm grain size), $140 \mu\epsilon$ in Figure 3.7 (25 μm diameter 3.2 μm grain size) and $150 \mu\epsilon$ in Figure 3.8 (20 μm diameter 7.7 μm grain size). The yield points of cyclic loading are $170 \mu\epsilon$ in Figure 3.11 (50 μm diameter 12 μm grain size) and $-450 \mu\epsilon$ in Figure 3.13 (50 μm diameter 3.3 μm grain size). The yield points of cyclic loading with thermal recovery are $130 \mu\epsilon$ in Figure 3.20 (50 μm diameter 8 μm grain size) and $160 \mu\epsilon$ in Figure 3.21 (50 μm diameter 8 μm grain size).

Following the same principle (where the data is flat within the random error), but measured in another experiment that subsequently went to higher strain, the yield points by elastic limit could be also determined. In Figure 4.3, the yield points (total torsional strain up to $1000 \mu\epsilon$) are $270 \mu\epsilon$ for 25 μm diameter 3.3 μm grain size copper wire, $350 \mu\epsilon$ for 50 μm diameter 3.3 μm grain size copper wire, $205 \mu\epsilon$ for 50 μm diameter 12 μm grain size copper wire, $283 \mu\epsilon$ for 25 μm diameter 10 μm grain size copper wire and $380 \mu\epsilon$ for 18 μm diameter 6.5 μm grain size copper wire.

In Figure 4.4, the yield points (total torsional strain up to unit strain) are $5100 \mu\epsilon$ for 25 μm diameter 3.3 μm grain size copper wire, $5100 \mu\epsilon$ for 50 μm diameter 3.3 μm grain size copper wire, $2900 \mu\epsilon$ for 50 μm diameter 12 μm grain size copper wire, $2900 \mu\epsilon$ for 25 μm diameter 10 μm grain size copper wire and $2900 \mu\epsilon$ for 18 μm diameter 6.5 μm grain size copper wire.

5.1.2 Permanent creep deformation

Alternatively, we could define the yield point the onset of permanent creep deformation or

unrecoverable creep deformation. As seen in Figure 3.1, the creep deformation at about 180 $\mu\epsilon$ total strain is not recovered by annealing at 300 °C or as seen in 4B of Figure 3.13, the creep deformation around -235 $\mu\epsilon$ total strain is not fully recovered, which imply that a permanent change of the dislocations has taken place. These two results are the only two ‘permanent creep’ yield points that we have.

5.1.3 Appearance of Bauschinger effect

We could define the yield point as the forward strain at which the Bauschinger effect appears in the reverse strain, which is reduction in strength. As seen in 2B of Figure 3.18, the reverse plasticity starts from -75 $\mu\epsilon$ while forward plastic starts from 170 $\mu\epsilon$. The reverse plasticity occurred much earlier than forward loading. Also as seen in Figure 3.21 (a) (b), creep was fully recovered up to 80 $\mu\epsilon$ and -100 $\mu\epsilon$ total strain. Reversing the load direction after these small deformations does not show any differences in the behaviour. While in Figure 3.21 (c), creep was partly recovered at 200 $\mu\epsilon$ and -147 $\mu\epsilon$ total strain. The deformation of 6B increased faster than 5F. It appears that there is an imbalance state in the internal stress as soon as the elastic limit is exceeded. The changes of internal stress could be associated with the re-arrangement of existing dislocations or the loss or annihilation of dislocations (see abnormal thermal recovery at 26 $\mu\epsilon$ and 78 $\mu\epsilon$ total strain in Figure 3.20). These two results are the only two ‘Bauschinger effect’ yield points that we have.

5.1.4 Abnormal thermal recovery

The yield point could also be defined as the onset of abnormal creep deformation or abnormal recovery behaviour. As seen in Figure 3.20, the thermal annealing at 26 $\mu\epsilon$ total strain gave no recovery at all, the wire was deforming further; or the thermal annealing at 78 $\mu\epsilon$ total strain gave a strain recovery much more than any plastic deformation so far imposed.

Dislocations events are clearly observed during the creep tests. However, the yield is not

always significant compared with the sensitivity of the measurement. These two results are the only two ‘abnormal thermal recovery’ yield points that we have.

5.1.5 Theory fitting to high strain area

The Ramsberg-Osgood fitting in chapter 4.3.4 shows that the power law equation with a yield strength accounts for most of the plasticity over the whole range. According to the Equation 4.4, the yield point is 1000 $\mu\epsilon$ for 50 μm diameter 12 $\mu\epsilon$ grain size copper wire and is 400 $\mu\epsilon$ for 25 μm diameter 10 $\mu\epsilon$ grain size copper wire.

However, these fits predict less plastic deformation than is observed at very low strains. There is some additional microplasticity, amounting to some 25 $\mu\epsilon$ for the 25 μm diameter wire and ten times as much in the 50 μm diameter wire, which may be attributed to another mechanism. These could also be defined as yield points since the dislocation multiplication starts there.

And we could define the yield points as the beginning of dislocation source operation. This is the only ‘source operation’ yield point that we have.

5.1.6 Engineering yield point

In conventional engineering, the flow stress at 0.2% plastic strain is defined as the yield stress, and there is a corresponding elastic strain at yield (stress/modulus).E.g., for 50 μm diameter 12 μm grain size copper wire, the yield strain is about 1400 $\mu\epsilon$, which is far above from the descriptions mentioned above.

Yield points of all definitions mentioned above are put in the table below for a clear view.

| Definitions of yield points | | | | | | | | | | | |
|---|-------------------------------------|---|---|---|--|---|---|---|--|--|---|
| | | d = 25 μm , a = 3.6 μm | d = 25 μm , a = 3.2 μm | d = 20 μm , a = 7.7 μm | d = 50 μm , a = 12 μm | d = 50 μm , a = 3.3 μm | d = 50 μm , a = 8 μm | d = 50 μm , a = 8 μm | d = 25 μm , a = 10 μm | d = 50 μm , a = 20 μm | d = 18 μm , a = 6.5 μm |
| ‘Elastic limit’ yield point | Strain from 0 to 420 $\mu\epsilon$ | 160 $\mu\epsilon$ | 140 $\mu\epsilon$ | 150 $\mu\epsilon$ | 170 $\mu\epsilon$ | -450 $\mu\epsilon$ | 130 $\mu\epsilon$ | 160 $\mu\epsilon$ | | | |
| | Strain from 0 to 1000 $\mu\epsilon$ | | 270 $\mu\epsilon$ | | 205 $\mu\epsilon$ | 350 $\mu\epsilon$ | | | 283 $\mu\epsilon$ | | 380 $\mu\epsilon$ |
| | Strain from 0 to unit strain | | 5100 $\mu\epsilon$ | | 2900 $\mu\epsilon$ | 5100 $\mu\epsilon$ | | | 2900 $\mu\epsilon$ | | 2900 $\mu\epsilon$ |
| ‘Permanent creep deformation’ yield point | | | | | | -235 $\mu\epsilon$ | | | | 180 $\mu\epsilon$ | |
| ‘Bauschinger effect’ yield point | | | -75 $\mu\epsilon$ | | | | | 200 $\mu\epsilon$ & -147 $\mu\epsilon$ | | | |
| ‘Abnormal thermal recovery’ yield point | | | | | | | 26 $\mu\epsilon$ & 78 $\mu\epsilon$ | | | | |
| ‘R-O fitting’ yield point | | | | | 1000 $\mu\epsilon$ | | | | 400 $\mu\epsilon$ | | |
| Engineering yield point | | | | | 1400 $\mu\epsilon$ | | | | | | |

Table 2 Table of the definitions for all the yield points

5.2 Size effects

5.2.1 Grain size

The plastic deformation is indeed affected by the grain size, as seen in Figure 4.4. The elastic strain in high strain region of smaller grain sizes (3.2 μm and 3.3 μm) are clearly larger than the larger grain sizes (12 μm , 10 μm and 6.5 μm).

5.2.2 Sample size

The plastic deformation is also affected by the sample sizes (wire radius), as seen in Figure 4.3. The 18 μm diameter wire shows smaller plastic strain comparing to the 25 μm and 50

μm diameter wires.

5.2.3 Effective length scales

When the grain size and sample size were combined together, the yield strain of low strain in chapter 3 by elastic sensitivity limit versus the combined length scale is plotted in Figure 5.3. The data do not show much correlation between the length scale and the yield strain.

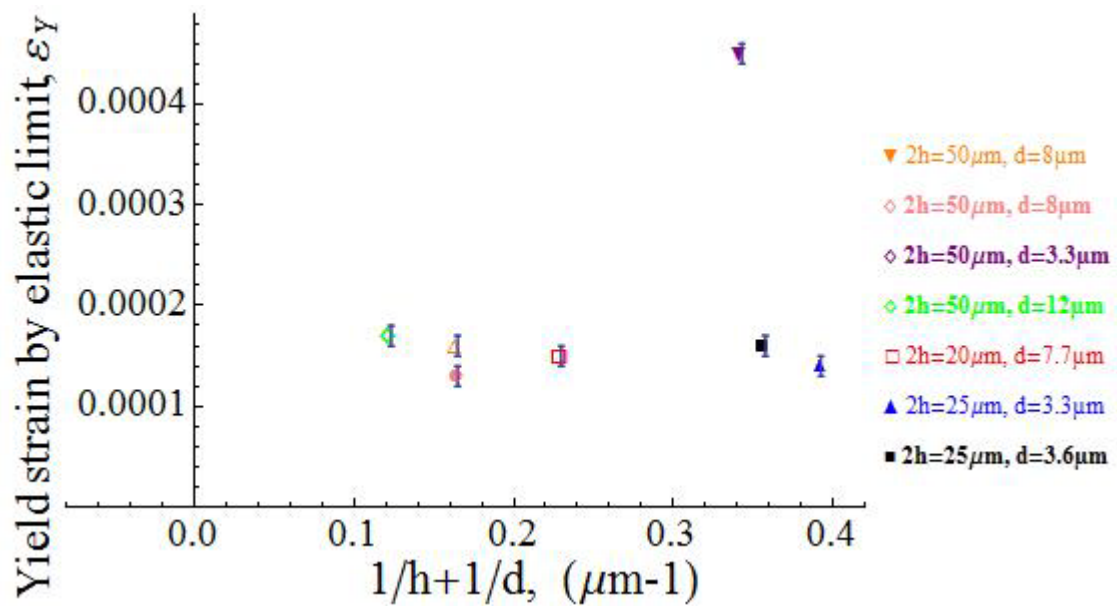


Figure 5.3 Yield strain (elastic limit) versus combined length scale at low strain

Up to 1000 $\mu\epsilon$, the yield strain by elastic limit versus the combined length scale is plotted in Figure 5.4.

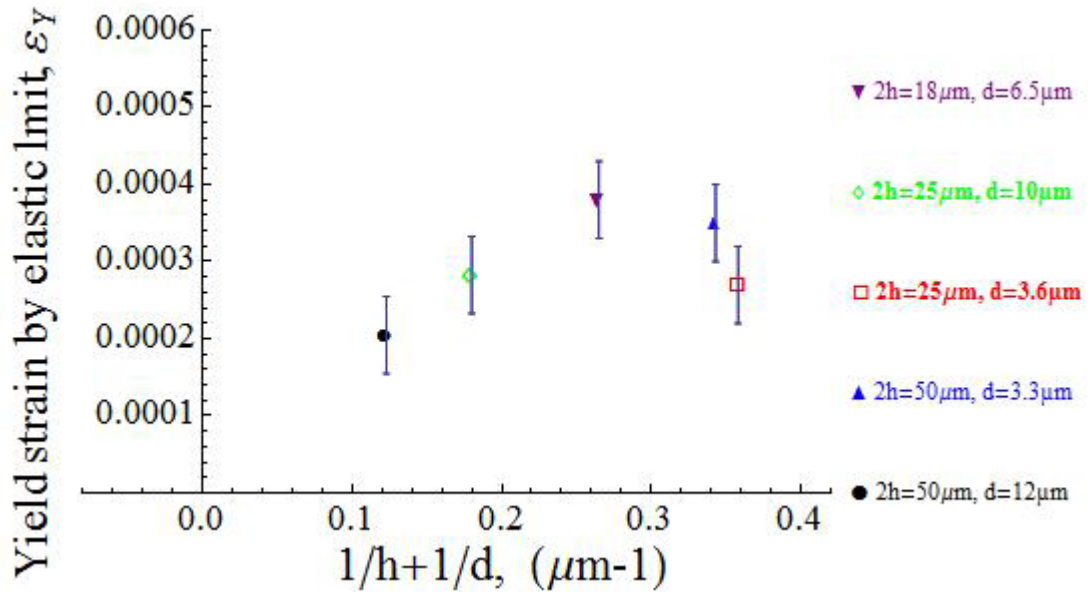


Figure 5.4 Yield strain by elastic limit versus combined length scale at strain up to $1000 \mu\epsilon$.

In high strain up to unit strain, the yield strain by elastic limit in Figure 4.4 versus the combined length scale is plotted in Figure 5.5.

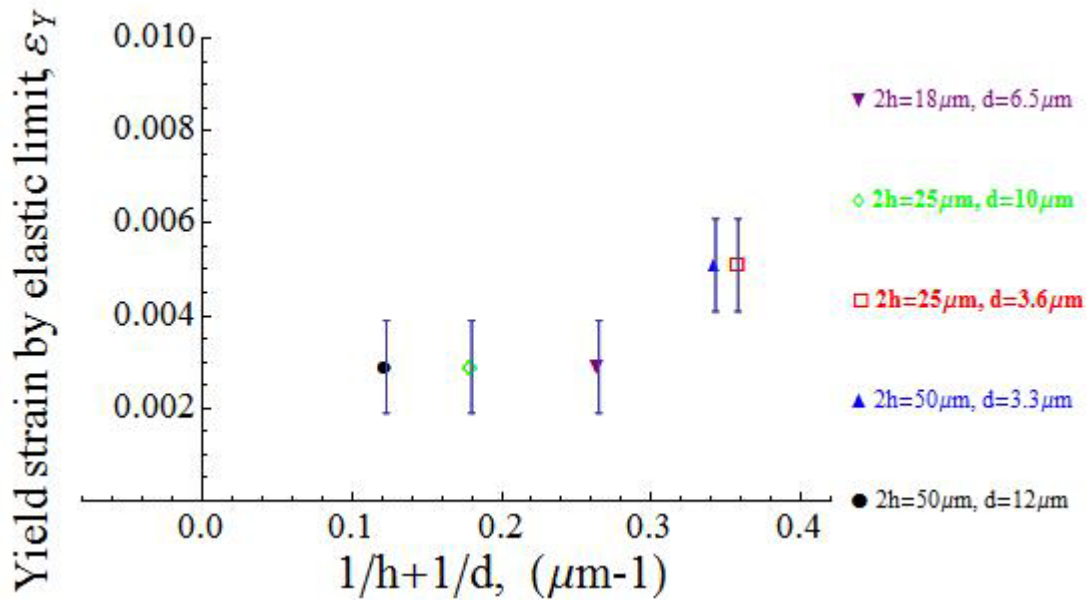


Figure 5.5 Yield strain by elastic limit versus combined length scale at high strain up to unit strain.

The yield strain by elastic limit was also plotted against inverse square root grain size, as seen in Figure 5.6. Here we got negative intercept within error, which is contradicted to the

physical facts: no negative strain exists.

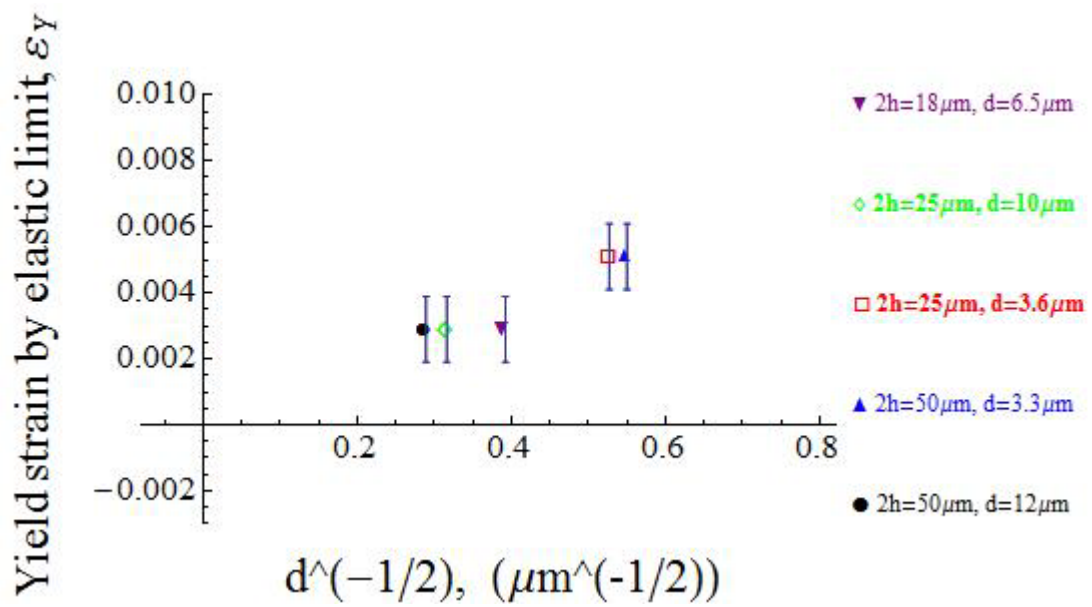


Figure 5.6 Yield strain by elastic limit versus inverse square root grain size at high strain up to unit strain.

The yield strain by elastic limit was plotted against inverse wire radius only, as seen in Figure 5.7. The data do not show much correlation between the wire radius and the yield strain.

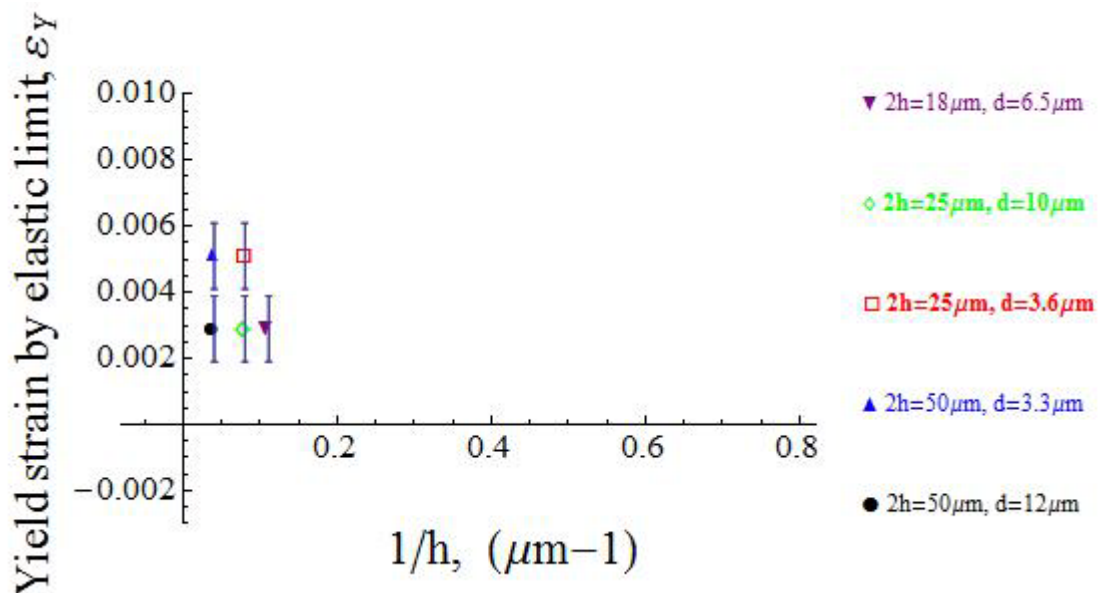


Figure 5.7 Yield strain by elastic limit versus inverse wire radius at high strain up to unit strain

The yield strain by elastic limit was plotted against inverse grain size only, as seen in Figure 5.8. The data show some correlation with the grain sizes.

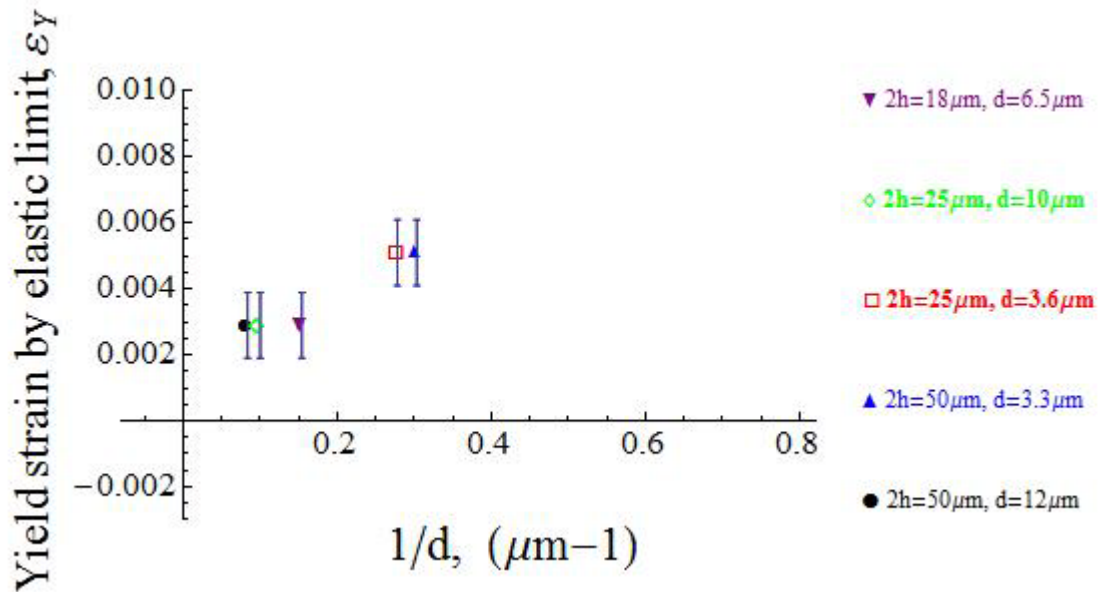


Figure 5.8 Yield strain by elastic limit versus inverse wire radius at high strain up to unit strain.

Therefore, the data would suggest that grain size is the more dominant size effect in the polycrystalline wires but the wire diameter is also important. Neither the grain size nor the wire diameter give as good a correlation with yield strain as the combination of both length scales. This is consistent with the findings of Ehrler *et al.* [17] for results on foil bending.

Combining the length scales with an inverse reciprocal sum gives a more physically meaningful result than combining the inverse square roots. The inverse square root plots tend to give a negative intercept to the plot, which is unphysical, implying that very large objects would have a negative stress – or fall apart.

The correlation with the combined length scale is better at higher plastic strains and becomes less convincing at low strains. This might imply that the combined length-scale is more applicable to situations where dislocation sources operate while in the micro-plastic

deformation area individual dislocations interact or re-arrange without significant source operation.

6. Conclusion

These studies of deformation in small scales by wire torsion are sensitive enough to detect the movement of a few dislocations in the micro-plasticity range. Comparing various sizes, size effects are clearly observed, depending on both grain size and wire size. The early fully reversible plasticity and creep are due to the reversible rearrangement of existing dislocations under the small stresses. Non-reversible plasticity may be attributed either to the departure of dislocations through the free surface, or the operation of dislocation sources.

From theory fitting and experimental evidence, yield points and flow are detectable in this low strain regime and could be defined as nine distinct concepts.

Bauschinger effects were not observed when the deformation remained below the ‘elastic limit’ yield point but were observed immediately the elastic limit was exceeded.

In future, dislocation dynamics simulations may well show the types of interactions that are likely to occur and hence allow calculation of the magnitude of the changes in internal stress distribution that lead to the reverse-loading Bauschinger effect and hence cyclic fatigue.

Publications

1. Bushby AJ, Feuvrier J, **Dong DV** and Dunstan DJ (2012). *Testing the limits of small scale plasticity with thin wires in torsion*. Materials Research Society Symposium Proceedings vol. 1424, 61-65.
2. **Dong D**, Dunstan DJ, Bushby AJ (2015). *Plasticity and thermal recovery of thin copper wires in torsion*. Philosophical Magazine vol. 95, (16-18) 1739-1750.

References

1. N.A. Fleck, G.M. Muller, M.F. Ashby, and J.W. Hutchinson, *Strain gradient plasticity: theory and experiment*. Acta Metallurgica et Materialia, 1994. 42, 475-487.
2. J.S. Stolken and A.G. Evans, *A microbend test method for measuring the plasticity length scale*. Acta Materialia, 1998. **46**, 5109-5115.
3. T.T. Zhu., A.J. Bushby and D.J. Dunstan, *Size effect in the initiation of plasticity for ceramics in nanoindentation*. Journal of the Mechanics and Physics of Solids, 2008. **56**, 1170-1185.
4. M.D. Uchic, D.M. Dimiduk, J.N. Florando and W.D. Nix, *Sample dimensions influence strength and crystal plasticity*. Science, 2004. **305**, 986-989.
5. E.O. Hall, *The deformation and ageing of mild steel: III discussion of results*. Proceedings of the Physical Society. Section B, 1951. **64**, 747-753.
6. N.J. Petch, *The cleavage strength of polycrystals*. The Journal of the Iron and Steel Institute, 1953. **174**. 25-28.
7. Y.Y. Lim and M.M. Chaudhri, *The effect of the indenter load on the nanohardness of ductile metals: An experimental study on polycrystalline work-hardened and annealed oxygen-free copper*. Philosophical Magazine A, 1999. **79**. 2979-3000.
8. H.D. Espinosa, B.C. Prorok and B. Peng, *Plasticity size effects in free-standing submicron polycrystalline FCC films subjected to pure tension*. Journal of the Mechanics and Physics of Solids, 2004. **52**. 667-689.
9. D.J. Dunstan, J.U. Gallé, B. Ehrler, N.J. Schimitt, T.T. Zhu, X.D. Hou, K.M.Y. P'ng, G. Gannaway and A.J. Bushby, *Micromechanical testing with microstrain resolution*. Review of Scientific Instruments, 2011. **82**, 093906.
10. W.-Y. Lu and B. Song, *Quasi-Static Torsion Characterization of Micro-diameter*

Copper Wires. Experimental Mechanics, 2011.**51**, 729-737.

11. B. Song and W.-Y. Lu, *An Improved Experimental Technique to Characterize MicroDiameter Copper Wires in Torsion*. Experimental Mechanics, 2015.**55**, 999-1004.

12. Walter, M. and O. Kraft, *A new method to measure torsion moments on smallscaled specimens*. Review of Scientific Instruments, 2011.**82**, 035109.

13. Y. Chen, O. Kraft and M. Walter, *Size effects in thin coarse-grained gold microwires under tensile and torsional loading*. Acta Materialia, 2015.**87**, 78-85.

14. D. Liu, Y. He, D.J. Dunstan, B. Zhang, Z. Gan, P. Hu and H. Ding, *Toward a further understanding of size effects in the torsion of thin metal wires: an experimental and theoretical assessment*. International Journal of Plasticity, 2013.**41**, 30-52.

15. D. Liu, Y. He, D.J. Dunstan, B. Zhang, Z. Gan, P. Hu, and H. Ding, *Anomalous plasticity in the cyclic torsion of micron scale metallic wires*. Physical Review Letters, 2013.**110**, 244301.

16. Z. Gan, Y. He, D. Liu, B. Zhang and L. Shen, *Hall–Petch effect and strain gradient effect in the torsion of thin gold wires*. Scripta Materialia, 2014. **87**, 41-44.

17. D.J. Dunstan, B. Ehrler, R. Bossis, S. Joly, K.M.Y. P'ng and A.J. Bushby, *Elastic limit and strain hardening of thin wires in torsion*. Physical Review Letters, 2009.**103**, 155501.

18. M.F. Ashby, *The deformation of plastically non-homogeneous materials*. Philosophical Magazine, 1970.**21**, 399-424.

19. J.F. Nye, *Some geometrical relations in dislocated crystals*. Acta Metallurgica, 1953.**1**, 153-162.

20. W. D. Nix and H. Gao, *Indentation size effects in crystalline materials: a law for strain gradient plasticity*. Journal of the Mechanics and Physics of Solids, 1998.**46**, 411-425.

21. G.I. Taylor, *The mechanism of plastic deformation of crystals. Part I.*

Theoretical. Proceedings of the Royal Society of London. Series A, Containing Papers of a Mathematical and Physical Character, 1934.**145**, 362-387.

22. R.H. Dixon and P.J. Goodhew, *On the origin of misfit dislocations in InGaAs/GaAs strained layers*. Journal of Applied Physics, 1990.**68**, 3163-3168.

23. F.C. Frank and J.H. van der Merwe, *One-Dimensional Dislocations. I. Static Theory*. Proceedings of the Royal Society of London. Series A, Mathematical and Physical Sciences, 1949.**198**, 205-216.

24. D.J. Dunstan, *Mathematical model for strain relaxation in multilayer metamorphic epitaxial structures*. Philosophical Magazine A, 1996.**73**, 1323-1332.

25. J.W. Matthews and A.E. Blakeslee, *Defects in epitaxial multilayers: I. Misfit dislocations*. Journal of Crystal Growth, 1974.**27**, 118-125.

26. D.J. Dunstan, *Strain and strain relaxation in semiconductors*. Journal of Materials Science: Materials in Electronics, 1997. **8**, 337-375.

27. D.J. Dunstan and A.J. Bushby, *Theory of deformation in small volumes of material*. Proceedings of the Royal Society of London A: Mathematical, Physical and Engineering Sciences, 2004. **460**, 2781-2796.

28. R. Beanland, *Multiplication of misfit dislocations in epitaxial layers*. Journal of Applied Physics, 1992.**72**, 4031-4035.

29. I.J. Spary, A.J. Bushby and N.M. Jennett, *On the indentation size effect in spherical indentation*. Philosophical Magazine, 2006.**86**, 33-35.

30. J.R. Greer, W.C. Oliver and W.D. Nix, *Size dependence of mechanical properties of gold at the micron scale in the absence of strain gradients*. Acta Materialia, 2005.**53**, 1821-1830.

31. B. von Blanckenhagen, P. Gumbsch and E. Arzt, *Dislocation sources and the flow stress of polycrystalline thin metal films*. Philosophical Magazine Letters, 2003.**83**, 1-8.

32. T.A. Parthasarathy, S.I. Rao, D.M. Dimiduk, M.D. Uchic and D.R. Trinkle, *Contribution to size effect of yield strength from the stochastics of dislocation source lengths in finite samples*. ScriptaMaterialia, 2007. **56**, 313-316.
33. D.J. Dunstan, *Critical thickness theory applied to micromechanical testing*. Advanced Engineering Materials, 2012.**14**, 942-947.
34. D. Kiener, C. Motz, T. Schöberl, M. Jenko and G. Dehm, *Determination of mechanical properties of copper at the micron scale*. Advanced Engineering Materials, 2006.**8**, 1119-1125. .
35. J.D. Eshelby, F.C. Frank and F.R.N. Nabarro, *XLI. The equilibrium of linear arrays of dislocations*. The London, Edinburgh, and Dublin Philosophical Magazine and Journal of Science: Series 7, 1951. **42**, 351-364.
36. C. Motz and D.J. Dunstan, *Observation of the critical thickness phenomenon in dislocation dynamics simulation of microbeam bending*. ActaMaterialia, 2012.**60**, 1603-1609.
37. E. Demir and D. Raabe, *Mechanical and microstructural single-crystal Bauschinger effects: Observation of reversible plasticity in copper during bending*. ActaMaterialia, 2010.**58**, 6055-6063.
38. C. Kirchlechner, W. Grosinger, M.W. Kapp, P.J. Imirich, J.-S. Micha, O. Ulrich, J. Keckes, G. Dehm and C. Motz, *Investigation of reversible plasticity in a micron-sized, single crystalline copper bending beam by X-ray μ Laue diffraction*. Philosophical Magazine, 2012.**92**, 3231-3242.
39. D. Kiener, C. Motz, W. Grosinger, D. Weygand and R. Pippan, *Cyclic response of copper single crystal micro-beams*. ScriptaMaterialia, 2010. **63**, 500-503.
40. E. Heyn, *Short reports from the metallurgical laboratory of the Royal Mechanical and Testing Institute of Charlottenburg*. Metallographist, 1903.**5**, 37-64.

41. C.T.F. Ross, *Mechanics of solids*. Horwood Publishing Limited, 1999.
42. S. Suresh, *Fatigue of materials*, 2nd edition. Cambridge University Press, 1998.
43. S.P. Baker, R.-M. Keller-Flaig and J.B. Shu, *Bauschinger effect and anomalous thermomechanical deformation induced by oxygen in passivated thin Cu films on substrates*. Acta Materialia, 2003.**51**, 3019-3036.
44. Y. Xiang and J.J. Vlassak, *Bauschinger effect in thin metal films*. Scripta Materialia, 2005. **53**, 177-182.
45. Y. Xiang and J.J. Vlassak, *Bauschinger and size effects in thin-film plasticity*. Acta Materialia, 2006.**54**, 5449-5460.
46. A. Abel and H. Muir, *The Bauschinger effect and discontinuous yielding*. Philosophical Magazine, 1972.**26**, 489-504.
47. D.J. Dunstan and A.J. Bushby, *Grain size dependence of the strength of metals: the Hall–Petch effect does not scale as the inverse square root of grain size*. International Journal of Plasticity, 2014.**53**, 56-65.
48. M.A. Meyers and K.K. Chawla, *Mechanical behavior of materials*, 2nd edition. Cambridge University Press, 2008.
49. R.E. Smallman and R.J. Bishop, *Modern physical metallurgy and materials engineering*, 6th edition. Butterworth-Heinemann, 1999.
50. D.J. Dunstan and A.J. Bushby, *The scaling exponent in the size effect of small scale plastic deformation*. International Journal of Plasticity, 2013.**40**, 152-162.
51. B. Ehrler, X.D. Hou, T.T. Zhu, K.M.Y. P'ng, C.J. Walker, A.J. Bushby and D.J. Dunstan, *Grain size and sample size interact to determine strength in a soft metal*. Philosophical Magazine, 2008.**88**, 3043-3050.
52. H. Conrad, S. Feuerstein and L. Rice, *Effects of grain size on the dislocation density and flow stress of niobium*. Materials Science and Engineering, 1967.**2**, 157-168.

53. A.J. Bushby and D.J. Dunstan, *Size effects in yield and plasticity under uniaxial and non-uniform loading: experiment and theory*. Philosophical Magazine, 2011.**91**, 1037-1049.